Modeling of Argon-Molten Steel Flow in a Slab Continuous Caster by Discrete Phase Model

Yousif R. Al-Dhafeery

Mining and Materials Engineering

McGill University, Montreal

April 2012

A thesis submitted to McGill University in partial fulfillment of the requirements of the degree of Masters of Engineering.

Abstract

Improvement of steel products cleanliness and alleviating problems related to Submerged Entry Nozzle (SEN) clogging are two main requirements for the efficient operation of a steel continuous caster. Argon injection is employed to achieve these objectives. Unfortunately, argon may cause quality defects related to slag entrainment and/or pencil pipe defect as well as influence molten steel flows and temperature distributions in the SEN and in the mold region.

The well-known k-ω turbulence model, together with the 3D continuity, momentum and energy equations, was employed in order to predict and quantify the single-phase velocity fields and temperature distributions for the upper mold region of a slab continuous caster. In addition, the Discrete Phase Model (DPM), which incorporates bi-directional momentum coupling and force balance over discrete bubbles, was used to simulate the two-phase liquid steel-argon flows. Transient 3D numerical simulations were carried out using the ANSYS-FLUENT code (version 12) for various injection rates of discrete argon bubbles from a porous stopper-rod into a quarter-model of SEN and mold configuration.

Influence of argon injection parameters, like injection rate and bubble size, for different casting speeds of a conventional slab caster were studied thoroughly. A comparison between predicted surface velocity results and experimental results from the literature show an acceptable agreement. Simulations indicate that high argon injection rates are detrimental to flow patterns, this is especially true for low casting speeds. Since under these conditions there is a high probability of slag emulsification and bubble entrapment. Argon injection, especially with small bubble sizes, usually forms two velocity peaks at the meniscus level.

These peaks have less-dominant effects for lower injection rates and/or larger bubble sizes. Whereas, higher casting speeds reduce the impact of gas injection near SEN walls due to the lower gas volume fraction in that region but enhances the superheat dissipation rate at the mold's upper region.

The present modeling results show that the DPM simulations can provide reasonable qualitative guidelines in characterizing the complex molten steel-argon gas flow in the mold. The present numerical parametric study suggests that a proper control of argon injection rate, corresponding to a specific casting speed, is essential in obtaining optimum flow patterns, in reducing the slag entrainment and cold spots, and in enhancing superheat dissipation rates.

Résumé

L’amélioration de la propreté de l'acier fondu et la réduction des problèmes liés au colmatage de la busette immergée (SEN) sont deux principaux critères pour un fonctionnement efficace d’une coulée continue d’acier. L'injection d'argon est utilisée pour atteindre ces objectifs. Cependant, l'argon peut causer des défauts de qualité liés à l'entraînement de laitier et / ou aux défauts de type "pencil pipe" et affecter les flux d'acier en fusion et les distributions de température dans le SEN et dans la région du moule.

Le modèle bien connu de turbulence k-ω, ainsi que la continuité, la dynamique et les équations 3D de l'énergie, ont été employés afin de prédire et de quantifier les champs de vitesse monophasés et les distributions de température pour la région supérieure d'une brame de coulée continue. En outre, le Modèle de la Phase Discrète (DPM), qui comporte un couplage de moments bidirectionnel et l'équilibre des forces sur des bulles discrètes, a été utilisé pour simuler les flux du liquide à deux phases acier-argon. Les simulations 3D en régime transitoire ont été réalisées par ANSYS FLUENT-code (version 12) pour différents taux d'injection de bulles discrètes d'argon à partir d'un bouchon-tige poreux dans un modèle quart de SEN et de configuration du moule.

L'influence des paramètres d'injection d'argon, comme le taux d'injection et la taille des bulles, pour des vitesses de coulée différentes d'un caster classique a été étudié à fond. Une comparaison entre les résultats prévus de vitesse de surface et les résultats expérimentaux de la littérature montre un accord acceptable. Des simulations indiquent que le niveau élevé des taux d'injection d'argon est préjudiciable au modèle des flux, ce qui est particulièrement vrai pour les faibles vitesses de coulée. Puisque, dans ces conditions, il y a une forte probabilité de scories d'émulsification et de piégeage de bulles. L'injection d'argon, en particulier avec des bulles de petite taille, forme habituellement deux pics de vitesse au niveau du ménisque. Ces pics ont des effets moins dominants sur les taux d'injection inférieurs et / ou les bulles de plus grande taille. Des vitesses de coulée élevées réduisent l'impact de l'injection de gaz près des murs SEN en raison de la fraction volumique de gaz inférieure dans cette région, mais améliorent le taux de dissipation de surchauffe dans la région supérieure du moule.

Les résultats de cette modélisation montrent que les simulations DPM peuvent fournir des lignes directrices qualitatives raisonnables dans la caractérisation du flux gazeux fondu complexe acier-argon dans le moule. La présente étude numérique paramétrique suggère qu'un contrôle adéquat du taux d'injection d'argon, ce qui correspond à une vitesse de coulée spécifique, est essentiel dans l'obtention de modèles d'écoulement optimaux, pour réduire l'entraînement des scories et des points froids, et pour améliorer les taux de dissipation de la surchauffe.

Acknowledgements

My deep gratitude and gratefulness to God (Creator of mankind and his/her knowledge) for his countless blessings and support.

My sincere gratitude to Professor Mainul Hasan for his continuous effort in providing guidance during my studies.

I would like to convey my gratitude to Dr. Kinnor Chattopadhyay, Waqqas Khan and Ken Morales for the technical tutorials of ANSYS-FLUENT code.

Special thanks to my colleagues and friends, including Manas Paliwal, Faisal Al-Ghamdi and Mohammad Al-Abbad, for their support and advice.

My sincere appreciation to my management at Saudi Arabia Basic Industries Corp. (SABIC) for the granted scholarship.

Finally, my sincere gratitude to my parents, grandmothers and family for their patience and supplications.

Table of Contents

List of Symbols

ρ : density of the fluid , kg/m^3

t : time, s

$u\ v\ w$: velocity components, m/s

$x\ y\ z$: 3D (Cartesian) space coordinates, m

μ: isotropic dynamic viscosity of a Newtonian fluid, Pa.s

$\hat{p}$ or P : pressure, pascal

E: total energy, Joule

$S_{Mx}\ S_{My}\ S_{Mz}$: source terms for momentum equations.

$\tau_{xx}\ \tau_{yy}\ \tau_{zz}$: viscous normal stresses on particle cell, N / m^2

$\tau_{yx}\ \tau_{zx}\ \tau_{xy}\ \tau_{zy}\ \tau_{xz}\ \tau_{yz}$: Viscous shear stresses on particle cell, N/m^2

k : thermal conductivity of fluid continuum, W/K.m^2

T: absolute temperature, K

grad T: gradient of temperature, K/m

S_E: source terms, e.g. potential energy, heat production due to chemical reactions, etc.

u : velocity vector in momentum equation.

q : vector heat flow per unit area, W/m^2

ρ_P : particle density, kg/m^3

C_D : drag coefficient as a function of particle Reynolds number.

u_p: particle velocity, m s^{-1}

m_p: mass of the particle, kg

V_p: volume of the particle, m^3

g: acceleration due to gravity, m s^{-2}

d_p : diameter of the particle, m

μ, viscosity of the fluid, kg m^{-1} s^{-1}

F_D: drag Force, N

F_B: buoyancy Force, N

F_a: added mass force for accelerated flows, N

f_a: added mass force per particle mass, m.s^{-2} or N/kg

Re: dimensionless Reynolds Number.

ζ: a normally distributed random number based on GPD.

k: turbulent kinetic energy, m^2/s^2

ω : specific dissipation rate, s^{-1}

$\boldsymbol{\tau}$: the discrete phase relaxation time, s^{-1}

$\boldsymbol{L_e}$: the eddy length scale, m.

N: the number of bubbles in a computational cell

$\dot{m}_p$: mass flow rate of gas bubbles, kg/s

$\vec{F}$: inter-phase exchange momentum, N

μ_o: particle viscosity, Pa.s

$d_{bubble,max}$: bubble maximum diameter, m

ε: stirring power for , W/tonne

σ: surface tension, $N.m^{-1}$

We_{cr} : Critical weber number.

$d_{bubble,max}$: maximum bubble diameter in a turbulent flow, m

V_c : casting speed, $m.min^{-1}$

Q_g : argon injection rate, $Liter.min^{-1}$

D_b : argon bubble diameter, mm

Chapter 1: Continuous Casting Process and Modeling

1.1 Introduction

Steel, including carbon steel and alloy steel, is the most reliable building material for construction, automobile, household appliances, industrial vessels and many other applications. Even though many alternative materials, such as composites and plastics, are increasingly used, steel still is irreplaceable due to its availability and price advantage over both non-metallic and metallic materials that are equivalent in strength. Also, steel recycling is certainly an added benefit from environmental perspectives.

One of the important stages in steel production is casting which have evolved over the past decades. Steel casting started initially with ingot casting process but due to the high demand on steel productivity and desire to lower costs, plants adapted Continuous Casting (**CC**) process to achieve these goals. Steel continuous casting process emerged in 1950's with steady improvements over later years. There are different types of conventional casters based on the produced shapes of the semi-finished products which are billet, bloom and slab casters. Moreover, over the last two decades new casting technologies, such as thin slab casting and strip casting, were invented and commercialized to reduce the subsequent stages of thermo-mechanical processes required in conventional castings [1-3].

Quality improvement of the continuously casted semi-finished steel is highly desired for final products. There are many methods to improve quality, one such method is the utilization of Submerged Entry Nozzle (**SEN**), a refractory tube used between tundish and mold in **CC** process, to prevent reoxidatin of molten steel and splashing when the molten stream strikes the liquid surface in the mold [4-5].

Unfortunately, clogging of SEN is one of the main bottlenecks faced by steel continuous casters and it is counter-measured by a well-proven method known as argon injection. Understanding and possible optimization of argon injection involve system modeling through Computational Fluid Dynamics (**CFD**) which is the main focus of this thesis.

1.2 Continuous Casting Historical Developments

1.2.1 Continuous Casting versus Ingot Casting

The traditional method of steel production through casting was initially ingot casting, which was and still is used for casting cast iron and non-ferrous metals. In brief, ingot casting process involves shifting the steel in molten state by a teeming ladle from a furnace to ingot mold station where the liquid steel is poured into a stationary water-cooled mold which can have square, round or polygonal cross section depending on the final product [1]. The casting mold is usually made of cast iron which forms a thick-walled container open at the top and placed on a thick-bottom plate, also called stool. Because the thermal coefficient of cast iron is lower than steel, steel during solidification contracts more than cast iron which makes ingot detachment easier from the mold. The inner wall has a coated layer, usually made of tar or fine carbon that decomposes during solidification to prevent sticking of solidified ingots with mold. After steel solidification inside the mold, the solidified ingot is taken to soaking pits for reheating and later for further processing in mills to produce semi-finished products such as slabs, blooms or billets which then are rolled to final products [2].

At the beginning of the 19th century, the pioneering trials for **C**ontinuous **C**asting (**C.C.**), also called **strand casting** [2], started mainly for non-ferrous materials with low melting points such as lead. However, steel casting through this route had several difficulties because of the high temperature, low thermal conductivity of steel and relatively slow solidification rate. The first patent involving continuous casting basic principles was given to R M Daelen in 1889 [3]. Initially, problems such as sticking of solidified shell to the mold walls were preventing efficient continuous casting process for ferrous materials. Later in 1920s, Junghans, a German researcher, patented a non-harmonic mould oscillation, e.g. few centimeters with a frequency in the order of 1 Hz, to avoid sticking which was a major breakthrough for efficient continuous casting of metals starting with brass then later with steel pilot plants in mid 1940s [3]. By overcoming such problems, steel continuous casting began to emerge as a commercially viable process to replace steel ingot casting in the 1960s [4].

Since about five decades, steel casting has shifted from conventional ingot casting to continuous casting. Continuous casting route have increased steel yield from 85% in the 1970s to more than 95% today. Generally, steel produced by **C.C.** route have less defects compared to ingot casting. Therefore, the conventional practice of cropping defective parts of ingots is not necessary anymore with continuous casting, thus, increasing the output tonnage and yield. Furthermore, the conventional casting equipment for soaking, slabbing or blooming steps which are necessary in ingot casting are not required any more in continuous casting. In general, steel **C.C.** route provides a better quality, produces a more homogenous product and higher production rate/yield with less operating costs in comparison to conventional ingot casting [6]. Furthermore, several technological advancements were implemented over the few last decades to improve the cast quality and productivity further. These improvements include the following [1]:

a) Implementation of the bent vertical strand design to replace the straight vertical strand in 1970s.
a) Usage of electromagnetic stirrer for quality improvement and product homogeneity.
b) Introduction of rapid tundish and ladle changing equipment to increase yield and productivity.
c) Utilization of variable mold width adjustments and air-mist cooling.
d) Shrouding of molten metal streams by refractory tubes and inert gas injection to avoid contact with air and prevent reoxidation.
e) Integrated computer control of the casting process.

The overall profile of the strand, which is one of the major characteristic features of continuous casters, has evolved over the years. Initial continuous casters were totally vertical in the design, and thus required considerable height to achieve reasonable production tonnage per strand. The vertical-type casters faced several problems such as the severe stress against support rolls located under the mold due to ferrostatic pressure and the requirement to shift the produced steel from vertical to horizontal after the semi-finished product was severed. To overcome problems of vertical casters, the design of strand shifted from vertical to curved type "bow-type", or Curved with Progressive Straightening (CPS) in the 1960s[1]. Such design involves bending and straightening a strand to render it horizontal prior to cutting. With such strands, production rates increased and capital and maintenance costs got reduced [2]. The successive developments of **CC** strand profiles or shapes over several decades are shown in Figure 1.1.

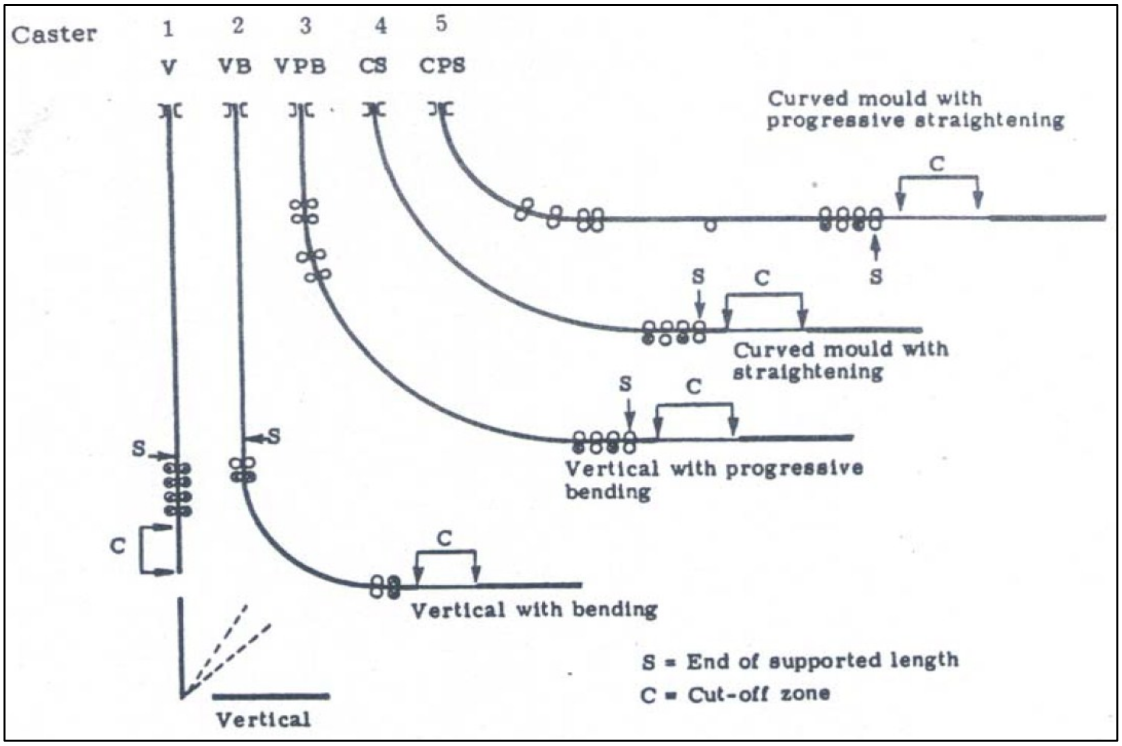

Figure 2.1: Main types of strand shapes utilized in continuous casters [3].

Another variation of continuous casters is the horizontal caster design which incorporates a stationary mold, usually made of graphite[1], connected directly to tundish or holding furnace without flow-control devices. Such design helps in avoiding bending-straightening of strand and its associated problems. Other benefits of horizontal casting include reduced ferrostatic pressure on support roll and reduced exposure to air to avoid reoxidation. Unfortunately, such design faced several difficulties related to steel feeding which limits high productivity and product sizes. Horizontal continuous casters are commonly used for casting bars or rods of cast iron, special alloys and non-ferrous alloys such as copper alloys [3].

There are several types of cast sections or semi-finished products, which vary in sizes and dimensions, produced through conventional "bow-type" casters. For example, square billet with maximum size of 150x150 mm^2 and rectangular bloom with maximum size of 350x600 mm^2. Billets and blooms are used as feed material of rolling mills to produce bars and rails respectively. Also, similar casters can cast round billets, which are used mainly to manufacture seamless pipes, reaching a diameter of about 500 mm. Moreover, the rectangular thick-slab is

[1] Graphite (one of carbon allotropes) is used because of its superior thermal shock resistance, self-lubrication, high thermal conductivity and low wettability by liquid metals.

another semi-finished product with higher aspect ratios, ranging from 3:1 to 12:1, compared to blooms. Nowadays, some slab castings' thickness range between 150 to 300 mm and the maximum width can reach about 3 meters. Slabs are processed through rolling to produce final products such as plates and sheets. In addition, final products such as I-beams or H beams are produced by continuously casting beam-blank semi-finished product, also called "dog-bone" shapes [3].

1.2.2 New Continuous Casting Technologies

Today, new casting processes have been developed to reduce capital and operational costs like thin slab casters and strip casters. Thin slab casters with "mini-mills" are considered the new trend in continuous casters and this process is one major rival to the conventional process due to the reduced energy costs and the lower requirement of manpower. Also, the "mini-mill", i.e. direct hot charging to the finishing rolling mill where the roughing mill is omitted, is another advantage of thin slab casters over conventional casters as illustrated by Figure 1.2. Furthermore, thin slab casters utilize tunnel-type furnace for temperature equalizing or homogenization before the thin slab enters the Hot Strip Mill (HSM). The near-net shape thin slabs of thicknesses between 50-100 mm indicate a reduction in thermo-mechanical processing time and costs for producing flat coils which are in high-demand in the automobile industry [3].

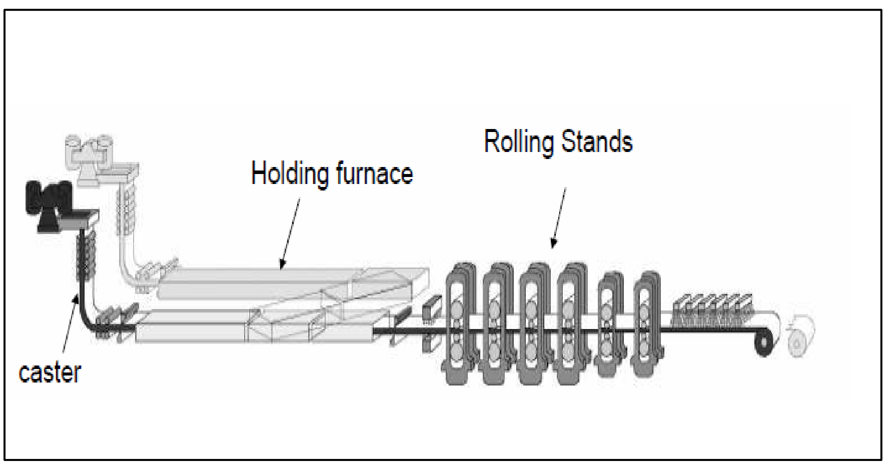

Figure 2.2: Layout of thin slab caster and integrated mini-mills.

To further reduce the operational costs and processing time, innovative strip casters, which do not require rolling mills, are introduced in steel industry. One type of strip casters is the

Hazelett "twin-belt" caster where the molten alloy is poured between two endless, parallel and water-cooled steel belts. The belts are held in tension and positioned at a small angle as shown in Figure 1.3. The pouring nozzle is accurately located between belts where a coating is applied on belt surfaces to avoid sticking. Hazelett casters are usually used for casting non-ferrous alloys such as aluminum and copper alloys. The strip thickness in these casters ranges between 9 mm to 35 mm depending on the product requirement [3].

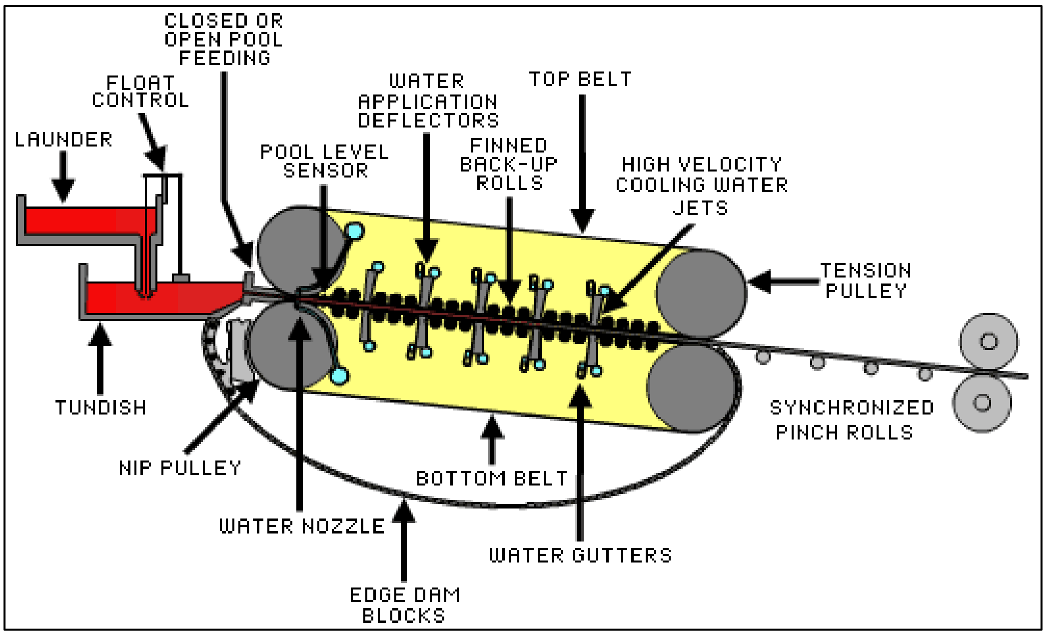

Figure 2.3: General layout of Hazelett twin-belt strip caster.

Twin drum caster is another strip caster design used to produce steel strips of thicknesses of about 0.5 to 5 mm with a width reaching about 1.8 meters. Twin Drum caster's general layout is shown in Figure 1.4. Such process involves two water-cooled counter-rotating rolls or drums. The diameter of the roll can reach about 0.5 meter. The liquid steel is fed through a refractory nozzle in-between the rolls to solidify over each roll. After steel solidification over rolls, the rolls are brought together to form the strip which is continuously withdrawn by a synchronized pinch roll. The coiler is located at the end of the process line where the strip is coiled then stored for dispatch [4].

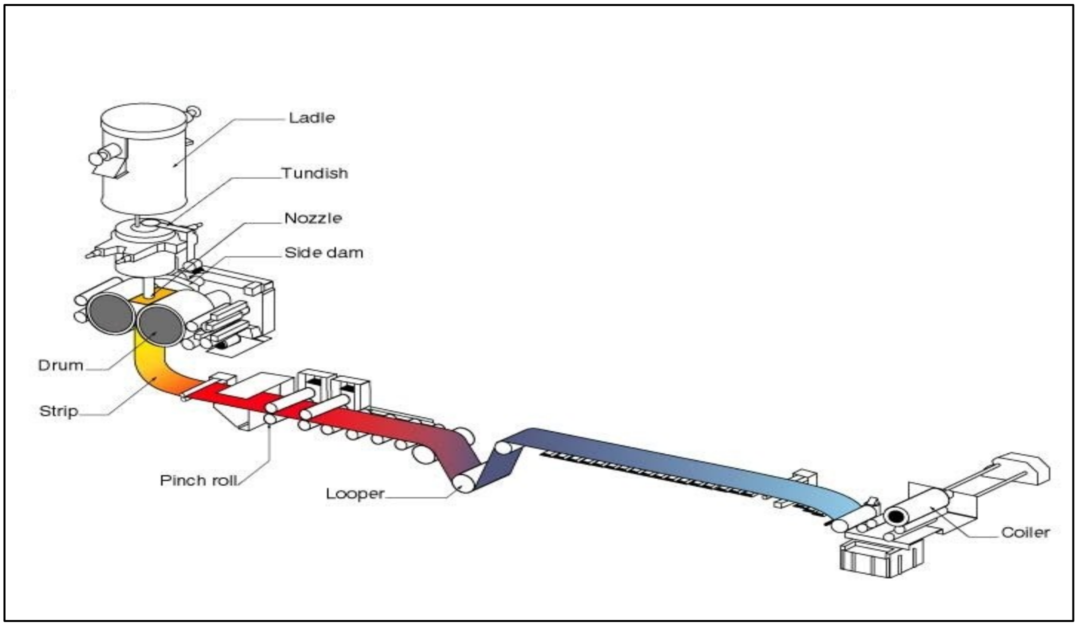

Figure 2.4: Schematic of Twin drum strip caster layout.

The main disadvantage of thin slab casters and strip casters compared to conventional casters is the low annual productivity as illustrated in Figure 1.5. Also, strip casters are not in a position to replace existing conventional casters for the mass production of commodity carbon steels but are rather suited to cast specialty steels, i.e. steels that contain less segregation due to the fast cooling of the strips. Texture control, through thermo-mechanical processes, poses another difficulty for strip casters when strip thickness is already very small [3].

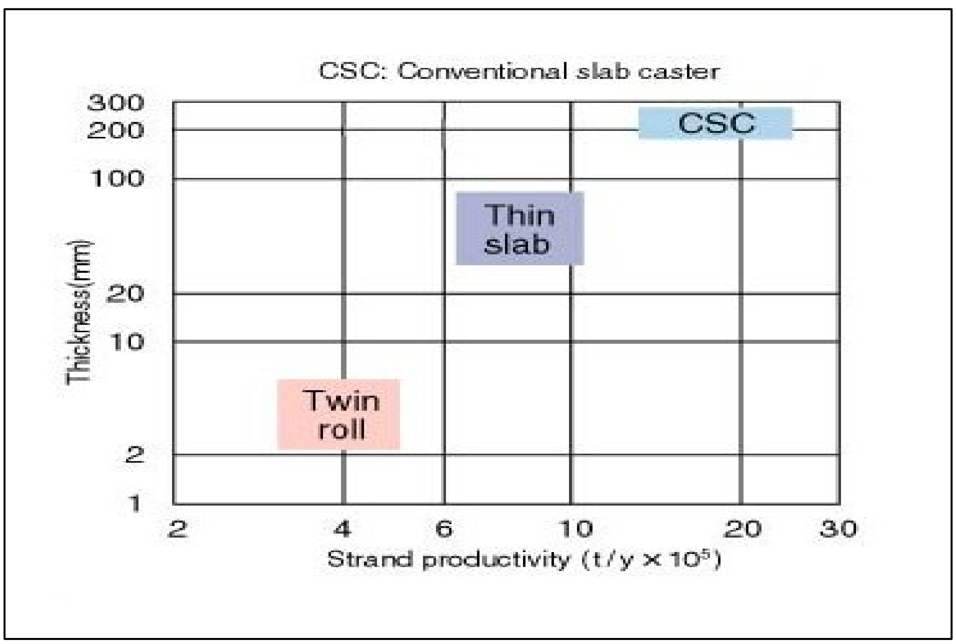

Figure 2.5: Comparison between different types of steel casters in terms of annual productivity.

1.2.3 Conventional Continuous Casting Process Description

Continuous casting process is preceded by steel making, either in Basic Oxygen Furnace (BOF) or in Electric Arc Furnace (EAF), and followed by steel secondary refining in ladle furnace or vacuum degasser. After steel refining, molten steel is transported inside a ladle toward a turret station, i.e. rotatable platform, which can hold two ladles in the same time. Later, the ladle is placed above the tundish, which is a metallurgical vessel used to continuously supply and control steel flow into the mold below. Then, liquid steel is poured continuously, via a metallurgical vessel called the tundish, into a bottomless copper water-cooled mold [4]. The flow from the tundish to the mold is gravity driven due to the difference in pressure between mold level and tundish level. Emanating molten steel flow rate can be controlled by several methods like stopper-rod mechanism and slide gate mechanism as shown in Figure 1.6.

In stopper-rod mechanism, a movable and submerged refractory rod is placed over the tundish hole to control the flow rate. While, the slide gate valve, which can be coupled with **SEN** fast exchanger, is an alternative flow control method used mainly for high productivity slab casters. The stopper-rod mechanism offers several significant advantages over slide gates like [5]:

a) Prevention of vortex formation above the tundish well when the liquid level is low, i.e. prevent slag entrainment.
b) Better sealing to avoid air aspiration or reoxidation.
c) Provision of uniform distribution of flow to SEN ports, i.e. symmetrical flow in mold.

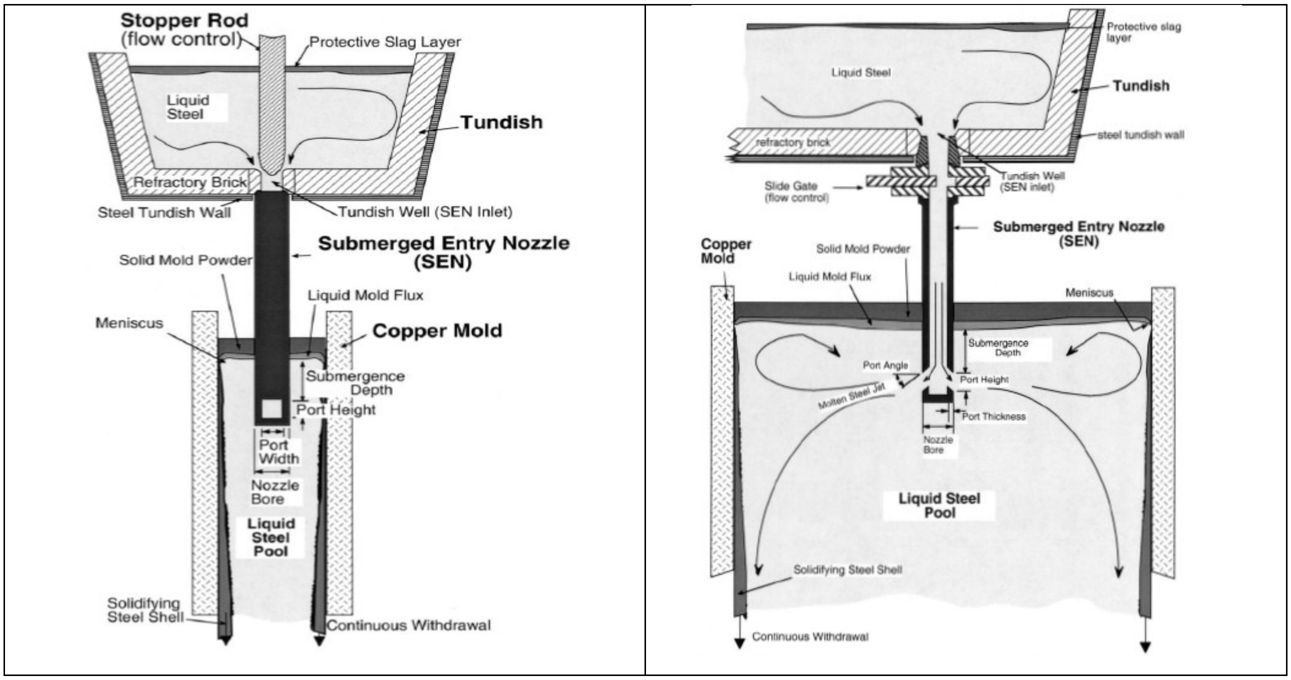

Figure 2.6: Flow control devices used in C.C. (a) Stopper-rod mechanism (b) slide-gate mechanism. [5]

Start-up of the continuous casting process requires the insertion of a starter bar or a "dummy" bar, a bar-head with a marginally smaller cross-section of the desired dimensions, connected to a withdrawal chain into the mold before molten steel pouring. Steel solidification is initiated over the dummy bar, which acts as a "temporary bottom" for the bottomless mold, prevents leakage during startup and forms a strong shell that can withhold liquid steel core during initial withdrawal process. In the mold, solidification takes place with a gradually increasing shell or solid skin. When the mold is almost full with solidifying steel pool, the starter bar withdrawal begins the continuous casting process. After the strand becomes long enough to be withdrawn by drive-rolls, the dummy bar is disconnected or cut from the fully solidified strand and removed to a parking station till next startup [4].

During casting, the mold reciprocates sinusoidally "non-harmonic oscillation" to avoid sticking, while, a powder is added to the molten steel meniscus. The powder sinters and melts to form a viscous liquid flux layer. The liquid flux layer provides lubrication effects and enhances heat transfer between the shell and the mold walls. Also, this layer augments the removal of non-metallic inclusions and prevents steel reoxidation [3].

The formed steel strand is withdrawn through a set of guiding rolls and further cooled by spraying with a water mist. As the solidified shell descends, it continues to thicken until the strand is fully solidified at the end of strand's metallurgical length[2]. After complete solidification, semi-finished products are obtained by intermittently cutting off desired lengths of the emerging strand using oxygen-acetylene torch, shear or plasma torch. Then, the products are discharged to a storage area for further thermo-mechanical processing such as rolling. For new casters and rolling complexes, an alternative way is to link the continuous caster directly to the subsequent hot rolling operation, aka hot direct rolling. Such operational link leads to savings in both energy and handling costs [5].

Conventional continuous caster configurations as well as product types have evolved in the last fifty years. Slab casters, for example, have different configurations like single strand, dual strand or multi-strands. Also, some slab casters are called combination-casters because a single strand caster can be readily modified to a twin-strand caster when required and vice versa. The general layout of a typical slab caster is shown in Figure 1.7.

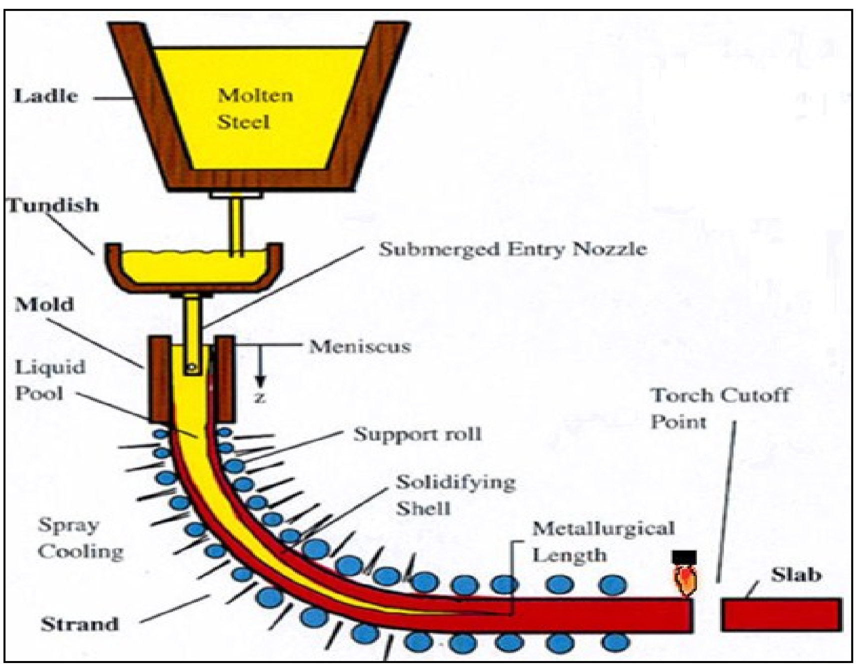

Figure 2.7: General layout of a typical slab continuous caster [5].

[2] The distance measured along the strand from the liquid level (meniscus) to a cross-sectional plane containing the assumed point of complete solidification, i.e. longest liquid core allowed by the machine design which varies with product thickness.

To increase caster utilization and annual throughput, sequential casting has been adopted by steel producers. Sequential casting involves casting a series (string) of heats in a sequence before strand(s) termination[1-2]. Effective sequential casting requires the installation of ladle rotating turret that allows fast ladle exchange, thus, continuous feeding of the caster. Another practice that enhances sequential casting is the flying tundish exchange practice, where, a standby tundish is placed on a moving platform for fast replacement of the older tundish. In addition, four-piece variable-width mold is installed in slab casters to change slab width online without the need to replace the mold [6]. Most importantly, sequential casting cannot be achieved unless a proper synchronization with steel making and ladle secondary refining is achieved. Therefore, the average casting time of a heat must be close to the average tap-to-tap time of a steel making furnace and secondary refining [7].

1.2.4 Steel Quality and Non-metallic Inclusion

Steel products with defect-free quality, viz. with uniform mechanical properties, are very essential for applications under loading and/or pressure. Surface and internal qualities of as-cast semi-finished products play a major role in the quality of final products during rolling and/or application. Thus, process optimization and defects prevention are two critical requirements for efficient continuous caster plant. Also, efficient control of different casting parameters helps in avoiding or at least reducing quality defects.

Generally, quality defects can be classified into four groups which are non-metallic inclusions, highly-localized segregation (macro-segregation), cracking and porosity. The main factors responsible for quality defects are summarized below [11-10]:

1) Inadequate preparation and handling of liquid steel can lead to ingress of air and re-oxidization, i.e. formation of non-metallic inclusions.
2) Improper composition of the liquid steel and superheat.
3) Excessive interaction between caster's mechanical equipment and the solidifying strand might induce cracking.

Deterioration of steel quality can occur due to impurities, like non-metallic inclusions, in final products. Non-metallic inclusions[3], like oxides, sulfides, and nitrides, in steel are foreign

[3] **Non-metallic inclusions** are chemical compounds and nonmetals that are present in steel and alloys.

substances that disrupt the structure homogeneity and reduce the fatigue life of steels. During deformation, either by rolling or forging, non-metallic inclusions can cause cracks in steel [9]. For example, the sliver defect is a type of surface defects that might appear in thermo-mechanical processing due to the presence of relatively large solid particles, e.g. emulsified slag or macro non-metallic inclusions, inside semi-finished products. These macro inclusions are usually located at about 15 mm below semi-finished product surface [10]. Also, entrapped inclusions form high concentrations of local internal stresses which reduce the fatigue life of final products. Therefore, the acceptable inclusion size for final products involving deep drawing is restricted to 50 micron [11].

Gas evolution from liquid steel, at the solidification front, forms voids that might get trapped below the surface of as-cast product and cause blow holes, i.e. internal defects that deteriorate product properties during rolling. Gas evolution is attributed to dissolved gas-forming elements like oxygen, nitrogen and hydrogen [9]. Oxygen certainly is the most adverse element because high levels of dissolved oxygen generated during steel making step, reacts with dissolved carbon and comes out of solution as carbon monoxide gas (CO) during solidification. Generally, steel oxygen content ranges between 0.01 – 0.10 % depending on alloying elements. Thus, lowering oxygen levels in liquid steel, through the deoxidation practice, to few parts per million (ppm) is very critical to obtain the desired metallurgical and mechanical properties of the final products [10].

Deoxidation, directly after steel making stage, is performed by adding strong deoxidizers to kill the liquid steel, i.e. remove dissolved oxygen. Oxygen affinity for different elements is given by Ellingham diagram, i.e. oxides' free energy of formations as a function of temperature, shown in Figure 2.8. In principle, all elements with a free energy of oxide formation lower than wustite (FeO) can act as deoxidizers [6]. In general, deoxidizers in steel industry are chosen for quality, availability and cost factors.

These inclusions are categorized by origin as either endogenous or exogenous.

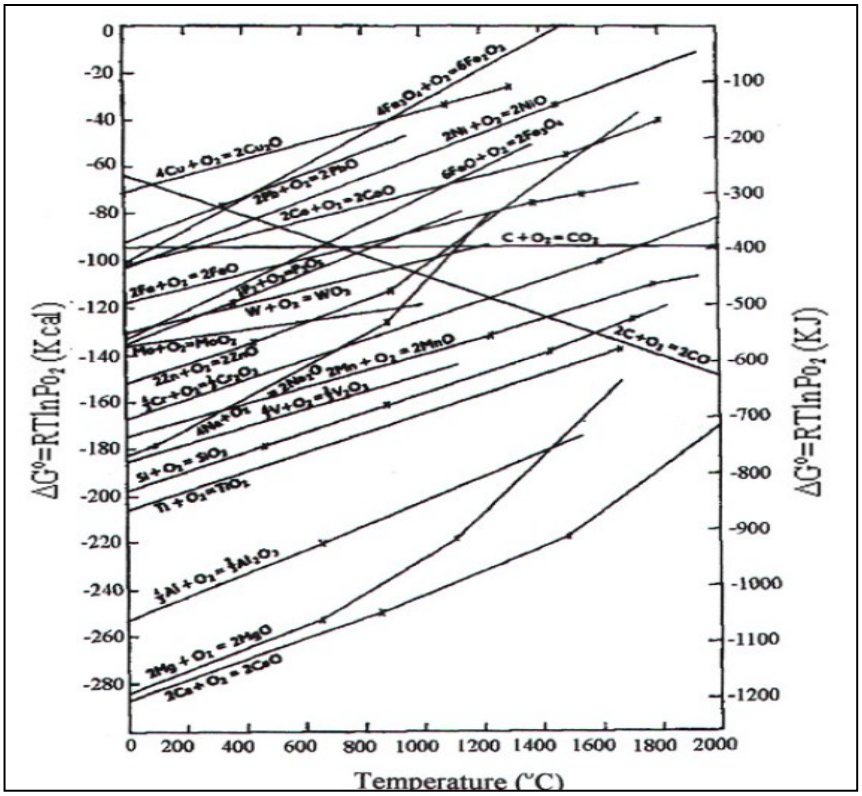

Figure 2.8: Ellingham curve for free energy of formation of oxides [6].

Deoxidizers combine with dissolved oxygen to form hundreds of thousands of non-metallic compounds (oxides) particles. The formed micron-sized inclusions, e.g. less than 50 microns, agglomerate into clusters because of turbulence and surface tension effects. These clusters float out due to density variation, i.e. slag density about 3500 kg/m^3, whereas, steel density is about 7000 kg/m^3 [7]. To enhance agglomeration and inclusion removal rate in ladle stations and vacuum degassers, gas stirring is used to reduce the number density of inclusions before casting stage. Also, slagging practices[4] support the production of high quality "clean" steels. Moreover, installation of refractory tubes, between ladle and tundish as well as between tundish and mold i.e. SEN, are used to shroud the steel stream and prevent any reaction with air or reoxidation [12].

[4] A floating flux layer over liquid steel surface, used in different metallurgical vessels, is used to prevent reoxidation, capture non-metallic clusters and provide insulation from heat losses.

1.3 Submerged Entry Nozzle Clogging Causes and Countermeasures

1.3.1 SEN and Clogging Phenomenon

The main purpose of SEN, shown in Figure 1.9, is to reduce splashing and prevent re-oxidation of molten steel during pouring from tundish into mold. SEN design can influence molten steel jet characteristics[5] as well as mold overall flow pattern. Thus, it can impact the as-cast product quality and the initial solidification of the shell. Also, surface defects, like surface cracks, may form due to severe meniscus fluctuations which are influenced by SEN design. Avoidance of slag emulsification, prevention of meniscus freezing and promotion of inclusion flotation are all significant objectives of SEN. Hence, optimal SEN design should provide symmetric distribution of molten steel as well as reduce turbulence and surface fluctuations inside the mold [5].

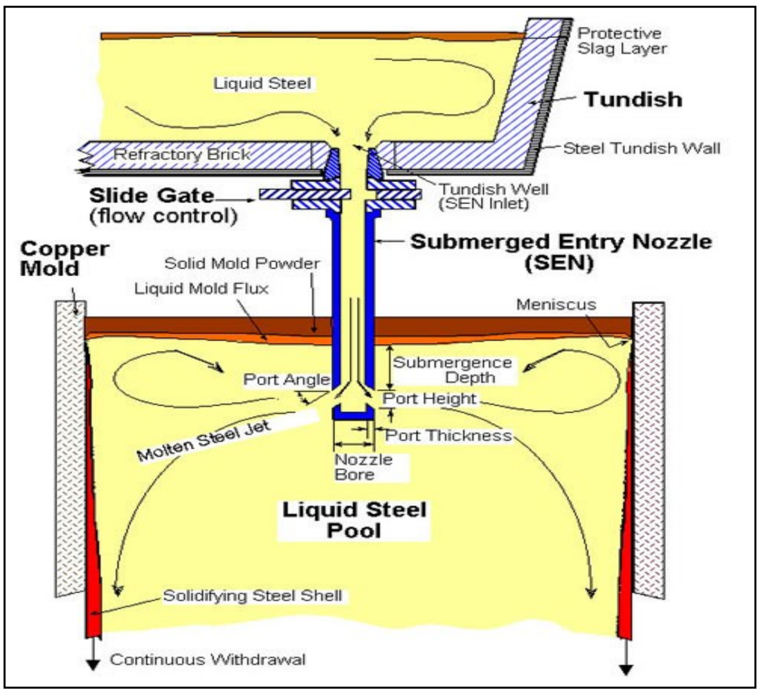

Figure 2.9: Schematic of C.C. main equipment and nomenclature [5].

There are different designs and sizes of SEN depending on the as-cast product shape and caster's productivity respectively. Caster's semi-product shape generally determines the optimum SEN design for delivering the desired symmetrical distribution of flow. For example, the umbrella- design is used with round billet casters, whereas, the relatively thin tri-ported SEN is used with thin slab casters. In billet and bloom casters, where the flow is evenly distributed to the four sides, SEN with four-ports is usually utilized. In slab casters, bifurcated SENs, Figure 2.10,

5 Jet characteristics include jet speed, angle, turbulence effects and impingement point onto narrow mold

are preferred to deliver the desired symmetric flow toward both narrow faces. The bifurcated SEN is preferred over the straight tube in slab casters because it speeds up the initial solidification at mold walls, reduces steel splashing and prevents meniscus freezing by delivering molten steel to top level effectively. Also, the quality of final cold sheet have improved with bifurcated nozzles, compared to straight nozzles, which indicate higher removal rates of non-metallic inclusions [4-5].

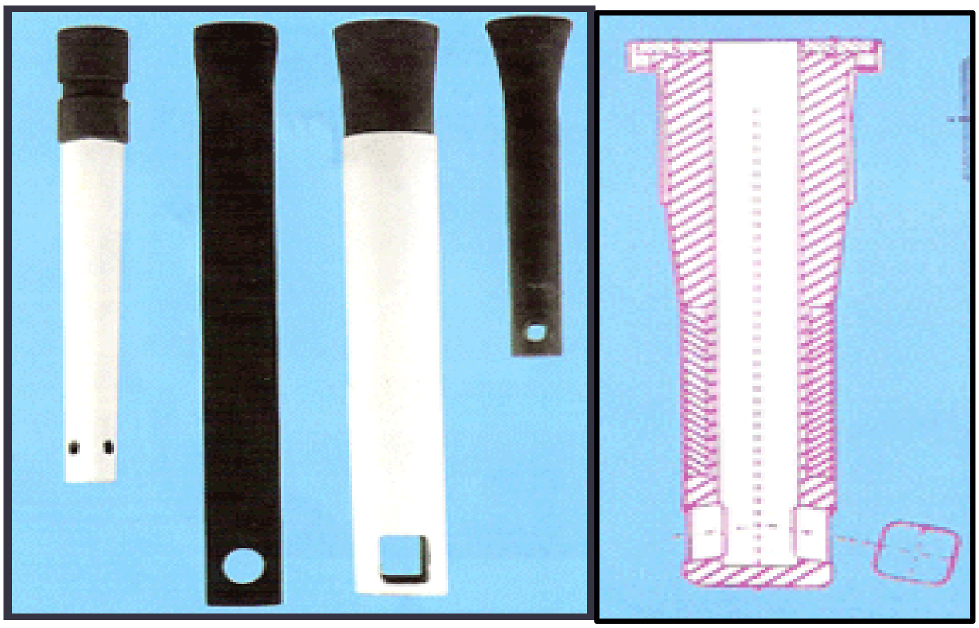

Figure 2.10: Different designs of bifurcated SEN used in steel casters.

Originally, silica-fused nozzles were used for casting Al-killed steels, but due to severe clogging, it was replaced with other materials. Nowadays, a typical iso-statically pressed SEN is made from a refractory mix; see Table 2.1, which mainly contains alumina-graphite (Al_2O_3-C). In addition, a special protective insert made of Zirconia is placed externally near slag-line to reduce SEN erosion or wear due slag's chemical attack [32-35]. Other optimal requirements of SEN design are low porosity to prevent air ingress, good thermal shock resistance to avoid cracking and reasonable price [14-17, 20].

Table 2.1: Typical composition of iso-statically Alumina-graphite SEN.

Component	Weight %
Al_2O_3	62-66

C (Graphite)	20-25
SiO_2	3.8
ZrO_2	4.6
TiO_2	1
FeO_3	0.3
MgO	0.4
Si	1

Unfortunately, SEN clogging is a major bottleneck in modern continuous casters. Clogging can have detrimental effects on both steel quality and caster productivity. It disturbs the castability of molten steel and interrupts sequential casting. Clogging is caused by the adhesion and sintering of non-metallic inclusions, formed by deoxidation or reoxidation, to the internal circumferential surface of SEN. Clogging reduces caster's throughput by gradually chocking molten steel flow passage till complete blockage. Also, product quality is affected by dislodged clog particles and induced turbulence at meniscus level that might lead to slag or flux entrainment inside the solidified shell. Clogging plays a strong role in the formation of surface defects caused by undesired flow patterns or asymmetry inside the mold. Transient flow also encourages irregular temperature distribution with a possibility of shell breakout. Furthermore, frequent replacement of clogged nozzles and associated tundish refurbishment add extra cost for maintenance. Elimination of clogging surely will alleviate previous disadvantages and increase casting time and production [15-17, 22].

1.3.2 SEN Clogging Types and Causes

SEN clogging occurs most profoundly during Al-killed steels casting as well as in steels deoxidized by Ti, Zr and rare earth metals [26]. For example, a clog sample from Alumina-graphite SEN is shown in Figure 2.11. This clog is caused by agglomeration of alumina inclusions during LCAK steel casting.

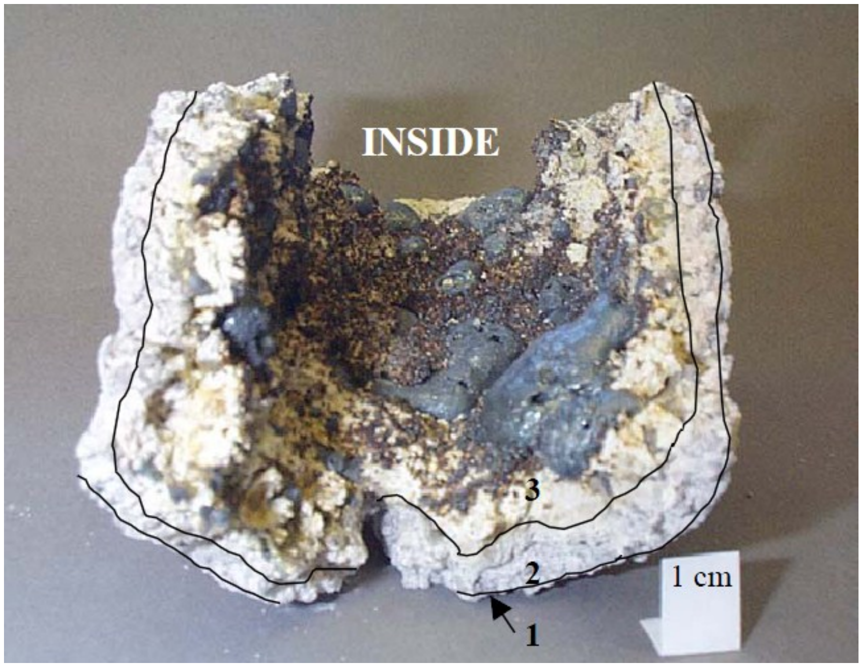

Figure 2.11: Clogging deposit with grey solidified steel over it. Note: three layers of clog with different thicknesses are indicated, whereas, SEN wall is removed [26].

SEN clogs are classified into four different types according to their formation mechanism. In fact, two or more mechanisms can contribute to a given clog, thus, pinpointing the exact source is a difficult task. Clogging can be generated from the following sources [15-17,19]:

a) Transport of inclusions, especially Alumina, existing in molten steel to nozzle wall.

A clog can occur as a result of inclusions agglomeration and attachment to SEN internal surface. Inclusions existing in steel prior to casting are commonly formed during calcium treatment modification, reoxidation of molten steel and deoxidation stage. Reoxidation can happen during ladle and/or tundish filling or through reaction with tundish or ladle flux before casting. Also, exogenous inclusions like refractory particles and entrapped slag from tundish or ladle can pass through the nozzle [9-11].

Both surface tension effects, between non-metallic particles and refractory wall, and poor wettability[6] of molten steel over refractory material support the formation of voids and consequently the attractive forces between inclusions and refractory. Also, impaction by turbulent eddies as well as high wall roughness are considered additional causes that support attachment. Moreover, hydrodynamic effects where the velocity is about zero, at the nozzle surface and at the separation points, aid the attachment of inclusions to refractory wall followed by high temperature sintering [15-17]. The attachment of alumina inclusions to Alumina-graphite SEN wall is shown in Figure 2.12.

Sintered clusters in SEN inner circumference form an irregular network that grow over time and block the orifice. Based on a study [15], 16% of the total inclusion population in the melt is sufficient to form the clog.

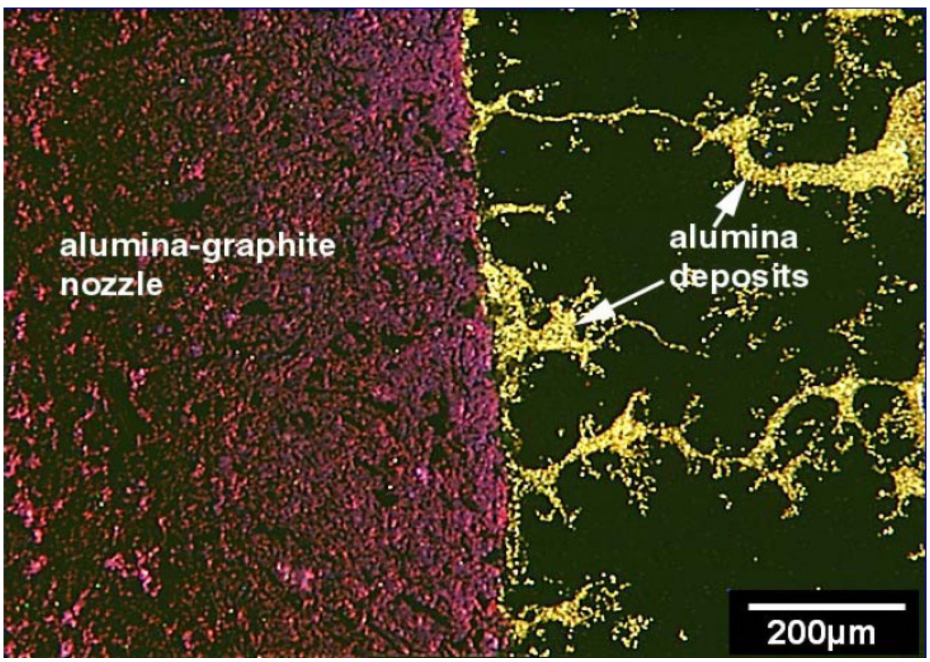

Figure 2.12 : Formation of alumina network accretion over Alumina-graphite nozzle [27-28].

b) Ingress of air into the nozzle, i.e. reoxidation inside SEN.

Reoxidation of steel through the local reaction of dissolved aluminum inside SEN can generate large alumina inclusions that readily clog the nozzle. Due to the applied local flow restriction, that causes "venturi effect" phenomenon, the pressure drops to below 1 atmosphere.

---

6 Alumina and liquid steel have a high contact angle (between 136 -146 Degrees) which implies a non-wetting condition of the refractory surface. Therefore, Alumina inclusions will be attracted to SEN refractory surface to minimize contact with steel.

Therefore, air can be sucked into nozzle through connections, cracks and/or nozzle pores because of the large pressure drop especially in the region immediately below the flow control devices. The minimum pressure inside SEN is affected by several factors like tundish path depth, casting speed, and clogging degree for specific SEN dimensions. Also, oxygen concentration gradient near SEN wall can influence steel surface tension. Surface tension difference may lead to inclusions attachment in non-recirculation and/or low turbulence regions. Clogs caused by reoxidation are identified by large-structured dendritic inclusions and nitrogen pickup between tundish and mold [13-17, 23].

c) Chemical reaction between the nozzle refractory and the molten steel.

Chemical reactions between nozzle material and molten steel can be the source for uniform film layers adjacent to SEN orifice, in comparison with sintered network in some clogs. SEN components, such as SiO_2 and Al_2O_3, can be reduced by graphite. Reduction of silica forms gaseous sub-oxides or compounds like SiO and CO inside refractory material. These compounds are sucked toward the molten steel/refractory interface, due to the low pressure inside SEN, and react with dissolved aluminum to form Alumina over refractory wall [19,21].

d) Steel solidification inside the nozzle.

Some clogs are associated with skull formation due to steel solidification inside SEN during casting. Insufficient SEN pre-heating[7] at startup can lead to steel solidification on refractory wall that is significantly below the solidus temperature of steel. Normally, incoming molten steel from tundish melts such layer within few minutes; however, clogging buildup may inhibit total removal of steel skull. Moreover, low superheat and large solidification range of an alloy can aid a relatively faster skull formation and associated clogging. In addition, molten steel entrapment followed by solidification at low flow regions can enforce clog network and enhance its growth. As this mixed network of sintered inclusions and skull acts as a filter for inclusions in liquid stream.

[7] SEN preheating should be for about 1 hour to reach a maximum temperature of 723 C.

1.3.3 Clog Detection in Casters

Timely stoppage of the industrial caster before severe SEN clogging, which affects both yield and quality, requires precise methods for early detection of a clog. The following methods are helpful in early detection of SEN clogging [13-17]:

a) Nitrogen Pickup

Increase of nitrogen (ppm) in mold samples indicates nitrogen pickup from the atmosphere; thus, a high possibility of reoxidation and clog formation. Based on an analytical model, nitrogen pickup of 5 ppm accumulated over seven 250-ton heats is sufficient to generate reoxidation inclusions of 5.1 kg that form a 20 mm clog layer [17].

b) Mold level Fluctuations

SEN clogging disturbs the constant flow rate from tundish to mold and cause transient flow asymmetry in the mold. The disturbance of mass flow rate is manifested as mold level fluctuations, shown in Figure 2.13. To overcome such disturbance, the flow control device, which is linked to mold's level sensor, tries to stabilize the flow and reduce these fluctuations. Since level fluctuations, can be affected by other factors such as mold oscillator parameters, clog detection should not depend solely on this detection method [23].

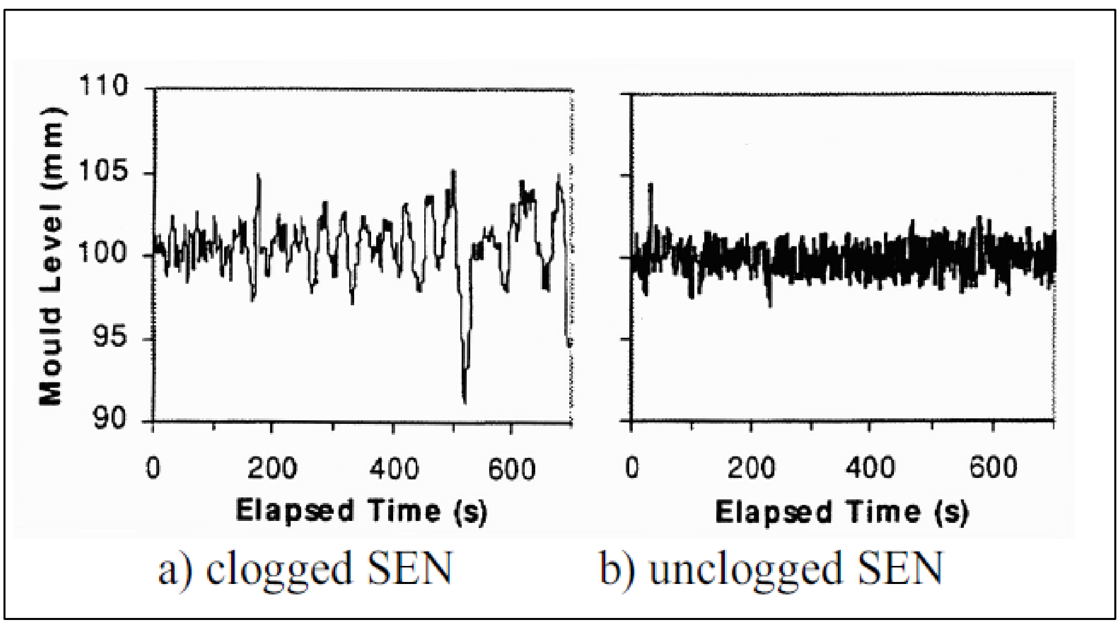

Figure 2.13: Effect of clogging on mold's level fluctuations [45].

c) Position of control device relative to casting speed

Flow control devices, i.e. slide gate and stopper rod, have a correlated position[8] or opening for the prescribed casting conditions. These prescribed casting conditions include fixed tundish path depth, constant casting speed, constant gas injection and product dimensions. The symmetrical buildup around SEN orifice, which usually starts at stagnation areas, reduces the effective bore diameter and steel throughput. Hence, the flow control device will open gradually to provide the required mass flow and to compensate for the drop in mold level. The deviations of actual device position from the correlated position can indicate the clog severity. Therefore, monitoring device's real-time position can be an important method for detection [23].

d) Argon back pressure

For casters using argon injection, see section 1.3.5, backpressure of argon-line has a set value based on argon flow rate and casting conditions. Erratic fluctuations or abnormal low back-pressure indicates a high possibility of air aspiration from a crack or a leak in SEN. Whereas, high back-pressure, caused by resistance to argon flow, signifies a clogging problem. Therefore, argon back-pressure is another important method to identify clogging [23].

1.3.4 Methods to Reduce Clogging

Several methods have been implemented to reduce inclusion deposition on SEN walls like enhancement of steel cleanliness, calcium treatment, modification of SEN material/geometry and argon injection. Steel cleanliness can be improved by efficient removal of inclusions through better ladle refining, i.e. vacuum degassing or argon stirring. Also, optimization of tundish flow pattern, by impact pads and baffles to reduce vortexing and high turbulence, promotes inclusion agglomeration and flotation. In addition, reoxidation inclusions, prior to casting, can be eliminated by submerged pouring from ladle to tundish and by applying protective flux layers over vessels.

Calcium treatment is carried out by adding calcium to liquid steel during secondary refining in ladle furnace to liquefy solid alumina by forming liquid calcium aluminates. It is a good method to reduce SEN clogging when mass ratio of alumina to calcia is about 1:1.

[8] Clogging factor is used for real time tracking of clogging in casters which correlates casting speed, flow device position, tundish path depth, argon injection flow rate for a given SEN geometry.

Unfortunately, insufficient calcium can aggravate clogging due to the formation of solid inclusions like solid alumina rich in $CaO.Al_2O_3$. On the other hand, excessive amount of calcium may generate calcium sulfides. Therefore, optimum calcium treatment should be after desulfurization step when steel sulfur content is below 0.007% [24-25, 27-29].

Modification of SEN material can be done by replacing or improving SEN refractory material. Reducing refractory potential oxygen sources or impurities, like sodium oxide, potassium oxide and silica, is critical to avoid the formation of gaseous suboxides that enhance clogging. Also, SEN made from doloma (MgO-CaO) with calcia (> 50%) can liquefy solid alumina to prolong nozzle life. However, wall erosion due to calcia diffusion is a disadvantage of this material. Recently, the promising calcium titanate and calcium zirconate are explored as potential alternatives for the widely used alumina-graphite SEN for aluminum killed steels [28]. Similarly, several refractory inner-surface coatings had been examined to improve castability like calcia (CaO) and boron nitride (BN) coatings which reflected a better SEN life [29-31].

Nozzle geometry modifications involves oversizing of SEN bore to accommodate for clog buildup and prolong casting. Also, incorporation of a five millimeter annular step at SEN's mid-height increases turbulence in central region to promote clogging detachment. Moreover, geometrical modification by the removal of stagnation areas, which are prone to clog buildup, can enhance SEN life. For example, elimination of nozzle-well in bifurcated SEN, where the nozzle ports coincide with the pore internal bottom, might reduce clogging [38-39].

Finally, argon injection, discussed in next section, is a widely used method to reduce clogging and to improve both cast quality and caster productivity.

1.3.5 Argon Injection into SEN Molten Stream

Argon is utilized in high temperature metallurgical processes like molten steel stirring and shrouding, due to its inertness, insolubility and inexpensive production, in comparison with other inert gases. Also, argon injection is used to reduce SEN clogging in industrial continuous casters. Injection can be done at different locations such as SEN connections, drilled grooves of slide gate or circumferential porous slits in SEN as shown in Figure2.14 [44]. Also, argon can be introduced through the porous plug of a stopper-rod as shown in Figure 2.15 [7, 79].

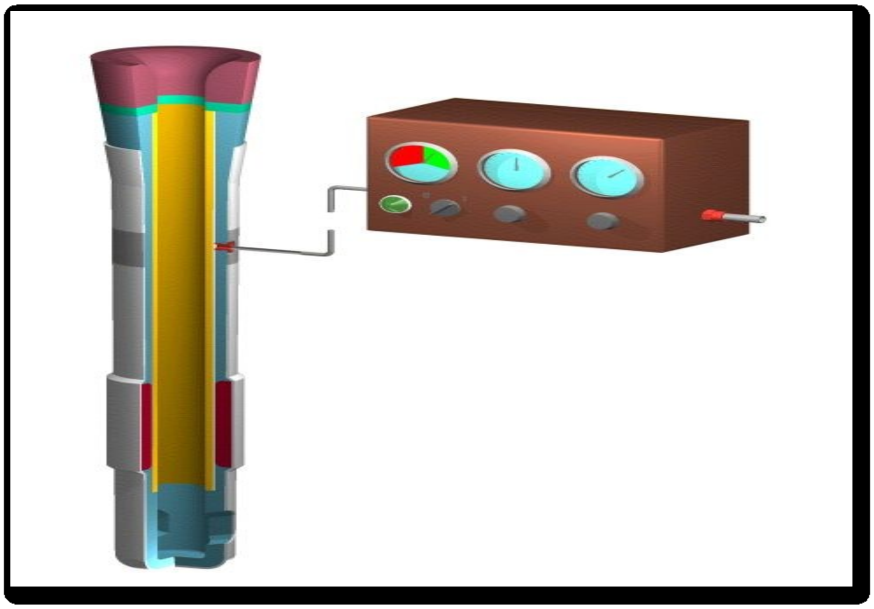

Figure2.14: Argon injection through SEN circumferential porous slits [44].

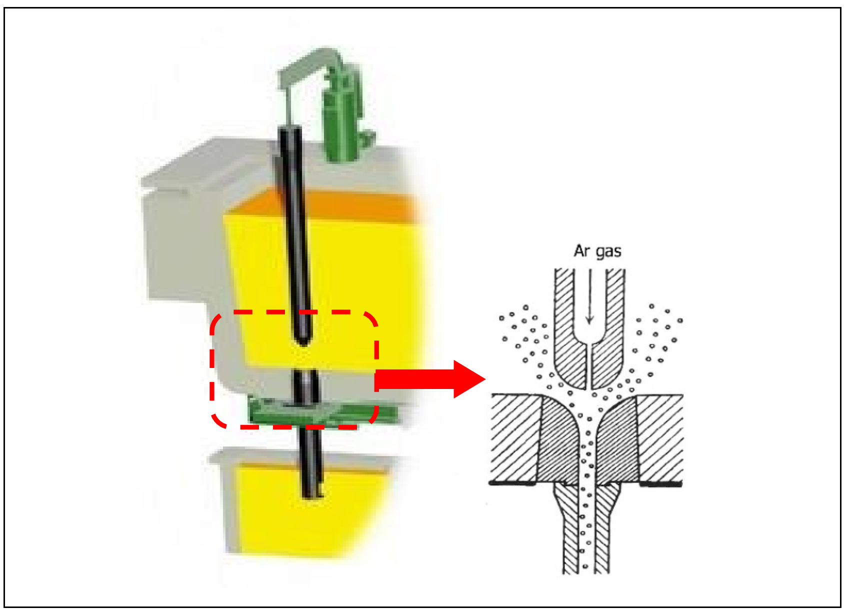

Figure 2.15: Argon injection through the porous plug of a stopper-rod [7].

Argon injection possible benefits can be summarized as following [17, 23, 36-37]:

A. Enhances agglomeration of non-metallic inclusions.
B. Enhances flotation of inclusions that attach to bubbles as shown in Figure 2.16.
C. Prevents meniscus freezing especially at relatively low superheats.
D. Increases the minimum pressure inside SEN, thus, prevent deposition of reoxidatized inclusions.

E. Increases turbulence to flush fragile inclusion networks from SEN wall.
F. Hinders chemical reactions between steel and refractory wall.
G. Promotes powder flux melting and retard the solidification of liquid flux layer.

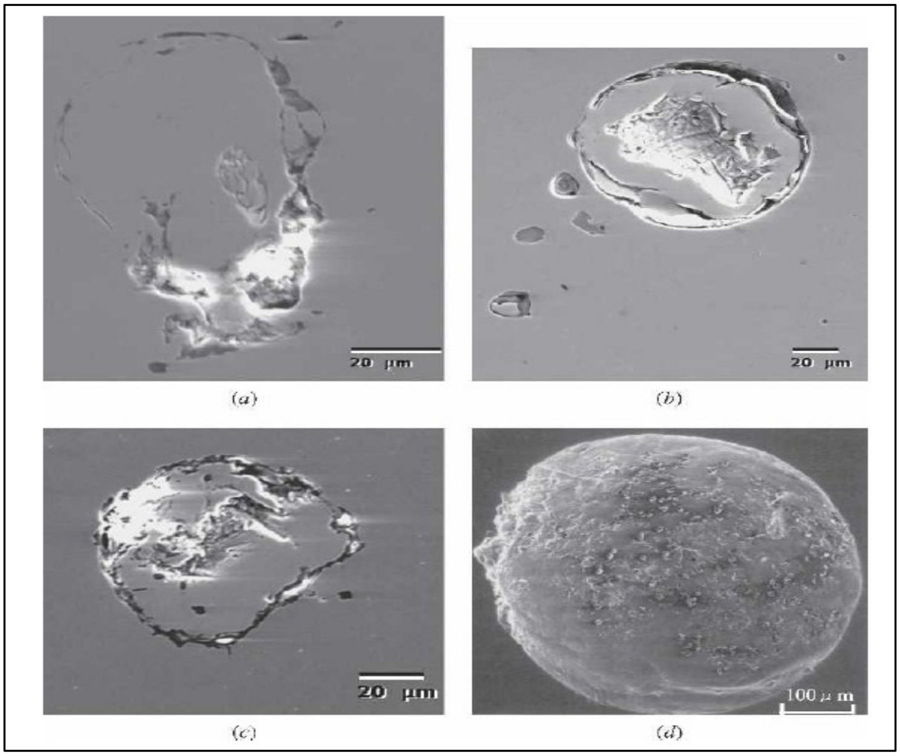

Figure 2.16: Inclusions attachment to bubble surface (a-d) [40-41].

Proper calibration of injection by maintaining at least one atmospheric pressure inside SEN, in conjunction with casting speed and tundish path depth, is essential to optimize inclusion removal, prevent clogging and reduce occurrence frequency of quality defects. These performance criteria can be achieved by increasing the interfacial gas/steel area, i.e. generation of fine bubbles.

Albeit the numerous advantages of argon injection, improper injection flow rate can lead to some types of internal and surface quality defects due to bubble entrapment inside steel shell and/or slag layer disturbance. Excessive gas flow rate may create abnormal top level fluctuations that cause severe erosion of SEN protective slag-line layer and possible slag entrainment. Slag emulsification or engulfment in the solidified shell, seen in schematic Figure 1.18, lead to a surface defect called sliver in the rolled products. This defect is usually located at about 15 mm below the surface as shown in Figure 1.17 (a) [43].

Also, entrapment of insoluble argon bubbles inside the solidified shell lead to the formation of a surface defect called pinhole. When the entrapped bubble is coupled with inclusions, the defect is called pencil pipe or pencil blisters. Pencil blisters are line defects in the rolled products in the form of elongated tubular-shaped surface, seen in Figure 1.17 (b) [40-43, 59].

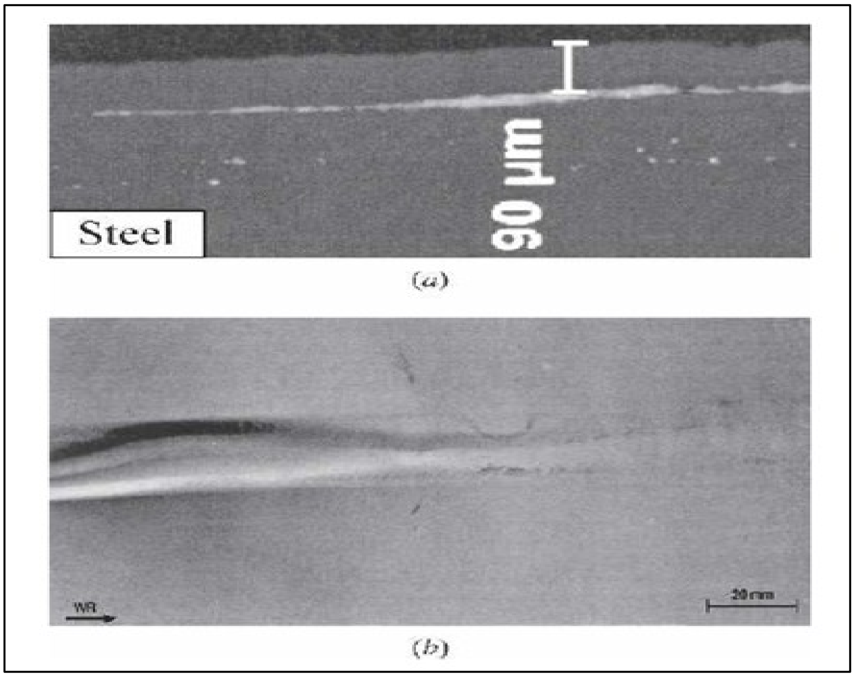

Figure 2.17: (a) Sliver defect in a rolled sheet [43] (b) Pencil blister defect on a steel sheet [41]

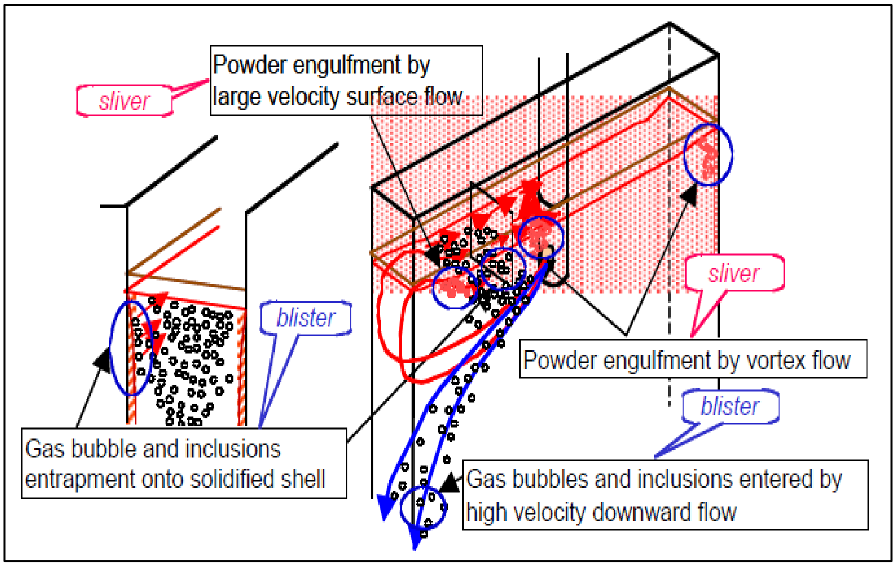

Figure 2.18: Schematic view of molten steel flow and origins of surface and internal defects.

Understanding argon injection effects on flow, in both SEN and mold, is important to optimize injection parameters and performance. Analysis of liquid steel-argon gas flow experimentally in steel casters is not feasible because it's expensive, dangerous and impossible to visualize or measure. Therefore, researchers employed physical gas-water models, where gas phase can be air, argon or nitrogen, to study the two-phase flow. Physical models of different scales based on similarity criteria are reported in literature. These physical models utilize water due to the comparable kinematic viscosities of molten steel and water of about $1x10^{-6}$ m^2/s. Also, these models employ visualization systems, e.g. Particle Image Velocimetry (**PIV**) and Laser Doppler Velocimetry (**LDV**), to obtain flow pattern and velocity fields [39, 46-50]. Moreover, many researchers have adopted Computational Fluid Dynamic (**CFD**) multi-phase models to study the molten steel-argon flow inside SEN and mold configuration. These models take into account heat transfer and steel properties in comparison to physical gas-water models.

Argon injection supports the removal of nozzle clogging which is caused by the adhesion of inclusions to SEN internal surface. Therefore, argon injection is very beneficial for the extension of SEN life. Also, argon injection encourages mixing of molten steel to enhance the homogeneity of temperature and composition. Unfortunately, several quality defects, sliver and blister defects, have been linked to argon injection.

Understanding the effects of argon injection on flow and temperature fields in both the SEN and the mold region of a continuous steel caster is important to optimize injection parameters and to improve performance and cast quality. Experimental analysis of liquid steel-argon gas flow in commercial sized casters is not practically feasible because such experimental campaigns are expensive, dangerous and impossible to visualize or measure.

1.4 Thesis Objectives

The main goal of this thesis research is to qualitatively understand through 3D CFD modeling the behavior and influence of argon bubbles on the two-phase flow in a slab continuous caster. This numerical parametric study is carried out for a specific slab caster incorporating the Discrete Phase Model (**DPM)** and k-ω turbulence model. The main objectives of this research encompass the following items:

a) Investigate the flow patterns inside SEN/mold configuration with and without gas injection.
b) Study injection rate effects on molten steel-argon gas flow for different casting conditions.
c) Study bubble size effects on molten steel-argon gas flow for different casting conditions.
d) Estimate superheat dissipation rates at mold's upper region under the influence of argon injection.
e) Analyze meniscus surface velocity and temperature distribution under the influence of different casting and injection conditions.

Chapter 2: Literature Review

2.1 CFD Modeling Fundamentals

2.1.1 CFD Background

CFD encompasses the study field of fluid mechanics using modeling and numerical methods. Nowadays, this acronym is directly related to commercial software packages such as ANSYS-FLUENT. CFD has the potential to provide a great amount of data inexpensively compared to experiments. CFD codes solve the basic Partial Differential Equations (PDEs) derived from the three governing laws of conservation of a physical system. These equations are derived through Reynolds transport theorem and are [51-53]:

A. Conservation of mass (continuity equation in 3D Cartesian coordinates):

$$\frac{\partial \rho}{\partial t}+\frac{\partial(\rho u)}{\partial x}+\frac{\partial(\rho v)}{\partial y}+\frac{\partial(\rho w)}{\partial z}=0 \tag{2.1}$$

for incompressible fluids; $\frac{\partial \rho}{\partial t}= 0$

B. Conservation of momentum (Newton's second law):

For incompressible, viscous newtonian fluid, the conservation of momentum equations are called Navier-Stokes equations (2.2)-(2.4). For three dimensional Cartesian coordinates, the equations are:

$$\text{X - momentum}: \rho\frac{\partial u}{\partial t}+\rho u\frac{\partial u}{\partial x}+\rho v\frac{\partial u}{\partial y}+\rho w\frac{\partial u}{\partial z}=-\frac{\partial \hat{p}}{\partial x}+\mu\left[\frac{\partial^2 u}{\partial x^2}+\frac{\partial^2 u}{\partial y^2}+\frac{\partial^2 u}{\partial z^2}\right]+S_{Mx} \tag{2.2}$$

$$\text{Y - momentum}: \rho\frac{\partial v}{\partial t}+\rho u\frac{\partial v}{\partial x}+\rho v\frac{\partial v}{\partial y}+\rho w\frac{\partial v}{\partial z}=-\frac{\partial \hat{p}}{\partial y}+\mu\left[\frac{\partial^2 v}{\partial x^2}+\frac{\partial^2 v}{\partial y^2}+\frac{\partial^2 v}{\partial z^2}\right]+S_{My} \tag{2.3}$$

$$\text{Z - momentum}: \rho\frac{\partial w}{\partial t}+\rho u\frac{\partial w}{\partial x}+\rho v\frac{\partial w}{\partial y}+\rho w\frac{\partial w}{\partial z}=-\frac{\partial \hat{p}}{\partial z}+\mu\left[\frac{\partial^2 w}{\partial x^2}+\frac{\partial^2 w}{\partial y^2}+\frac{\partial^2 w}{\partial z^2}\right]+S_{Mz} \tag{2.4}$$

The terms in above equations denote that velocity rate of change (local acceleration) plus three terms for transport due to convection equals pressure forces (pressure gradient) plus diffusion/viscous forces plus source terms.

C. Conservation of energy (1st law of thermodynamics):

First law of thermodynamics[9] postulates that rate of change of energy of a fluid particle equals the rate of heat addition plus the rate of work done on it assuming that heat transfer is governed by Fourier's law of heat conduction[10]. Also, viscous stresses represent the viscous dissipation function since viscosity cannot add energy to the system i.e. conversion of mechanical energy into heat.

$$\begin{aligned}\rho\frac{DE}{Dt} = &-\mathrm{div}(p\mathbf{u}) + \left[\frac{\partial(u\tau_{xx})}{\partial x} + \frac{\partial(u\tau_{yx})}{\partial y} + \frac{\partial(u\tau_{zx})}{\partial z} + \frac{\partial(v\tau_{xy})}{\partial x}\right. \\ &\left. + \frac{\partial(v\tau_{yy})}{\partial y} + \frac{\partial(v\tau_{zy})}{\partial z} + \frac{\partial(w\tau_{xz})}{\partial x} + \frac{\partial(w\tau_{yz})}{\partial y} + \frac{\partial(u\tau_{zz})}{\partial z}\right] \\ &+ div(k\ grad\ T) + S_E\end{aligned} \tag{2.5}$$

These equations are considered the backbone of all CFD commercial packages for fluid motion description. The main three unknown quantities (variables) that are simultaneously derived from the above laws are velocity, pressure and temperature. Likewise, the final discretized forms of these PDEs contain other thermodynamic properties: density and enthalpy, and transport properties of a fluid: conductivity and viscosity. By solving these PDEs numerically using CFD codes, all required variables can be deduced.

Furthermore, at low speeds, i.e. Mach number (Ma) < 0.2, fluids can be considered incompressible. So, the energy equation is not linked to mass and momentum equations. While for Ma>0.2, equations of state like perfect gas law, under the assumption of equilibrium, are used to obtain required variables for compressible fluids. In addition, conservation of species and chemical reaction laws are added to CFD codes to account for the effects of diffusion and reaction between elements in multi-component reacting fluids. Auxiliary relations such as diffusion coefficients, chemical equilibrium constants, heats of formation and reaction rates are required for the solution of such modeling problems

2.1.2 Turbulence Modelling

Many fluid flows in industry are considered turbulent including molten steel flow in continuous casting (CC). The dimensionless number that gives distinction between different flow

[9] Energy (E) = Internal energy (thermal) (i) + Kinetic Energy (½ $(u^2+v^2+w^2)$) .
[10] $q = -k\ \nabla T$; relates the heat flux to the local temperature gradient.

regimes, either laminar, transition or turbulent, is the dimensionless Reynolds[11] number (**Re**). In C.C., **Re** of molten steel flow, which falls in the turbulent regime, ranges between 90,000 to100,000 depending on inlet velocity. Turbulence is characterized as an irregular flow that is treated statistically. In a turbulent flow, unsteady vortices appear on many scales and interact with each other. It leads to chaotic property variations due to low momentum diffusion, high momentum convection, and rapid variation of both pressure and velocity in space and time. Therefore, turbulence enhances rapid mixing and increases rates of mass, momentum and energy transports.

Turbulence is taken into account during CFD simulations through turbulence "models". There are three classes of turbulence models in CFD codes which are Direct Numerical Simulation (DNS), Large Eddy Simulation (LES) and Reynolds Averaged Navier-Stokes (RANS) models [51]. LES and RANS are used to model the expected influence or impact of turbulence on flow domain. Selected turbulence simulation class has a huge impact on solution accuracy and computational cost. For instance, DNS class, the most accurate, requires relatively large number of cells to capture turbulent eddies and their motion with time. In contrast, RANS turbulence models are used to predict turbulence effects in fluid flow without resolving all scales of the smallest turbulent fluctuations. The time-averaged RANS models yield reasonably accurate results with less computational cost [52]. Also, Thomas et al. compared LES and RANS results with experimental measurements of water models and found close match [55]. These models require additional PDEs, e.g. turbulent kinetic energy and its dissipation rate, to represent the turbulent properties of the flow.

Most prominent RANS models in CFD literature are eddy-viscosity models like (k-ε) and (k-ω) models [53]. In here, k is the turbulent kinetic energy and ε the dissipation rate of the turbulent kinetic energy, while, ω is the specific turbulent dissipation rate or turbulent frequency. Eddy-viscosity models are based on Boussinesq's hypothesis which assumes that the momentum transfer caused by turbulent eddies can be modeled with turbulent viscosity (μ_t) [52]. Also, these models integrate turbulence effects on flow momentum by replacing the molecular viscosity (μ) with the effective viscosity, $\mu_{eff=}$ μ+ μ_t, in the time-averaged RANS equations [52].

[11] Reynold number ($Re = \frac{\rho * v * L}{\mu}$): measure of the ratio of **inertial forces** to **viscous forces** for given flow.

2.1.3 Near-wall Region of Bounded Flow.

Fluid flows are significantly affected by the presence of walls, thus, wall-bounded flows need careful treatment in CFD turbulent models. At the near-wall region, solution variables have large gradients, and the momentum and other scalar transports vary strongly. Accordingly, accurate representation of flow in the near-wall regions determines successful predictions of wall-bounded turbulent flows. The near-wall region, also called inner layer, can be subdivided into three layers, Figure 2.1, which are [72]:

a) Viscous sub-layer.

At the wall, the no-slip condition affects the mean velocity field sharply, where; viscous damping reduces the tangential velocity fluctuations at this innermost layer. The flow is approximately laminar and molecular viscosity plays a prevailing role in momentum and heat transfer.

b) Fully-turbulent (log-law) layer.

This layer is the outermost layer of the near-wall region. Turbulence plays a major role in this layer due to production of turbulence kinetic energy which is caused by the large gradients of the flow velocities.

c) Buffer layer.

Buffer layer or blending region is located between the viscous sub-layer and the fully turbulent layer. In this layer, effects of molecular viscosity and turbulence are just as important.

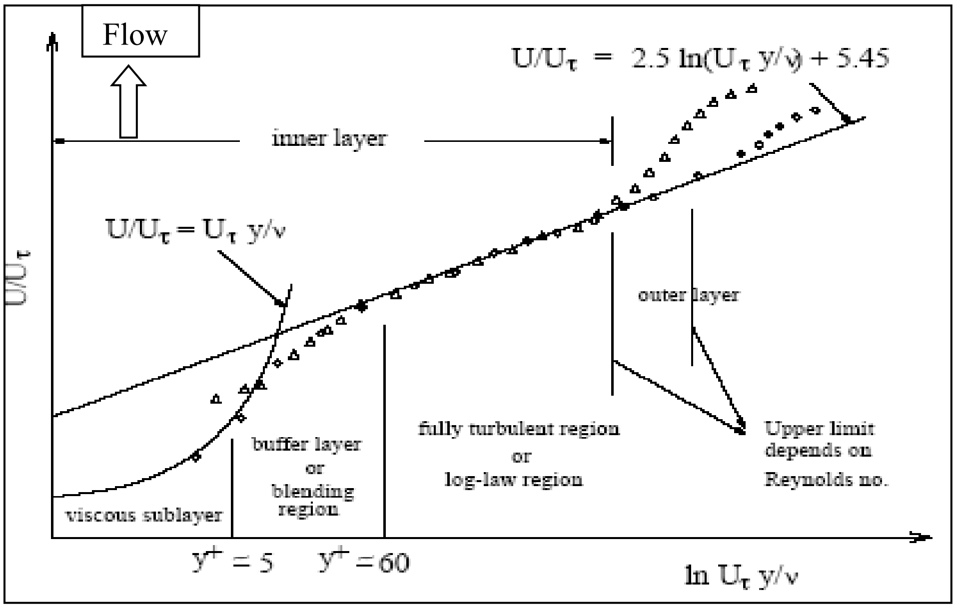

Figure 2.1: Schematic of the subdivisions of the near-wall region (in semi-log coordinates) [72].

Customarily in commercial CFD packages, two main approaches, Figure 2.2, are utilized to simulate wall-bounded flows and incorporate turbulence effects at the near-wall region. The two main approaches are described below namely [72]:

A. Wall function approach

Wall functions, which are semi-empirical formulas, are integrated into the code to account for viscosity-affected inner region, i.e. viscous sub-layer and buffer layer, influence on the fully-turbulent layer. Hence, high resolution near walls and modification of turbulence model formulation are not required. This approach saves computational resources and generates reasonably accurate solution especially for industrial flow simulations. However, this approach is not accurate to represent the flow when pressure gradients are large and low-Reynolds-number effects are pervasive like in fluid flow through a very small gap/hole or in the case of highly laminar flow.

B. Near-wall model approach

Near-wall model approach is used to overcome limitations of wall-function approach. In this approach, the turbulence models are modified to enable the viscosity-affected region, also called low-Re region, to be resolved with a fine mesh all the way to the wall. This approach main disadvantage is being more computationally expensive compared to wall function approach.

RANS turbulence models can generally have two forms, which are high-Re and low-Re models, depending on flow domain and boundary treatment. Generally, high Re models incorporate walls functions, while, low-Re models resolve the boundary layer with a very fine mesh near the wall.

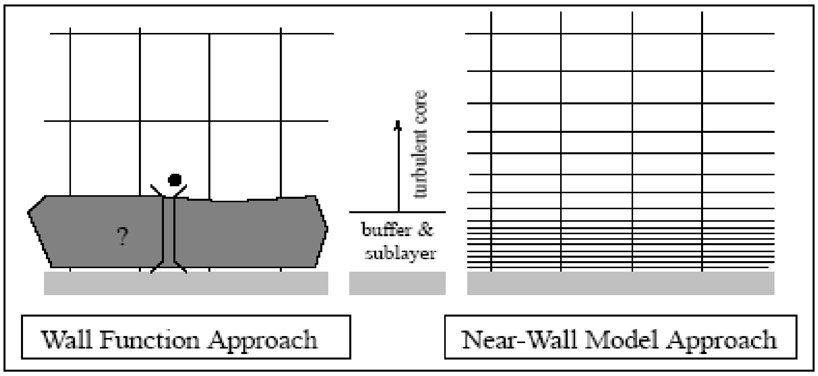

Figure 2.2: The main approaches for the treatment of near-wall region in CFD codes [72].

2.1.4 Procedure and Steps of CFD Modeling

The general procedure of CFD modeling consists of the following steps:

a) Proper selection of the mathematical model

Tackling a physical problem by CFD starts with the proper approximation of flow characteristics, i.e. viscous or inviscid, laminar or turbulent, incompressible or compressible, single-phase or multi-phase. Based on flow characteristics and boundary conditions, a mathematical model, i.e. the governing PDEs, can be formulated to ensemble the whole domain.

b) Preprocessing (Grid Generation)

Pre-processing starts with drawing of spatial domain by CAD tools, e.g. GAMBIT. Computational grid or mesh is obtained by suitably dividing the geometrical domain into 3D cells or 2D elements. These discrete cells/elements form the calculation nodes, where different dependent variables are locally solved. There are three main gridding (meshing) strategies, namely, structured, unstructured and hybrid, which are used to generate the grid. Structured grids majorly consist of quadrilateral elements or hexahedral cells. On the other hand, unstructured grids employ triangles or tetrahedral cells. While, hybrid grids consist of mixed elements/cells from previous geometrical shapes [71].

c) Solution Methods

There are several numerical methods to discretize the continuous PDEs like Finite Element Method (FEM), Finite Difference Method (FDM) and Finite Volume Method (FVM). The FVM, which is employed in the commercial code of ANSYS-FLUENT, encompasses the integration of governing PDEs over each non-overlapping control volume, i.e. every cell/element in the mesh. The FVM formulation ensures the integral conservation of mass, momentum and energy over discrete volumes, and thus, accommodates the entire calculation domain. The FVM discretization transforms the continuous PDEs into simple algebraic equations which can be solved with relative ease. Moreover, evaluation of required integrals requires an expression for the variation of dependent variables between grid points which are termed piece-wise profiles/schemes like piece-wise linear or polynomial [51].

d) Solution Monitoring

Solving discretized equations by CFD codes involves successive iteration techniques, e.g. Gauss-Seidel iterative method [51], to get a converged solution for each dependent-variable field. Fields' residuals[12] are used to measure computational errors between successive iterations and indicate convergence. To obtain an accurate, stable and converged solution, the residuals of every dependent-variable field should reach prescribed threshold or convergence criteria.

e) Post-Processing

Post-processing of CFD simulations includes the collection and the analysis of data of a converged solution. In addition, validation of results to ensure realistic agreement with theory/experiments is another critical part of post processing. A numerically converged solution does not mean that the solution is acceptable physically. Therefore, the actual measurement, e.g. velocity or temperature at a specific point, is used to identify a “physically realistic” CFD result.

[12] Residual: The relative difference of fields' values, e.g. velocity, between two successive iterations to compute the error of CFD approximations.

2.1.5 Multi-Phase Models

The two-phase gas-liquid flow is generally complex because it incorporates a deformable interface as well as gas compressibility. Gas-Liquid flow in a tubeis classified into different regimes based on the interfacial distribution and volumetric fractions of the two phases. Argon-molten steel flow in the **S**ubmerged **E**ntry **N**ozzle (**SEN**) falls into the bubbly flow regime criterion because argon has a low volume fraction inside SEN. In such bubbly flow, argon bubbles are considered discrete and dispersed secondary-phase structures in the primary continuous phase of molten steel.

In CFD packages like ANSYS-FLUENT, several multi-phase models exist to solve such two-phase flows, namely, the Eulerian Model, the Volume Of Fluid (VOF) model and the Discrete Phase Model (DPM). Each of these models has a distinctive formulation and assumptions to generate the required simulation. The VOF model is used mainly for stratified and free surface multi-phase flows. On the other hand, bubbly flows can be modeled effectively by Euler model and DPM [72].

2.2 Modeling of Continuous Casting

Understanding and controlling the flow behavior inside SEN/mold configuration are of huge importance since several quality defects are linked to it. For instance, optimization of SEN design through parametric studies can reduce meniscus fluctuations, and consequently, lead to less quality defects. Since parametric studies are difficult, risky and expensive to carry out on an operating caster by plant trials, models, like CFD models and physical water models, are used extensively for this purpose. Generally, these models fall into two main categories which are single-phase models and multi-phase models.

2.2.1 Single-Phase Models

Initially, single-phase molten steel flow in continuous casters was investigated by water models but later CFD models were utilized. Najjar et al. [66, 67] published thorough parametric studies for bifurcated SEN optimization by CFD simulations. Also, Thomas et al. [55] compared the results of different CFD models with water model results for various SEN and mold configurations. Heaslip et al. [36] conducted a study to compare different C.C. flow control systems, namely, stopper-rod and slide-gate systems. Further, Iguchi et al. [62] used a water model with a floating oil layer to study slag emulsification phenomena inside continuous casters.

The typical flow double-roll pattern inside the slab caster mold, equipped with bifurcated SEN, is shown in Figure 2.3.

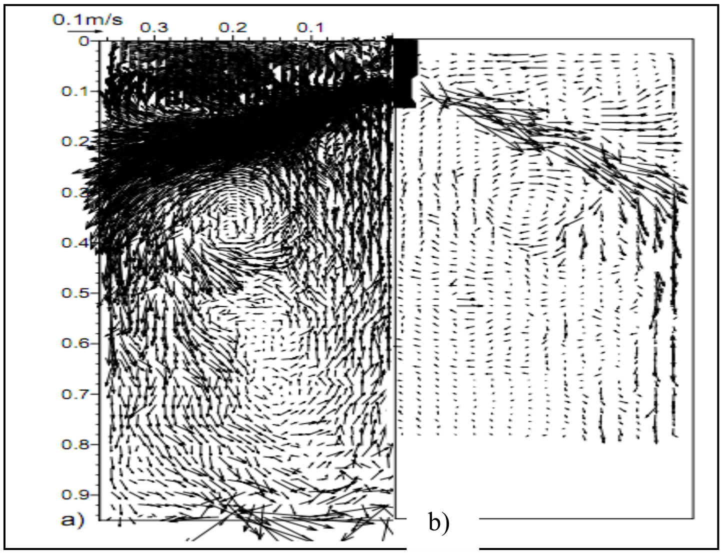

Figure 2.3: Instantaneous velocity vector plot, (a) Large Eddies Simulation (b) PIV measurement, showing the typical C.C. double roll flow pattern in the mold [55].

Moreover, both geometrical parameters, shown in Figure 2.4, as well as operational factors, like submergence depth and casting speed, have strong effects on the flow pattern and jet characteristics as highlighted in Table 2.1.

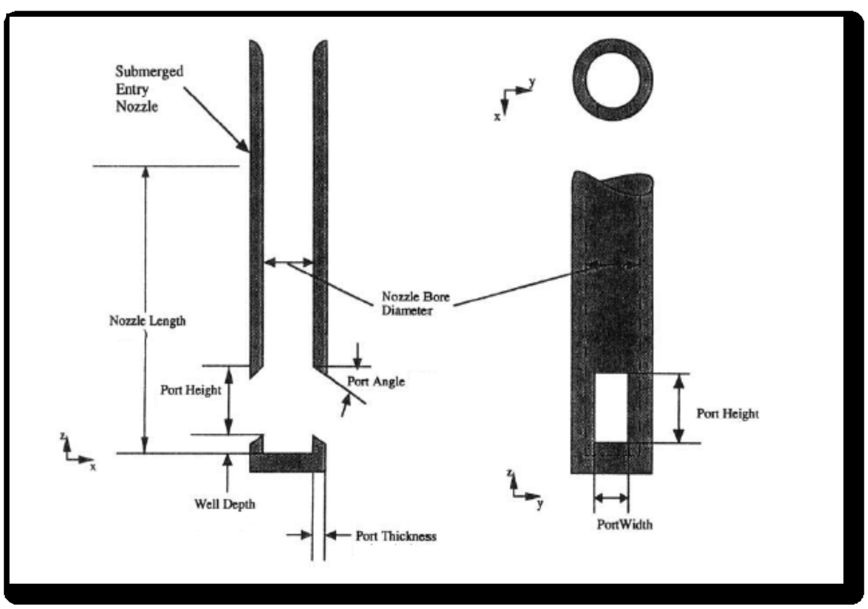

Figure 2.4: Schematic of a bifurcated SEN with the typical geometrical nomenclature.

Table 2.1: Effects of different factors on flow obtained by single-phase simulations [66].

SEN Geometry/Operational factor	Influence on flow
Port angle	The turbulence intensity of jet increases with increasing port angle.
Port width	Narrow ports generally increase the effect of port angle and shape.
Port shape	Round ports increase the swirling component of the jet and increase the turbulence compared to square ports.
Casting speed	Jet speed & turbulence levels increase with casting speed due to the increase in throughput out of SEN ports.
Slab width	Very wide molds/slabs can change the flow pattern from double roll to single roll.
Submergence depth	Shallow submergence depth can change the flow pattern from double roll to single roll as well as increase the meniscus velocity.

2.2.2 Two-Phase Models

After the implementation of gas injection in metallurgical processes, substantial research was conducted to model the two-phase flow by both gas-water models and CFD multi-phase models. Moreover, physical gas-liquid metal, e.g. mercury or molten iron, models were used to study the gas injection in a quiescent molten steel system such as ladle stirring. However in casters, argon is injected into a turbulent stream which yields a different two-phase flow phenomenon compared to the quiescent molten steel case. Better understanding of argon-liquid steel flow helps in the quality improvement and the proper control of operational parameters such as argon flow rate. Unfortunately, the broadly used gas-water models do not have the proper similitude to model the heat transfer and the complexity of the two-phase flow. Dissimilarity can be attributed to the difference of physical properties, like interfacial tension and viscosity, of molten steel and water. While, multi-phase CFD models may provide added insight into flow dynamics overcoming inaccuracies of gas-water models.

Bai and Thomas [56-57] established a 3-D finite difference Eulerian multi-phase model that incorporate k-ε turbulent model. They investigated the effects of argon injection, slide gate position, casting speed, nozzle bore diameter and tundish bath depth on flow and pressure inside SEN. Their results indicate that argon injection reduces possible air aspiration through slide gate joints by increasing the minimum pressure across the slide gate. Also, they recommended reducing argon flow rate at low and very high casting speeds. Sussman et al. [58] incorporated the (k-ε) turbulence model into a 3-D Eulerian multi-phase model to simulate the two-phase flow and to study argon effects on flow pattern inside the mold. Furthermore, they studied the effects of gas injection on temperature distribution, superheat dissipation and grade intermixing during continuous casting and compared their predicted results with experimental measurements.

Dennisov et al. [59] studied the behavior of argon inside the continuous caster mold using both the air-water model and the 3-D finite difference simulations. It was concluded that argon may reduce clogging but excessive flow rate might cause fluctuations at meniscus which might lead to surface defects like deep oscillation marks and slag emulsification. Also, they have indicated that argon bubbles support inclusion removal by attachment to bubbles and agglomeration.

Pfeiler et al. [60] used Eulerian-Lagrangian approach to model the multi-phase flow inside a trifurcated nozzle in a thin slab mold. Two methods of interaction between liquid steel and dispersed phases, namely, one way coupling and bi-directional coupling, were examined. They recommend incorporating bi-directional interaction for multi-phase studies to obtain a reliable prediction.

YU et al. [61] studied argon injection influence on level fluctuations at the interfacial layer or liquid flux-steel meniscus interface. They used the Volume of Fluid model (VOF) to simulate this phenomenon in a thin slab caster. They investigated the influence of nozzle submergence depth and casting speed on the two-phase flow. They noted a critical argon flow rate value to have a stable interfacial layer and reduce level fluctuations, while fixing other casters' parameters.

2.2.3 Heat Transfer Models

In continuous casters, the strand's casting speed is controlled by different factors like alloy composition, as-cast geometry and superheat. Molten steel superheat limits the casting speed due to its implications on liquid pool and shell thickness at mold's outlet. Excess superheat increases both the liquid pool's depth within the strand and the shell surface temperature. This prolongs complete solidification and increases the cooling requirements. Also, at the maximum heat-flux region, where the molten jet impinges against the narrow face, excessive superheat might encourage shell thinning and may lead to shell breakout below the mold. Moreover, shell thinning can lead to strand bulging, by internal ferro-static forces, in large slabs if roll containment is insufficient. Last but not least, higher casting speeds often cause surface cracks, due to the higher thermal stresses.

Molten steel superheat also influences the internal microstructure and related macrosegregation defect, where, the formation and remelting of crystal nuclei and subsequent growth is controlled by the degree of superheat. High superheat enhances the undesirable formation of columnar grains. These columnar grains aggravate the macrosegregation defect compared to the equiaxed grains.

At the liquid flux/molten steel interface, liquid steel should maintain sufficient superheat and velocity to avoid meniscus and flux freezing as well as the tendency of subsurface hook formation. So, inadequate superheat worsens the surface defects, while, excessive superheat leads to low casting speeds or reduced productivity of the caster.

Heat extraction in a continuous caster involves a complex interplay of several heat-transfer mechanisms like the convection of superheat in the liquid pool due to the incoming metal momentum as well as the conduction through steel shell and mold walls. So, superheat optimization and proper extraction in the mold's upper region is one of the main objectives to optimize caster's performance

There are few studies or validated models of coupled turbulent flow with heat transfer in the literature. Hasan and Seyedein [90] performed 3-D finite difference simulations using a low-Re number (k-ε) model, which included solidification phenomenon, to study the effects of different heat extraction rates on steel solidification. Thomas et al. [91], using ANSYS-FLUENT code, compared different RANS coupled heat-transfer models with the temperature measurement in a thin slab caster and found reasonable agreement. Thus, CFD coupled with heat transfer models can be considered credible.

Although heat transfer simulations do not incorporate solidification and heat extraction by mold walls, temperature distribution at the upper mold region can be estimated roughly by CFD simulations as asserted by Thomas et al. [58]. This can be achieved by assuming steel liquidus temperature, as a boundary condition, at mold walls where the shell is very thin. So, this assumption will be integrated in heat transfer simulations to study the effects of argon bubbles on the temperature distribution.

2.2.4 Measurement of Actual Velocities in Steel Casters

Velocity measurement of liquid metals and slags is a challenging task due to the opacity and corrosiveness of these fluids. Even though some velocimeters are used in low temperature liquid metals and hot transparent salts, almost all of the available techniques fail in measuring high-temperate (>1500 °C) liquid steel velocity in C.C. mold. Based on a review by Argypoloulos [86], photographic methods, hot wires and films anemometers, electromagnetic (potential difference) probes, tracer studies, reaction probes, dissolution measurement, sphere melting method and fiber-optic sensors and Karman-vortex probe face limitations in measuring liquid steel velocity in industrial settings. These methods are hindered by steel high temperature range, opacity of slag/liquid steel and calibration difficulties. Also, many methods are costly, inaccurate, or only provide average velocities over large distances. Hence, these methods are impractical to measure molten steel velocity in an industrial scale. Nonetheless, velocity at the meniscus can be estimated roughly by some methods like nail-board method [88].

Meniscus velocity is a key factor that affects the final quality because high surface velocities create shear instability at slag-liquid steel interface with a very high possibility of slag entrainment. On the other hand, too low surface velocities may cause hook formation and entrapment of inclusion/slag particles due to the insufficient heat transfer near the narrow face and meniscus regions. Therefore, it is deemed important to measure and control meniscus velocities in the mold during C.C. process.

Typically, a double-roll flow pattern with symmetric flow from bifurcated SEN in slab casters is highly desirable to avoid these problems. Meniscus velocity profiles for different casting speeds are simulated by computational codes, namely, k-ε and LES, as well as water model's PIV results and are shown in Figure 2.5. The centerline velocity increases gradually from the narrow face till reaching a peak in about a quarter-distance along the wide-face then decreases when approaching SEN. Moreover, the mold velocities generally exhibit a transient behavior as indicated by the horizontal velocity history at a point between SEN and narrow face, see Figure 2.6. This transient behavior is due to the turbulent nature of the flow, i.e. fluctuation components of velocity [55].

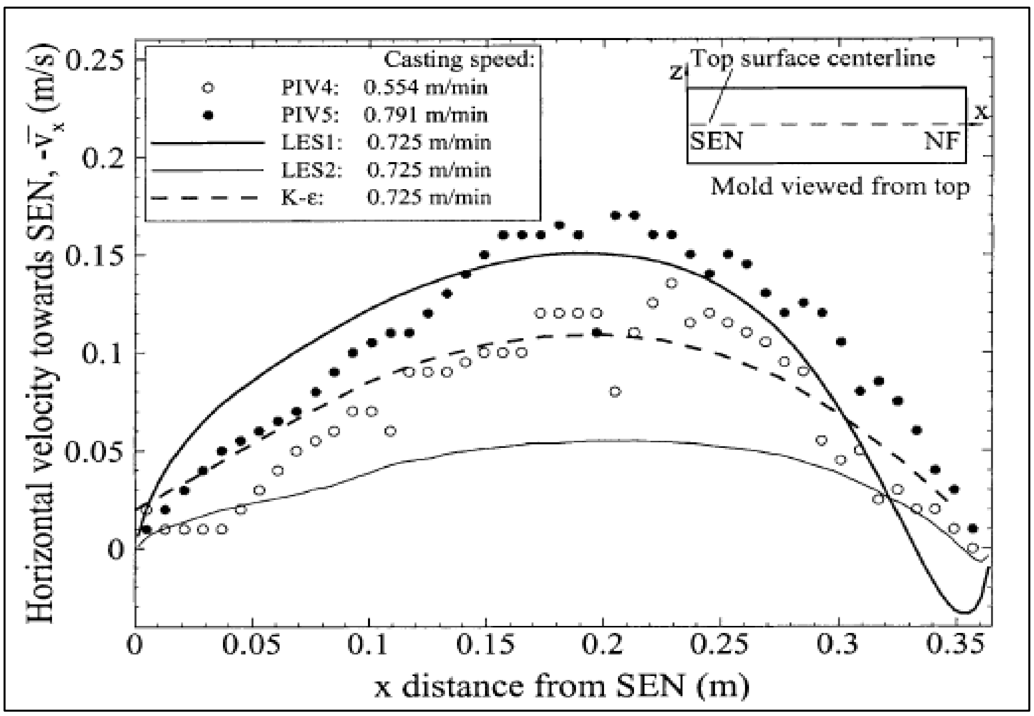

Figure 2.5: Time-averaged speed profile along surface centerline, comparing PIV, K-epsilon and LES. (Mold 228 X 1800)

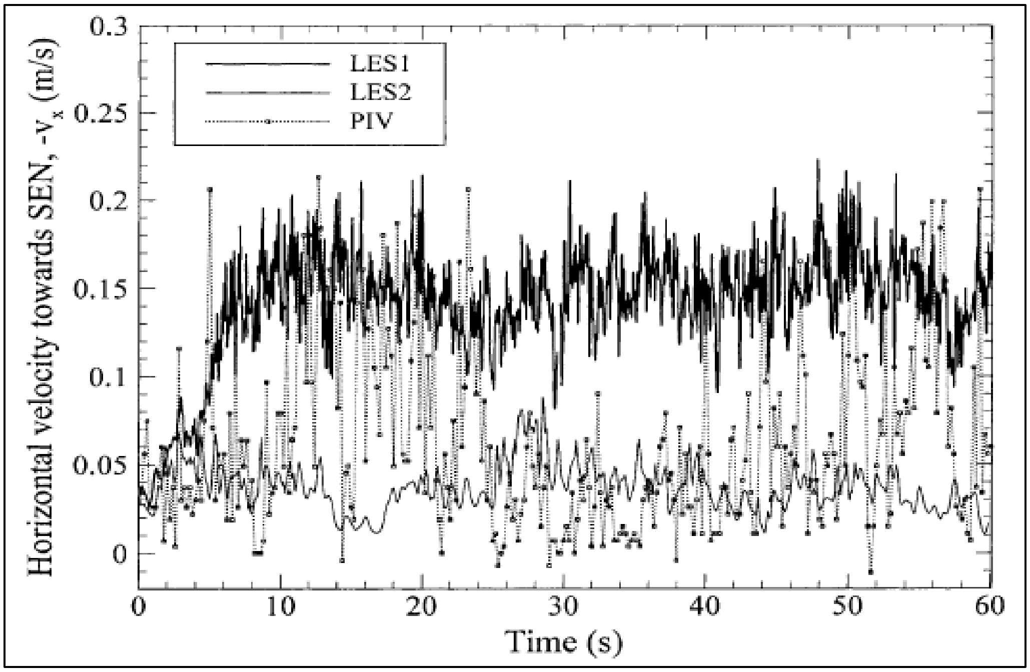

Figure 2.6: Velocity history from different methods at a point in mid-way between SEN and narrow face at about 2cm below surface.

Regarding the actual surface velocity values in slab casters, nail insertion (dipping) method can provide a rough estimation of velocity and flow direction in a slab mold. The general steps of this method are illustrated in Figure 2.7. Such a method is normally used simultaneously with the measurement of powder/slag layer thickness as seen in

Figure 2.8. The basic idea of the nail-dipping method is to insert the nail(s) momentarily into molten steel for about 3~5 seconds. Later, a solidified knob or lump forms due to the impingement and solidification of liquid steel and slag around the nail. The height difference of the solidified knob forms because flow kinematic energy is converted to potential energy at the stagnation point. Since the pressure is lower at the wake region, steel level drops on the opposite side of the nail lump. The shape of the lump and the height difference indicate the direction and the magnitude of surface velocity, respectively [87].

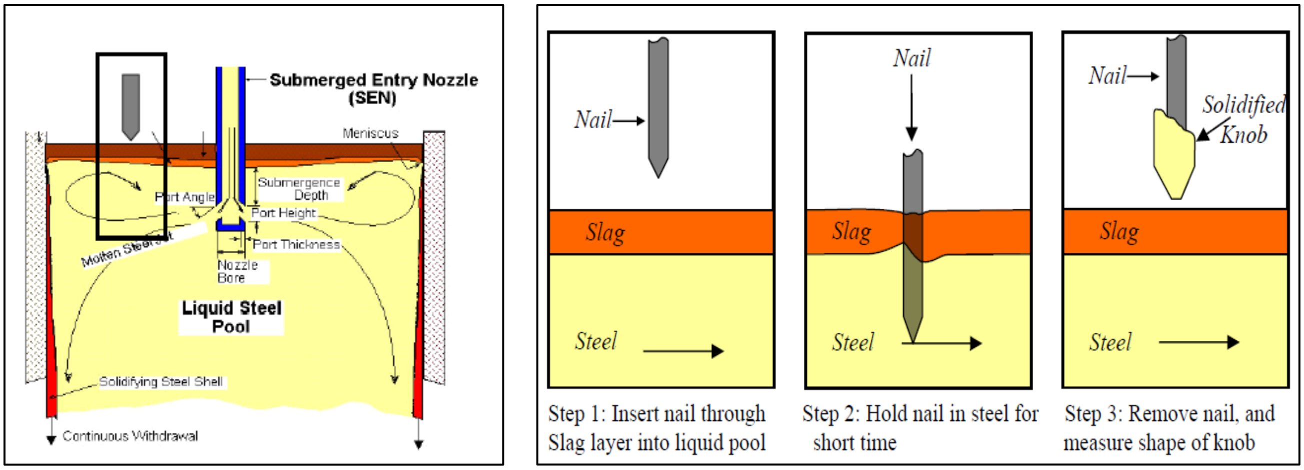

Figure 2.7: The general procedure of Nail-board insertion method [88].

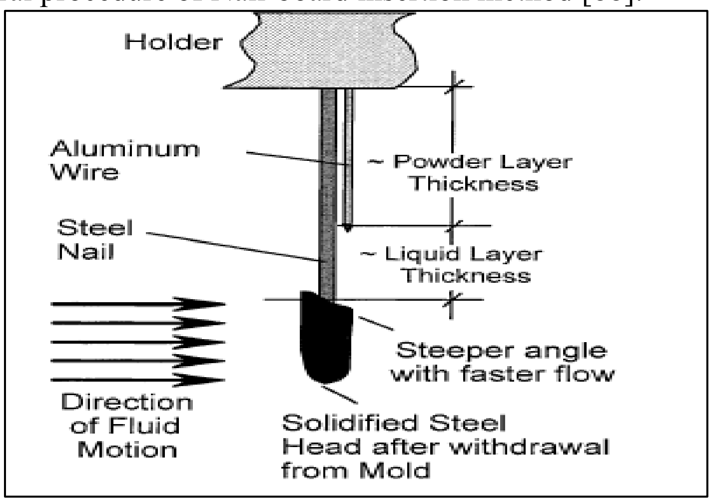

Figure 2.8: Schematic of the measurement of slag thickness and surface velocity using nail insertion. [55]

Thomas et al. [88] compared the meniscus velocity measurements of nail insertion and Sub-meniscus Velocity Control (SVC)[13] methods for different slab casting conditions as seen in Table 2.2. The **SVC** rod was inserted at a quarter distance of wide face, while, the 6-mm diameter nail was inserted at about 50 mm closer to narrow face compared to SVC. The results of the experimental study using these methods are shown in Figure 2.9. The geometrical parameters that were used in their study are not far-off the geometrical parameters of the present simulations. Thus, the experimental measurements can be used creditably as a validation tool, at least for the qualitative comparison with the present CFD simulations. The comparison between simulation results and experimental results is done in Section 4.2.2.

[13] SVC method basic principle is to convert the deflection angles or measured torques of an immersed rod into surface velocities of steel.

Table 2.2: The main parameters of the slab continuous caster employed in the experimental study of SVC and Nail comparison study.

Measuring Method	Mold Thickness (mm)	Mold Width (mm)	SEN Submergence depth (mm)	Gas Injection Rate (SLPM)
Nail	225	983	185	6
SVC+Nail		1248	177	

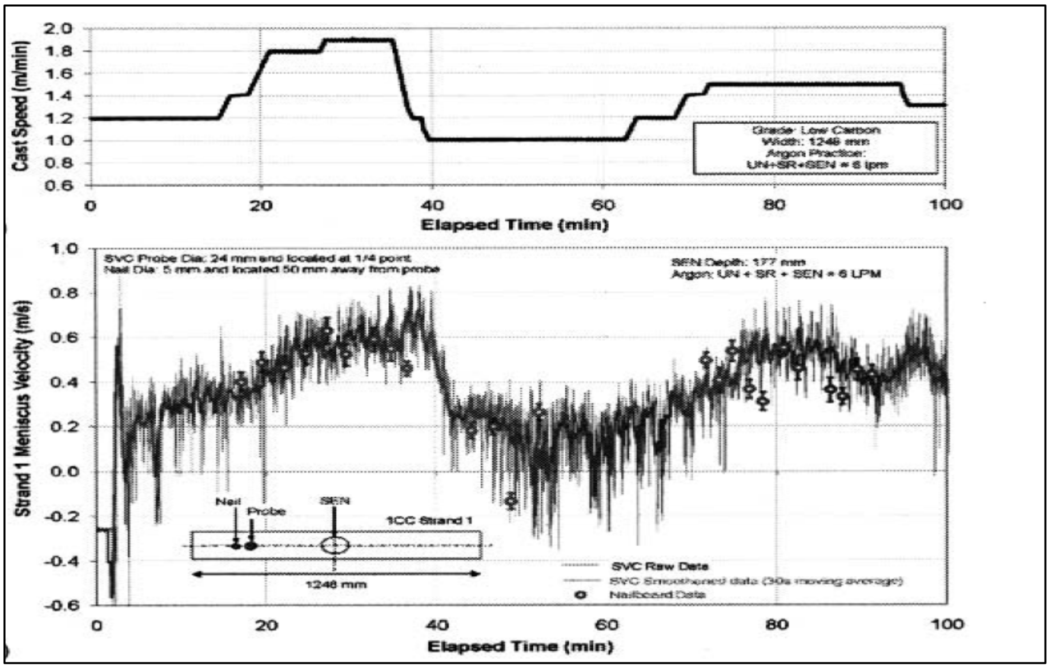

a) Casting speed change profile and the corresponding meniscus velocity.

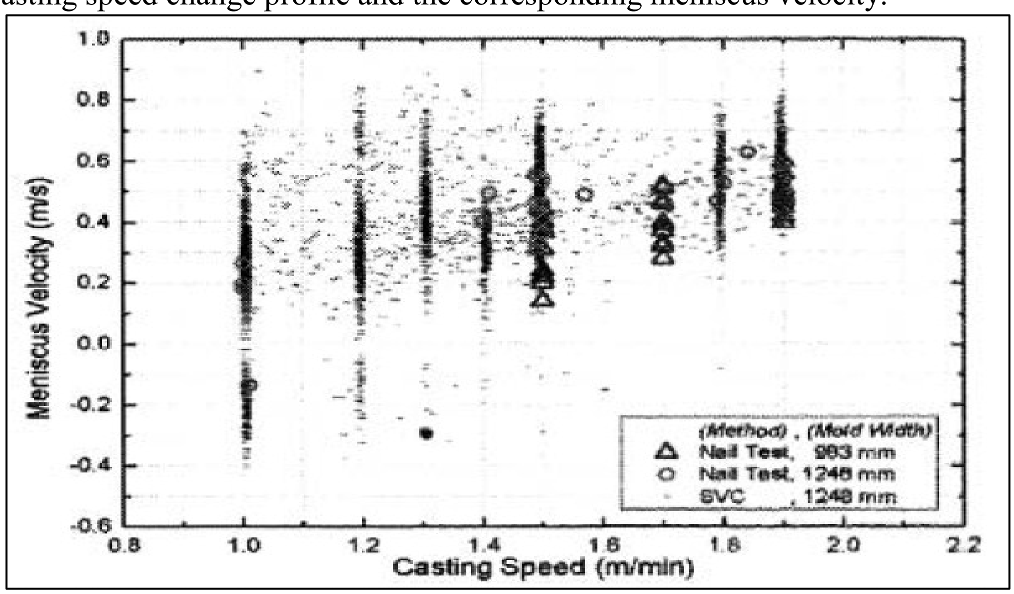

b) Casting speed effect on meniscus velocity for both Nail test and SVC.

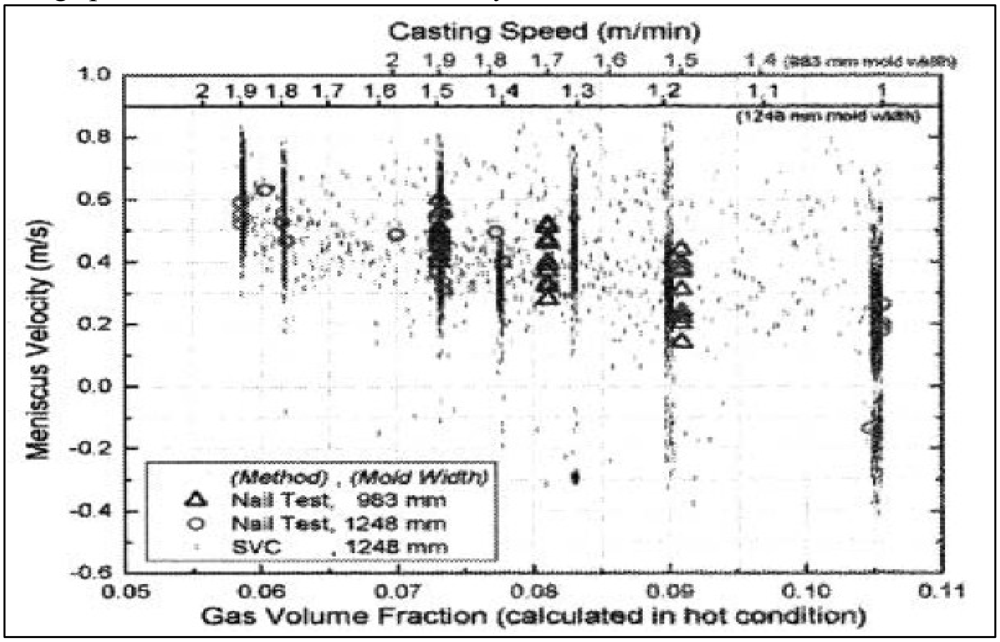

c) Gas volume fraction (hot condition) effect on meniscus velocity.

Figure 2.9: Experimental study results of actual caster using SVC and Nail dipping methods[88].

Chapter 3: Modelling of Argon Injection by Discrete Phase Model

3.1 Argon Injection through Stopper-rod

Argon injection benefits include the enhancement of agglomeration and flotation of inclusions as well as the reduction of SEN clogging. However, excessive injection flow rates can lead to deteriorated quality. The simulations of this present research represent argon injection through a porous plug. In addition, proper estimation of the bubble size range in molten steel is critical for accurate simulations of the two-phase flow phenomena and further control of injection flow rates.

3.1.1 Bubble Formation Mechanism

Understanding the principles of bubble formation and subsequent size are important since gas injection plays a key role in different industries like metallurgical processes development. Based on a review paper by Kulkarni and Joshi [74], most studies in the literature are related to bubble formation from a single orifice that is submerged in a stagnant liquid pool. Moreover, usage of image visualization methods like stroboscopes[14] and high-speed camera for transparent liquids and X-ray for opaque liquids are common in the experimental setup.

Under the assumption of constant bubble volume, frequency of the bubble formation at an orifice can be measured by pressure pulse and/or acoustic devices. The approximate bubble volume can be later estimated by equation (3.1).

$$Volume_{Bubble}\,(m^3) = \frac{Gas\ flow\ rate(m^3/sec)}{Frequency\ of\ formation(\frac{bubble}{\mathrm{sec}})} \tag{3.1}$$

Analytical models of spherical bubbles are formulated based on the force balance over the forming spherical bubble. The force balance over a bubble involves buoyancy, surface tension, liquid inertial forces, viscous drag and gas momentum. Furthermore, the most reliable analytical models, that yield good predictions compared to experimental results, are formulated by the two-stage model, namely, expansion (growth) stage and detachment stage, such as Kuloor and Kumar [73] two-stage model. However, bubble shapes observed through experimental tools indicate that both spherical and non-spherical bubbles are possible based on fluids, gas and liquid, properties and flow conditions. Therefore, computational models of non-spherical bubbles

[14] An instrument used to make a cyclically moving object appear to be slow-moving, or stationary. The principle is used for the study of rotating, reciprocating, oscillating or vibrating objects.

are devised through the local balance of pressure and force at the gas/liquid interface, where the bubble surface is divided into 2-D axisymmetric elements. In these models, equations of motion and continuity for both vertical and radial directions are solved for each element to find the velocity and position of the interface, i.e. movable pressure boundary. [80].

Unfortunately, the results of bubble formation/detachment models are not concordant and these models basically depend on the model assumptions and the system under investigation. Also, coalescence and breakup models are not yet established to provide accurate results to be integrated into CFD formulations or codes.

In steel industry, gas injection into molten steel is mainly used in ladle furnaces, BOF, vacuum degasser, ladle shrouding tube and tundish SEN. The majority of studies are focused on gas-stirred vessels from a vertically-directed orifice into a quiescent molten steel bath. Guthrie and coworkers [81] measured bubble formation frequency in molten iron path using known gas flow rates to infer bubble volume by equation (3.1). The equivalent diameters are predicted to be larger than 10 mm, under the assumption of spherical shape. This was supported by Iguchi et al. [82] study which incorporated X-ray fluoroscopy visualization method.

However, in continuous casters, argon is injected into a highly turbulent traverse flow with a shearing force that influence bubble formation frequency, coalescence and subsequent size. Thus, bubble sizes are presumed smaller due to the severe influence of turbulence intensity compared to quiescent liquid steel. Moreover, the bubble size distributions as well as the bubble formation frequency are critical for accurate modeling of the two-phase flow.

In a recent study, the distribution of air bubbles in the air-water model was used to predict the expected distribution of argon bubbles in real casters [85]. However, the actual distribution of argon bubbles of this complex two-phase flow cannot be reflected in air-water models because [83]:

1) Surface tension coefficient[15] of liquid steel-argon is 16 times higher than air-water.
2) Steel viscosity is 5 times higher than water.
3) Steel does not wet the refractory surface which influences the bubble formation frequency[16].

[15] $\sigma_{\text{steel -argon}}$ =1192 (dynes/cm) = 1.192 (N/m) (temperature and composition-dependent)
$\sigma_{\text{Water-air}}$ =73 (dynes/cm) = 0.073 (N/m)

4) The high argon temperature speeds up bubbles' detachment due to the higher momentum and the lower density in comparison to air-water models.
5) Turbulence in SEN and mold region encourages the bubble coalescence or breakup phenomena.

Therefore, proper evaluation of the bubble distribution, in relation to injection flow rate, in real casters is a key factor in determining the overall characteristics of the two-phase flow. Unfortunately, exact evaluation is difficult due to the process high temperatures and the turbulence effects. However, estimation of bubble sizes in a turbulent flow can be obtained through expression (3.2) which gives the approximate bubble diameter in a turbulent flow based on the critical weber number, turbulence intensity and fluids properties, see Section 3.1.3.

3.1.2 Stopper-rod Specifications

Stopper-rod, a refractory rod with high resistance to thermal shock and erosion, is used to control molten metal flow rate in casters. It can be used to introduce argon gas into molten metal stream through an integrated porous plug. Stopper rod body and porous plug are iso-statically co-pressed of similar materials (see Table 3.1) but with different grain sizes to yield a substantially different mean pore sizes, i.e. different gas permeability. So, continuous channels of small pores form within the porous plug. These micron-sized channels permit gas flow and prevent molten steel infiltration back into the pores. Porous plug usually has a mean pore size of about 10 μm, while, the body portion's mean pore size is 0.25 μm. Therefore, the porous plug produces very fine bubbles and provides a uniform gas flow by maintaining a sufficient gas pressure within the rod [7, 79].

Table 3.1: The typical composition of an industrial stopper-rod.

Component or Aspect	Body	Porous Plug nose
Al_2O_3	53%	61%
C (Graphite)	31%	22%
SiO_2	13%	6%
ZrO_2	1%	6%
other	2%	5%
Mean Pore size (microns)	0.25	10

[16] Static contact angle in liquid steel-argon-ceramic system is 150°. On the other hand, the contact angle is about 50° in air-water-plastic system.

Porosity (%)	18	19
Permeability (liter/min)	1	48

3.1.3 Predicted Bubble Size

Even though fine bubbles are produced by the porous plug, these bubbles are expected to coalesce due to the turbulent eddies near injection points and form large bubbles. Also, relatively large bubbles might form with high gas flow rates and/or low casting speeds as well as in the recirculation areas of a bifurcated nozzle.

These large bubbles are expected to break-up due to the high local turbulence levels at SEN outlet. Sevik and Park [77] correlated the bubble maximum diameter to a critical Weber number (We_{Crit}) and turbulent stirring intensity in a turbulent two-phase jet. Their experimental data yielded the following expression to calculate the maximum bubble diameter:

$$d_{\text{bubble max}} \approx We_{crit}^{0.6} * \left(\frac{\sigma * 10^3}{\rho * 10^{-3}}\right)^{0.6} * (\varepsilon * 10)^{-0.4} * 10^{-2} \quad (3.2)$$

Where; $\mathbf{We_{Crit}} \approx 0.59\text{-}1.0$

The Stirring power (ε) of various metallurgical systems and the predicted bubble sizes are shown in Figure 3.1 [78]. Generally, high stirring power favors the formation of small bubbles due to high influence of breakup phenomenon. For a highly turbulent flow system such as SEN outlet flow into the mold ($\varepsilon > 1000$ W/tonne), the predicted maximum bubble diameter is about 5 mm.

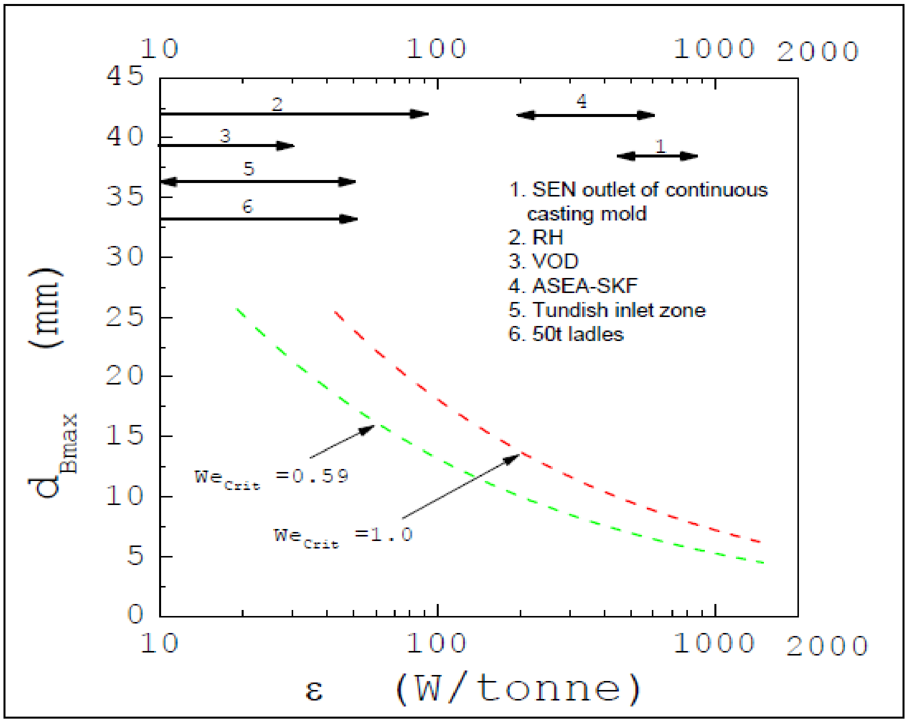

Figure 3.1: $d_{bubble\ max}$ as a function of stirring power for different metallurgical systems.

3.2 Discrete Phase Model (DPM) Theory

Secondary phase particles or bubbles in continuous casting process can be studied using Lagrangian trajectory calculations, e.g. Discrete Phase Model in ANSYS-FLUENT. Bubbles' position and velocity are obtained through integration of trajectory equation (3.3) using instantaneous velocity components of continuous phase at each cell. Whereas, a stochastic model, namely, Discrete Random Walk, accounts for bubbles dispersion inside the turbulent continuous phase. Therefore, DPM can be used to track argon bubbles location and velocity within the calculation domain [72].

Generally, the bubble momentum equation is integrated with respect to time along the particle path-line. Thus, the rate of change of momentum represents the force balance over the bubble during its motion. Typical force balance over a discrete bubble in a viscous fluid flow is shown in Figure 3.2.

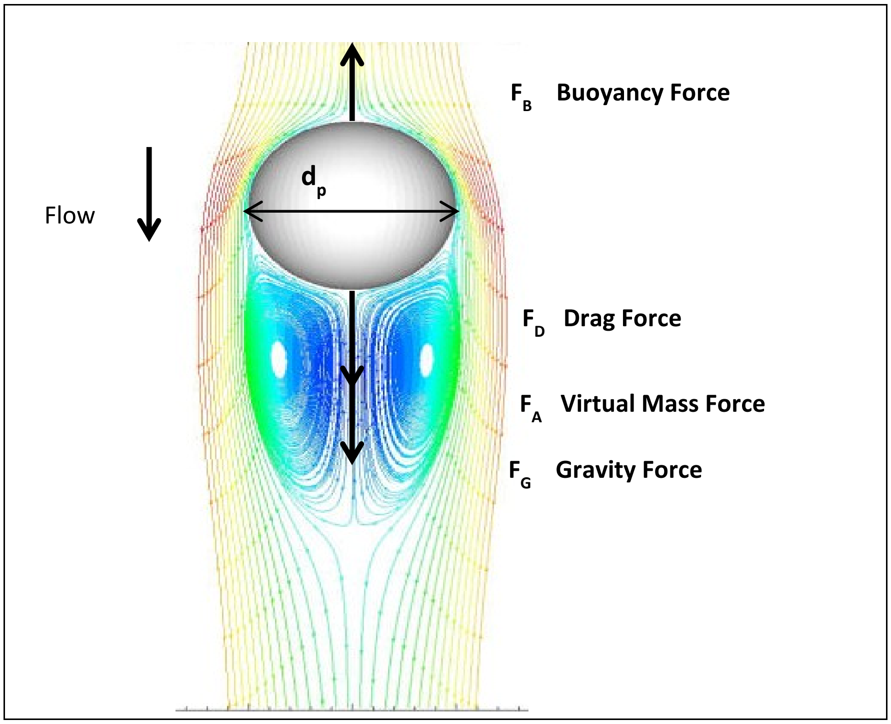

Figure 3.2: Schematic of forces acting on a bubble in a viscous fluid flow.

The governing equation for bubble trajectory is as follows:

$$\frac{du_p}{dt} = \frac{18\,\mu C_D Re}{24\,\rho_p d_p^2} u_{rel} + \frac{g(\rho_p - \rho)}{\rho_p} + f_a \tag{3.3}$$

Where;

$Re = \frac{\rho d_p |u_{rel}|}{\mu}$

$u_{rel} = u - u_p$

$f_a = \frac{1}{2}\frac{\rho}{\rho_p}\frac{d}{dt}(u - u_p)$

The right-hand side terms in equation (3.3) represent the forces on each bubble per unit mass, whereas, the left-hand side represents the acceleration of the bubble. These forces are the drag force, the buoyancy force due to gravity and density difference, and the virtual mass force (f_a). The bubble's position can be calculated incrementally by integrating its local velocity with respect to time [72]. The derivation of equation (3.3) is described in details in Appendix A.

3.2.1 Drag Coefficient Correlation

Drag coefficient[17] (C_d) quantifies the resistance of an object or bubble in a fluid and is a function of Reynolds number. Also, for the caluclations of C_d, coefficients a_i (i=1-3) are empirically obtained for different Reynolds number ranges. C_d varies with speed, flow direction, object position, object size, fluid density and fluid viscosity. For DPM simulations, ANSYS-FLUENT recommends Morsi and Alexander model [76] for spherical bubbles. The C_D general model equation (3.4) shows that drag coefficient is adjusted over a wide range of Re numbers as illustrated in Table 3.2. Thus, C_d is calculated, in the simulation domain, based on the local Re number within each control volume cell.

$$C_d = a_1 + \frac{a_2}{Re} + \frac{a_3}{Re^2} \tag{3.4}$$

Table 3.2: Correlations of drag coefficient for different Re number ranges.

Drag coefficient correlation	Re number range
$C_d = 24.0/\boldsymbol{Re}$	$\boldsymbol{Re} < 0.1$
$C_d = 22.73/\boldsymbol{Re} + 0.0903/\boldsymbol{Re}^2 + 3.69$	$0.1 < \boldsymbol{Re} < 1.0$
$C_d = 29.1667/\boldsymbol{Re} - 3.8889/\boldsymbol{Re}^2 + 1.222$	$1.0 < \boldsymbol{Re} < 10.0$
$C_d = 46.5/\boldsymbol{Re} - 116.67/\boldsymbol{Re}^2 + 0.6167$	$10.0 < \boldsymbol{Re} < 100.0$
$C_d = 98.33/\boldsymbol{Re} - 2778/\boldsymbol{Re}^2 + 0.3644$	$100.0 < \boldsymbol{Re} < 1000.0$
$C_d = 148.62/\boldsymbol{Re} - 4.75\times10^4/\boldsymbol{Re}^2 + 0.357$	$1000.0 < \boldsymbol{Re} < 5000.0$
$C_d = -490.546/\boldsymbol{Re} + 57.87\times10^4/\boldsymbol{Re}^2 + 0.46$	$5000.0 < \boldsymbol{Re} < 10000.0$
$C_d = -1662.5/\boldsymbol{Re} + 5.4167\times10^6/\boldsymbol{Re}^2 + 0.5191$	$10000.0 < \boldsymbol{Re} < 50000.0$

3.2.2 Continusous Phase Turbulence Impact on Dispresed Phase

The instantaneous velocity, expression (3.5), of the turbulent continuous phase is divided into two components which are the mean velocity component ($\bar{u}$) and the fluctuating component ($\grave{u}$). These quantities are calculated from the expressions (3.6) and (3.7).

$$u = \bar{u} + \grave{u} \tag{3.5}$$

[17] a dimensionless quantity in drag force and momentum exchange calculations.

$$\grave{u} \equiv \sqrt{\frac{1}{3}\left(\grave{u}_x^2 + \grave{u}_y^2 + \grave{u}_z^2\right)} = \sqrt{\left(\frac{2}{3}k\right)} \tag{3.6}$$

Where the turbulent kinetic energy $k = \frac{1}{2}*(\grave{u}_x^2 + \grave{u}_y^2 + \grave{u}_z^2)$

$$\bar{u} = \sqrt{u_x{}^2 + u_y{}^2 + u_z{}^2} \tag{3.7}$$

The impact of velocity fluctuations, which form due to the generation and movement of eddies, on bubble trajectory is treated using Discrete Random Walk (DRW), also called eddy lifetime model. DRW simulate the interaction of a particle with a series of discrete stylized turbulent eddies. Each eddy is characterized by the three dimensional velocity fluctuations as well as the characteristic lifetime of an eddy. The fluctuating velocity components, which prevail during the eddy lifetime, are calculated by the expression (3.8), where, the magnitude of the fluctuating component varies with the local turbulent kinetic energy at each cell [72].

$$\grave{u} = \varsigma\sqrt{\frac{2k}{3}} \qquad \grave{v} = \varsigma\sqrt{\frac{2k}{3}} \qquad \grave{\omega} = \varsigma\sqrt{\frac{2k}{3}} \tag{3.8}$$

Where; ς is a random number obtained through Gaussian Probability Distribution (GPD).

The bubble is assumed to interact with the local eddy over the smaller of the eddy rotation time (τe) or eddy crossing time (t_{cross}). When this time limit is reached, a new value of the instantaneous velocity is obtained by applying a new value of ς in expressions (3.8). Eddy rotation time (**$\boldsymbol{\tau_e}$**), expression (3.9), describes the time that a bubble spend in the turbulent motion of the considered eddy. Further, the eddy rotation time **($\boldsymbol{\tau_e}$)** is proportional to Lagrangian integral time (T_L), which can be approximated from expression (3.10). The eddy rotation time is approximated in k-ω turbulence model as $\boldsymbol{\tau_e} \approx (0.3\,\frac{1}{\omega})$, whereas, the particle eddy crossing time (t_{cross}) is calculated by equation (3.11).

$$\boldsymbol{\tau_e} = 2T_L \tag{3.9}$$

$$T_L = 0.15 * \frac{1}{\omega} \tag{3.10}$$

$$t_{cross} = -\boldsymbol{\tau}\, ln\left[1 - \left(\frac{Le}{\boldsymbol{\tau}|u - u_p|}\right)\right] \tag{3.11}$$

Where;

$\boldsymbol{\tau}$: discrete phase relaxation time.

L_e : eddy length scale.

3.2.3 Interphase Momentum Exchange

The bubbles' trajectories are computed though the integration of the force-balance equations over each bubble in every control volume cell. The changes in heat, mass, and momentum, either gained or lost by the bubble stream are then quantified. These quantities are then incorporated in the subsequent continuous phase calculations. This bi-directional coupling is achieved in the simulations through alternately solving bubbles' and molten steel equations until the solutions in both phases are converged.

The above bi-directional two-way coupling shows the influence of the continuous phase on the bubble phase via drag and turbulence transfer, whereas, bubble phase reduces the mean momentum and turbulent kinetic energy of the fluid continuous phase through source terms. Momentum transfer from the continuous phase to the discrete phase is computed in ANSYS-FLUENT code by examining the change of bubbles' momentum as they pass through each control volume in the domain. Bubbles' momentum change in a computational cell is considered a source term in molten steel momentum equations and is calculated by the equation (3.12).

$$\vec{\boldsymbol{F}} = \sum_{i}^{N} \frac{18\mu \quad C_D Re_{rel}}{24\rho_P d_p^2} (\vec{u}_P - \vec{u}) \dot{m}_P \Delta t \tag{3.12}$$

Here,

N: number of bubbles in a computational cell.

$\dot{m}_p$: mass flow rate of gas bubbles (kg/s).

μ : molten steel dynamic viscosity (Pa.s).

Re: relative Reynolds number.

Δt : time step (s).

3.2.4 DPM boundary conditions

Interaction of bubbles with boundaries can be included in simulations to identify the fate of each individual trajectory. The boundary conditions (B.C.) that are used with the present DPM simulations are the following:

A. **Escape B.C.:** when a particle impacts a boundary, trajectory calculations is terminated.

B. **Reflect B.C.:** a particle can be reflected from boundary walls with either elastic collision (coefficient of restitution=1).

3.3 Simulation General Setup

GAMBIT and ANSYS-FLUENT are the pre-processor for CAD/meshing and the commercial code for the two-phase simulations, respectively. Initially, molten steel flow field is solved for different casting speeds. Then for each casting speed, Discrete Phase Model (DPM) is used to conduct the parametric study for different argon injection rates and bubble sizes.

3.3.1 Simulation Domain

The configuration domain of SEN and mold is initially drawn to the dimensional specifications of **Error! Reference source not found.**. But due to the two-fold symmetry, only a 3-D quarter model is used to reduce computational costs of simulation, see Figure 3.3.

Table 3.3:Dimensions of SEN/mold simulation domain.

Mold Thickness (m)	0.22
Mold Width (m)	1
Simulation length (m)	4
SEN type	Bifurcated with mountain bottom
SEN Internal diameter (bore) (m)	0.075
SEN External diameter (m)	0.085

Port angle (degrees)	15° (downward)
Port dimensions (mm)	60 X 70
SEN submergence depth (mm)	120

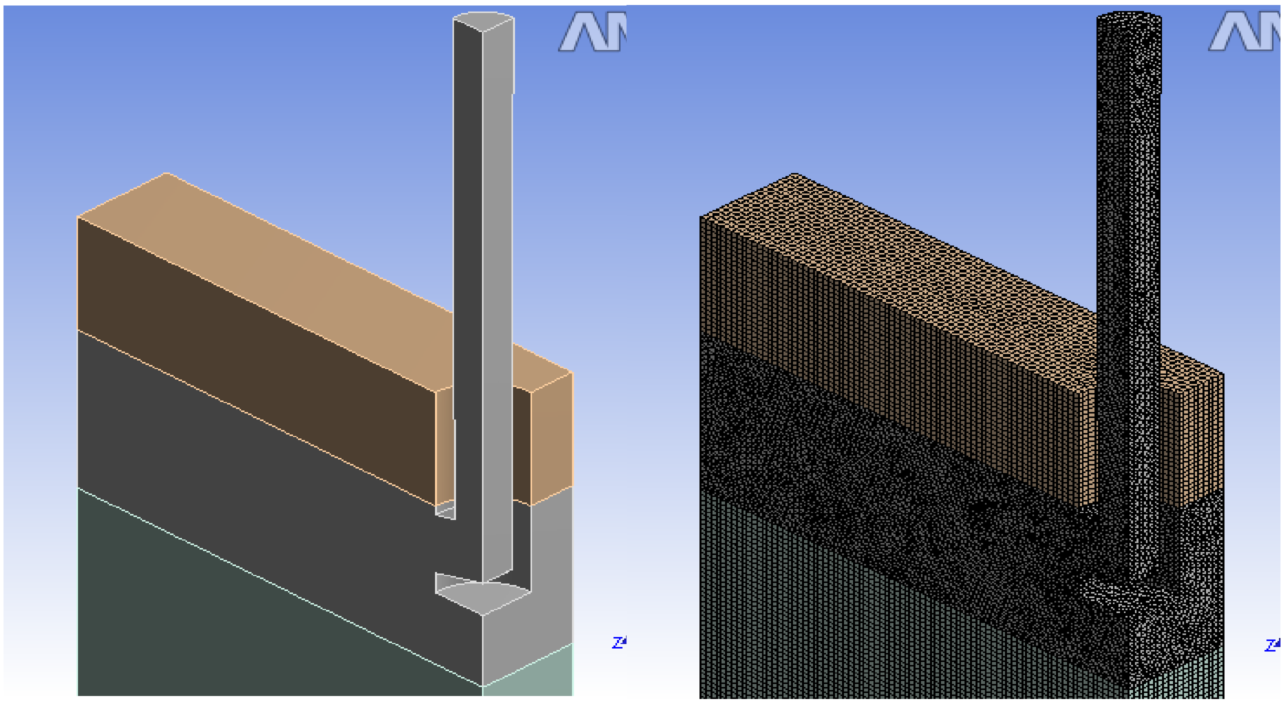

a) Before meshing b) After meshing

Figure 3.3: The 3-D quarter model (top geometrical section) before and after meshing.

3.3.2 Boundary Conditions

Proper selection of the problem-dependent boundary conditions, for both continuous phase and discrete phase, is critical for satisfactory simulations. For isothermal simulations, the main boundary conditions are shown in Table 3.4.

Table 3.4: boundary conditions of isothermal simulations.

Location of the boundary	Boundary condition
SEN entry	Inlet Velocity (m/s) ≈0.7, 1, 1.3 Turbulence Intensity = 5 % Hydraulic diameter = 0.075 mm

Mold Outlet	Pressure Outlet =101.325 KPa Hydraulic Diameter = $\frac{2*a*b}{(a+b)}$ = 0.36 Turbulence intensity=2% Escape (DPM)
Symmetry planes	Zero normal velocity. Zero normal gradients of all variables. Elastic collision (DPM)
Mold top surface	Shear stress = 0 Pa (free-surface) Escape (DPM)
Mold narrow and wide walls	No-slip conditions Elastic collision (DPM)
SEN walls	No-slip conditions Elastic collision (DPM)

For non-isothermal simulations, in addition to the previous boundary conditions, additional boundary conditions are incorporated for energy-related simulations and are shown in Table 3.5.

Table 3.5: Additional boundary conditions for non-isothermal simulations.

Location	Boundary condition
SEN entry	Temperature =1828 K (Superheat =25K)
Mold Outlet	Temperature = 1073 K
Symmetry planes	Adiabatic conditions or zero normal temperature gradient ($\frac{\partial T}{\partial n}$)
Mold top surface	Zero Thermal Flux
Mold narrow and wide walls	Liquidus Temperature = 1803 K
SEN walls	Zero Thermal Flux

3.3.3 Model Assumptions

To solve the fields of different variables, namely velocity, temperature and pressure, a suitable set of governing equations and boundary condition must be established beforehand. Also, reasonable simplification of governing equations without affecting the problem physics is recommended. The assumptions of the present simulations are the following:

a) Two-phase flow is assumed bubbly and incompressible.
b) Slag layer effects are neglected.
c) Liquid steel is treated as a Newtonian[18] fluid.
d) Effects of solidified shell and mold oscillation on flow are ignored.
e) Argon bubbles are assumed spherical with uniform size.
f) Effects of coalescence and break up of bubbles are neglected.

3.3.4 Physical Properties of Molten Steel and Argon Gas

Physical properties for both molten steel and argon gas are shown in Table 3.6. Argon gas volume is expected to expand to about five times due to temperature difference, i.e. from ambient to 1550 C° inside stopper-rod. So, the original argon flow rate increases by fivefold and the gas density decreases from 1.622 kg/m^3 to 0.3245 kg/m^3.

Table 3.6: physical properties of molten steel and argon gas.

Physical Property	Value
Molten steel density (kg/m^3)	7000
Molecular viscosity of molten steel (kg/m.s)	0.0055
Specific heat (cp) (j/kg.k)	720
Thermal conductivity (W/k.m)	26
Argon density (kg/m^3) (after expansion)	0.32456

[18] A fluid whose stress at each point is linearly proportional to its strain rate i.e. stress versus strain rate curve is linear with viscosity as the constant of proportionality.

Gravity (m/s^2)	9.81

3.3.5 Caster's Operational and Argon Injection Parameters

The present numerical parametric study involves different operational as well as argon injection parameters. The selected operational parameters, shown in Table 3.7, correspond to a specific conventional slab caster in Saudi Arabia. Moreover, the inlet velocities of SEN are calculated by expression (3.12).

Table 3.7: Casting speeds and SEN velocities for simulations without gas injection.

casting speed (m/min)	0.8	1.1	1.5
Inlet Velocity (m/s)	0.7094	1.001	1.330

$$\text{SEN inlet velocity} = \text{casting speed} * \left(\frac{\text{Slab Area}}{\text{SEN Area}}\right) * \left(\frac{\text{Solid steel Density}}{\text{Liquid steel density}}\right) \qquad (3.12)$$

Where; slab area= 0.22 m^2; SEN area= 0.0044179 m^2; solid steel density= 7500 kg/m^3; liquid steel density= 7000 kg/m^3.

For the two-phase simulations, three different injection rates and three bubble sizes were used for every casting speed and the specific conditions are shown in **Error! Not a valid bookmark self-reference.**. Hence, a total of thirty cases were simulated for isothermal conditions and another set of thirty cases were simulated for non-isothermal conditions, including the no-injection cases.

Table 3.8: DPM setup for argon injection simulations of the 3-D quarter model.

Argon gas injection volumetric flow rate Q_{gas}			mass flow rate	No. of bubbles injected per time step**		
LPM before expansion	LPM after expansion	**m^3/s** after expansion*	(kg/s)	D_{bubble}= 4 mm	D_{bubble}= 5 mm	D_{bubble}= 6 mm

2.5	12.5	2.083E-04	1.690E-05	8	4	2
5	25	4.170E-04	3.381E-05	16	8	5
7.5	37.5	6.250E-04	5.071E-05	23	12	7
* conversion factor = 0.000016667 (lit/min to m^3 /sec) **Simulation time = 5 seconds & time step= 0.005 second.						

3.3.6 ANSYS- FLUENT Simulation Setup

The commercial CFD package ANSYS-FLUENT contains many different options, like turbulence models and discretization schemes, to suit different applications. The proper selection of these options is critical for the generation of accurate simulation results. The main options used in ANSYS-FLUENT simulations are listed below:

a) k-ω turbulence model with low-Re corrections for turbulence modeling.
b) Second order upwind scheme is used for TKE, momentum and ω equations.
c) Pressure–velocity coupling is based on the Semi-Implicit Method for Pressure-Linked Equations (SIMPLE) algorithm.
d) Argon bubbles are injected as a group of similar sizes at SEN surface for every time step.
e) Relative residual threshold is 0.001 for all variables except energy where it's $1x10^{-6}$.
f) Under-relaxation factors are as follows:

pressure	TKE (k)	specific dissipation (ω)	momentum	DPM source	all other factors
0.3	0.8	0.8	0.7	0.5	1

Chapter 4: Results and Discussion

4.1 Grid Independence Analysis

Grid-independence study, or grid sensitivity, is conducted to improve the simulation output by reducing discretization errors and obtain the best achievable results to be a benchmark for further simulations. Grid-independence study starts with a coarse mesh simulation, then, gradually the mesh is refined until differences between outputs of a specific variable are smaller than a pre-defined error (< 0.1). For the present grid-independence study, velocities at four locations at the top surface are used for comparison purposes. The outputs of grid independence study are shown in Table 4.1. The mesh with 621,000 cells fulfills grid study criteria compared to other mesh sizes. This mesh is expected to provide a reasonably accurate grid-independent solution or results. The stated mesh size was used consistently in the numerical parametric study. It is noteworthy that high mesh refinements generate larger errors due to the magnification of round-off errors.

Table 4.1: The outputs of velocities (in m/s) at four points on meniscus level as well as the error percentages between simulation outputs of different mesh sizes.

No. nodes (10^3)	size (mm)	Quarter Vel.(1) (m/s)	Quarter Vel. (2) (m/s)	Symm. Vel.(1) (m/s)	Symm. Vel.(1) (m/s)	Error % Quarter Vel. (1)	Error % Quarter Vel.(2)	Error % Symm. Vel. (1)	Error % Symm. Vel.(2)
168.3	11.0	0.304	0.229	0.306	0.215				
218.9	10.0	0.242	0.167	0.234	0.173	25.41	37.05	30.45	24.08
313.6	9.0	0.249	0.134	0.245	0.099	2.89	25.08	4.45	74.75
422.7	8.0	0.249	0.156	0.250	0.137	0.02	14.24	1.66	27.75
621.4	7.0	0.244	0.169	0.241	0.150	2.02	7.64	3.56	8.44
987.8	6.0	0.230	0.151	0.224	0.138	6.47	11.73	7.80	8.90

*Points coordinates: at symmetry plane: Velocity (1) at X= -0.4, Y=0, Z = 0.055 m; Velocity (2) at X= -0.2, Y=0, Z= 0.055 m, and at quarter-distance of N.F: Velocity (1) at X= -0.4, Y=0, Z = 0.11 m; Velocity (2) at X= -0.2, Y=0, Z= 0.11 m.

4.2 Surface Velocity Measurement and CFD Predictions

4.2.1 Predictions of Velocity Profiles for Different Casting Conditions

Simulations results of velocity profiles along the centerline, i.e. symmetry line parallel to mold wide face, for different casting conditions indicate some general trends. For the no-injection profiles, the meniscus surface velocity increases with the casting speed and results in a single peak halfway toward SEN, but, surface velocity decreases upon approach to SEN walls. This matches simulations and PIV results of Reference [55] as shown in Figure 4.1. On the other hand, the velocity profiles with argon injection results in two velocity peaks on meniscus level as seen from Figure 4.6 through Figure 4.11. These peaks flow in opposite directions as will be shown through the velocity vector plots in Section (4.4).

The magnitudes of the developed peaks vary with bubble size, casting speed and injection flow rate. For example, high casting speeds with low injection flow rates form a small secondary velocity peak near SEN. But, at low casting speeds, high injection rates lead to the formation of a large secondary velocity peak around SEN which may cause an "open eye" at slag layer. The "open-eye" phenomenon is considered the main source for steel re-oxidations and subsequent formation of large exogenous inclusions in liquid steel.

Argon injection with different casting speeds generally increases the maximum velocity of the primary peak that moves toward SEN, see Tables 4.3- 4.5. For a constant casting speed and different bubble sizes, this peak is reduced gradually as injection rate increases, whereas, a secondary peak near SEN walls increases and moves in opposite direction to the primary peak. This is caused by the higher concentrations of bubbles, with high argon flow rates, around SEN outlet which collectively modify liquid steel flow at that region.

Moreover, high casting speeds reduce the influence of injection rate on surface velocity profile as seen from Figure 4.10. Also, smaller bubble sizes, for different injection rates, have more influence on the secondary peak compared to larger bubbles. This is mainly due to the increase in the number of bubbles and subsequent high concentrations around SEN as shown in bubble dispersion figures, Section (4.3).

Generally, the actual surface profile in continuous casters does not match the simulated velocity profile due to the floating viscous slag layer. This viscous layer dampens surface fluctuations and peaks strongly. However, the predicted velocity peaks might induce instability at the slag/liquid steel interface which might lead to slag entrainment. Therefore, precise control of argon injection flow rate is critical to avoid slag entrainment. Simulations results can provide a guideline criterion when coupled with slag entrainment studies.

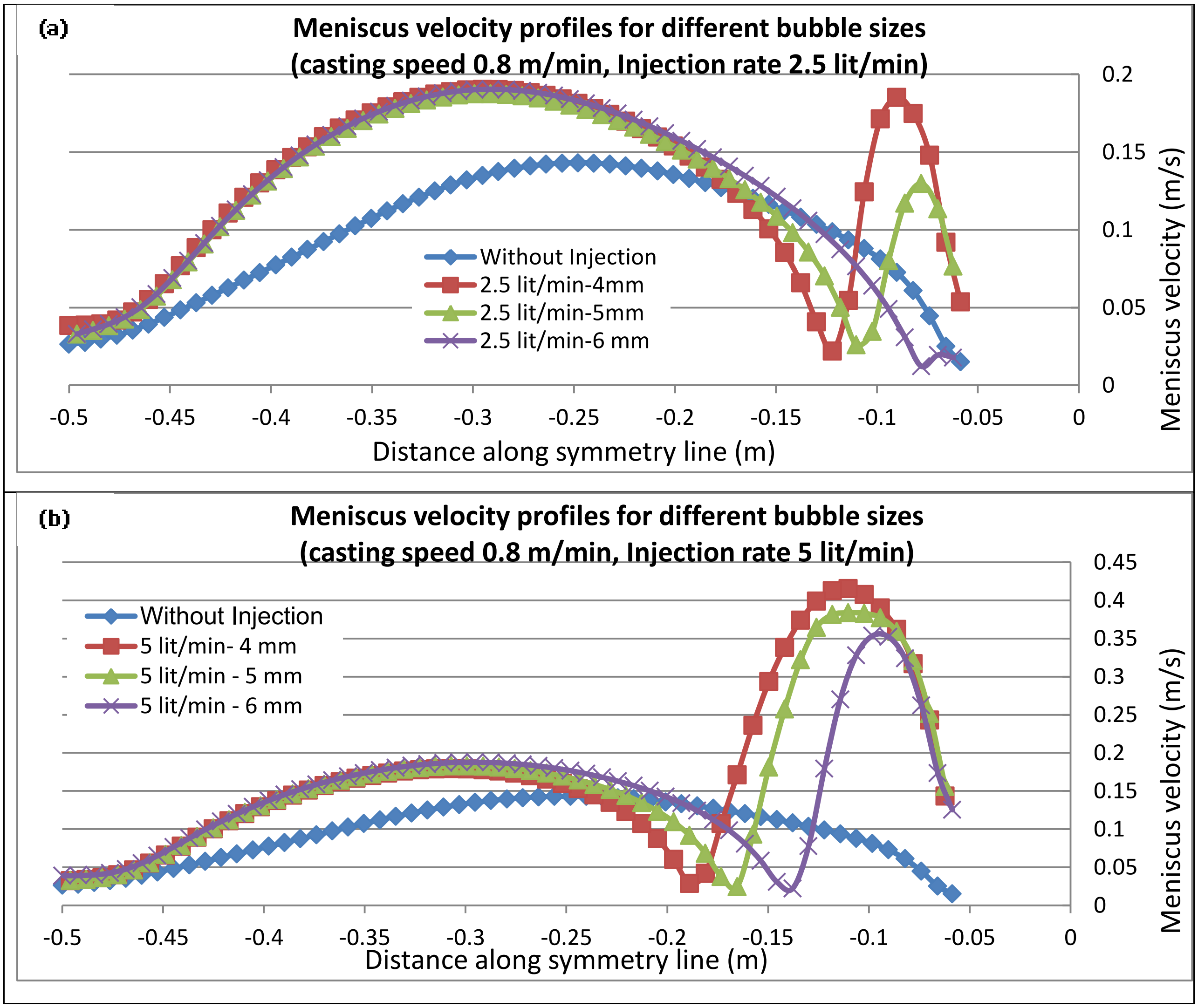

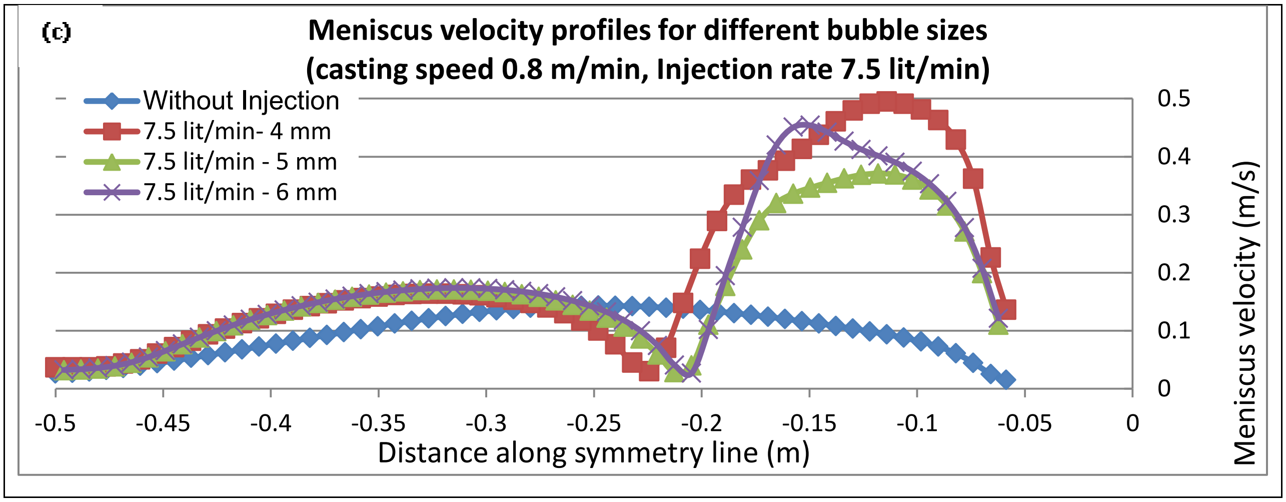

Figure 4.1: Effects of different bubble sizes on the velocity profiles, along top symmetry line, for a constant casting speed of 0.8 m/min and different injection rates: (a) 2.5 LPM, (b) 5 LPM, (c) 7.5 LPM.

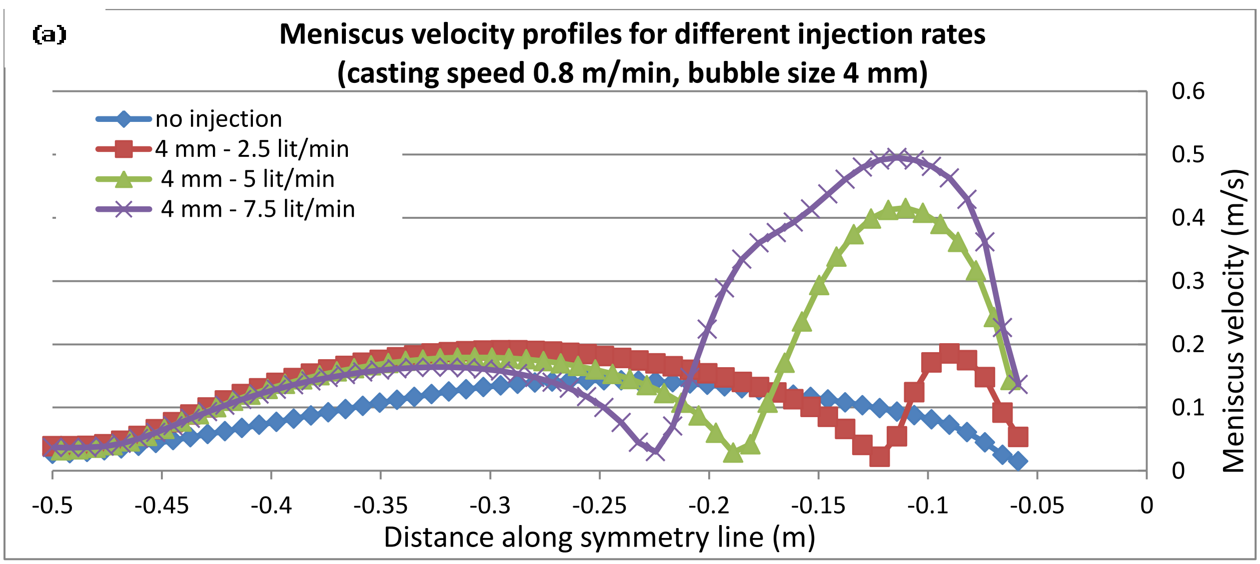

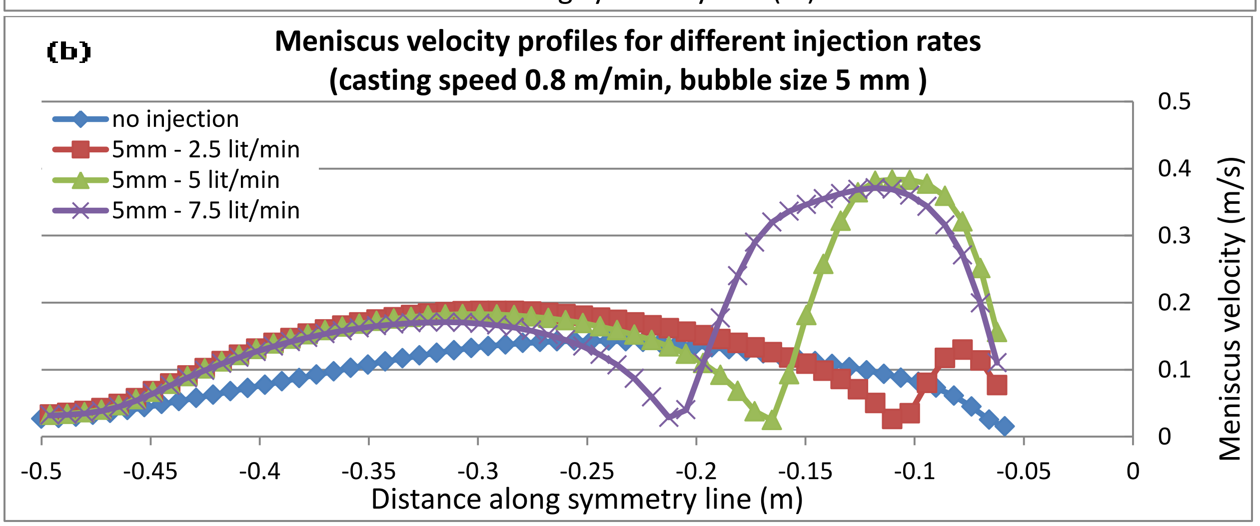

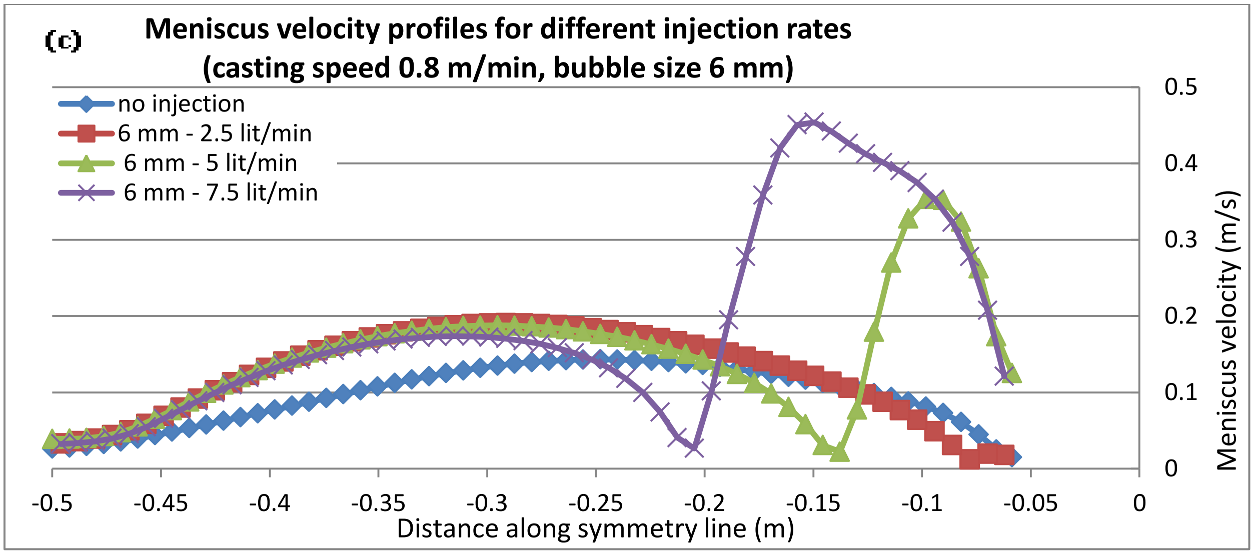

Figure 4.2: Effects of different injection rates on velocity profiles, along top symmetry line, for a constant casting speed of 0.8 m/min and different bubble diameters: (a) 4 mm, (b) 5 mm, (c) 6 mm.

Table 4.2: Surface velocities along centerline for different injection conditions for a constant casting speed of 0.8 m/min.

Injection Rate (liter/min)	Bubble Diameter (mm)	Maximum velocity (m/s)				Minimum velocity at top surface (interference of peaks)	
		1st Peak	Location of 1st peak along symmetry line	2nd Peak	Location of 2nd peak along symmetry line	Velocity (m/s)	Interference point (m)
0	NA	0.145	-0.25	-	-	-	-
2.5	4	0.192	-0.28	0.188	-0.09	0.02	-0.125
	5	0.188	-0.29	0.128	-0.08	0.024	-0.11
	6	0.192	-0.28	0.02	-0.07	0.012	-0.075
5	4	0.17	-0.3	0.42	-0.11	0.025	-0.19
	5	0.17	-0.3	0.38	-0.105	0.02	-0.165
	6	0.18	-0.3	0.36	-0.09	0.02	-0.14
7.5	4	0.16	-0.32	0.5	-0.12	0.02	-0.225
	5	0.17	-0.32	0.37	-0.12	0.02	-0.22
	6	0.17	-0.31	0.46	-0.15	0.025	-0.2

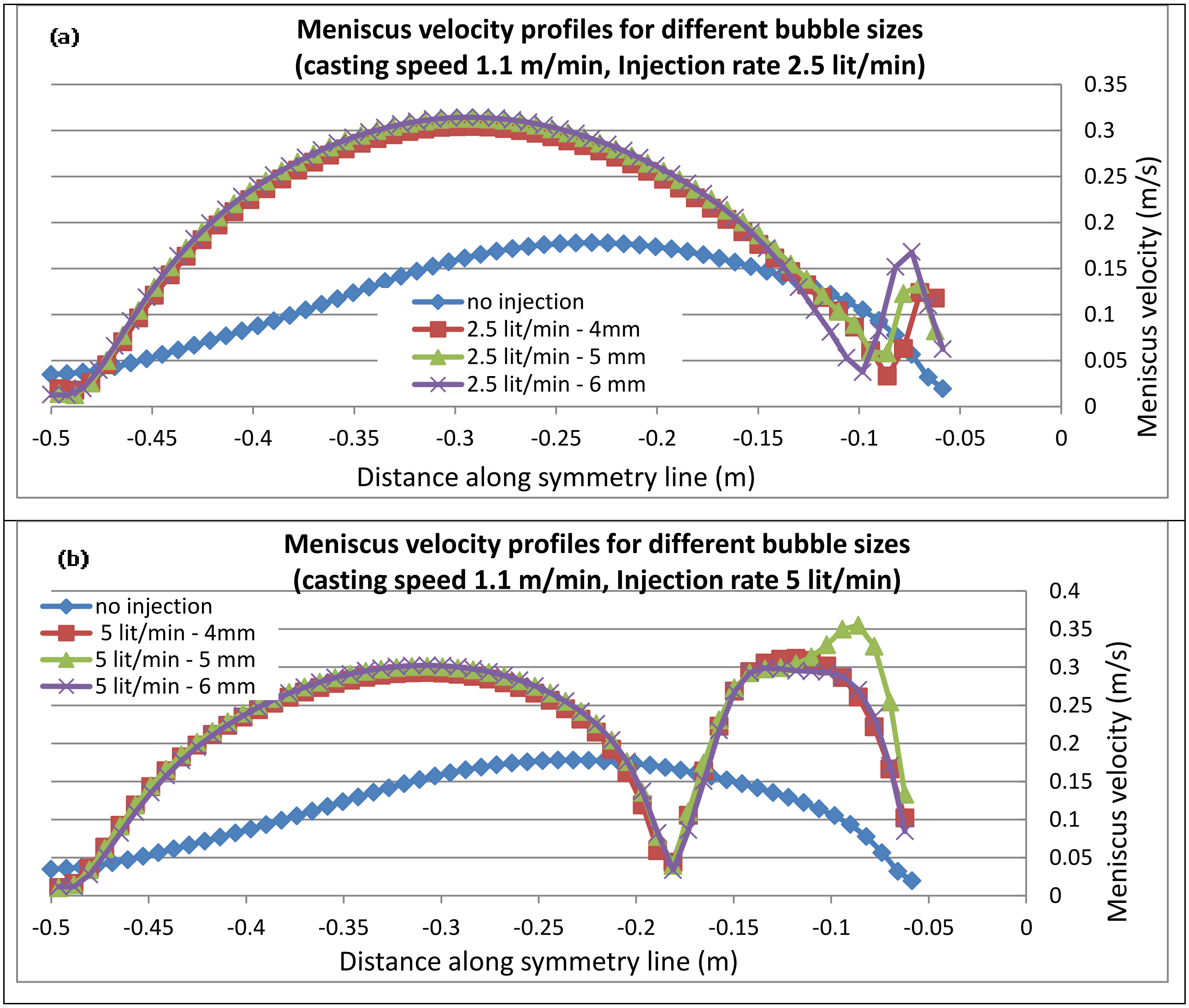
(a)
Meniscus velocity profiles for different bubble sizes
(casting speed 1.1 m/min, Injection rate 2.5 lit/min)
no injection
2.5 lit/min - 4mm
2.5 lit/min - 5 mm
2.5 lit/min - 6 mm
Meniscus velocity (m/s)
Distance along symmetry line (m)
0
0.05
0.1
0.15
0.2
0.25
0.3
0.35
-0.5
-0.45
-0.4
-0.35
-0.3
-0.25
-0.2
-0.15
-0.1
-0.05
0
(b)
Meniscus velocity profiles for different bubble sizes
(casting speed 1.1 m/min, Injection rate 5 lit/min)
no injection
5 lit/min - 4mm
5 lit/min - 5 mm
5 lit/min - 6 mm
Meniscus velocity (m/s)
Distance along symmetry line (m)
0
0.05
0.1
0.15
0.2
0.25
0.3
0.35
0.4
-0.5
-0.45
-0.4
-0.35
-0.3
-0.25
-0.2
-0.15
-0.1
-0.05
0

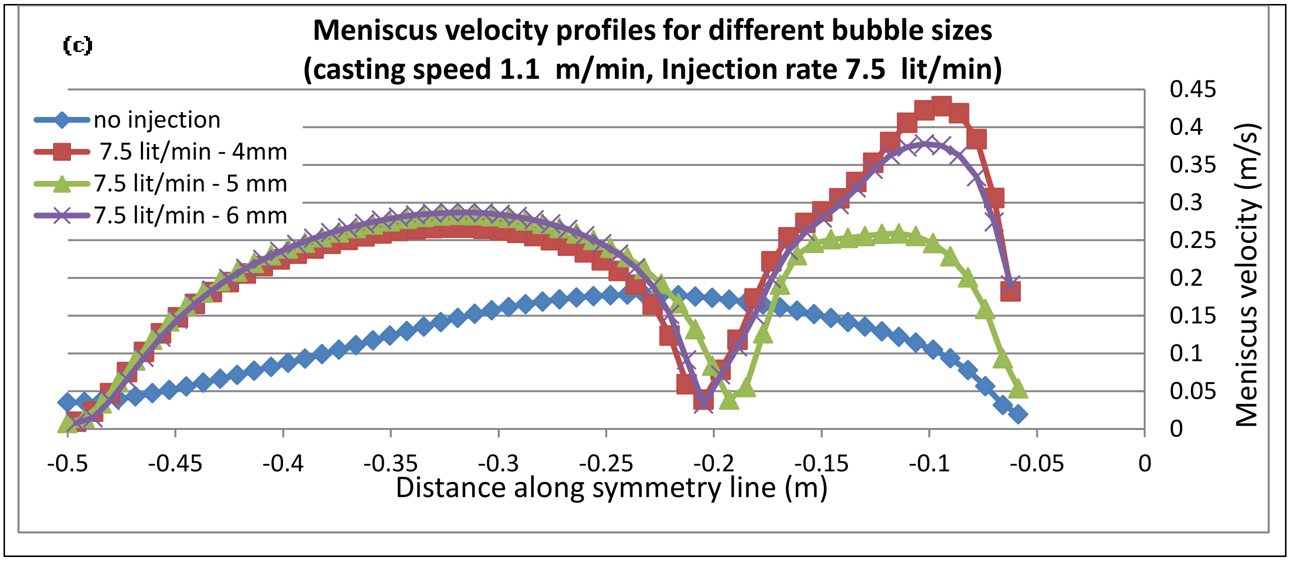

Figure 4.3: Effects of different bubble sizes on the velocity profiles for a constant casting speed of 1.1 m/min and different injection rates: (a) 2.5 LPM, (b) 5 LPM, (c) 7.5 LPM.

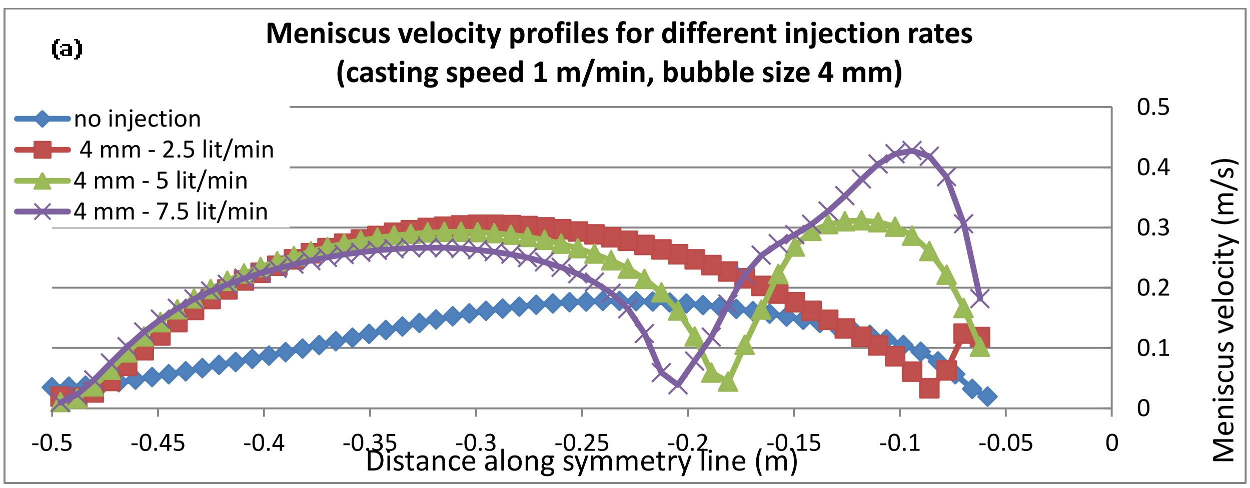

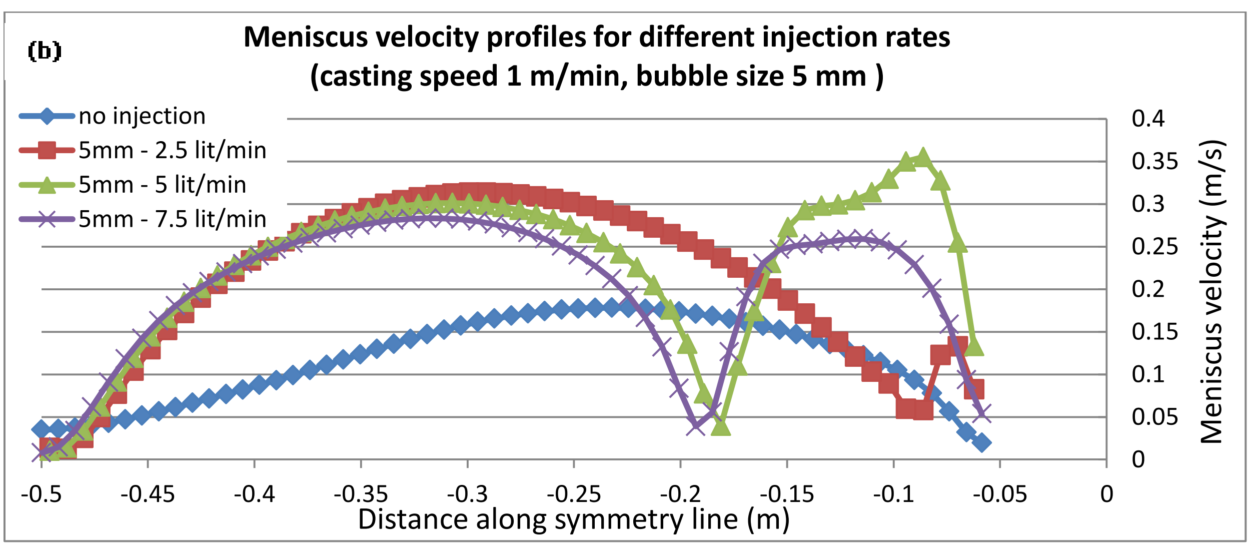

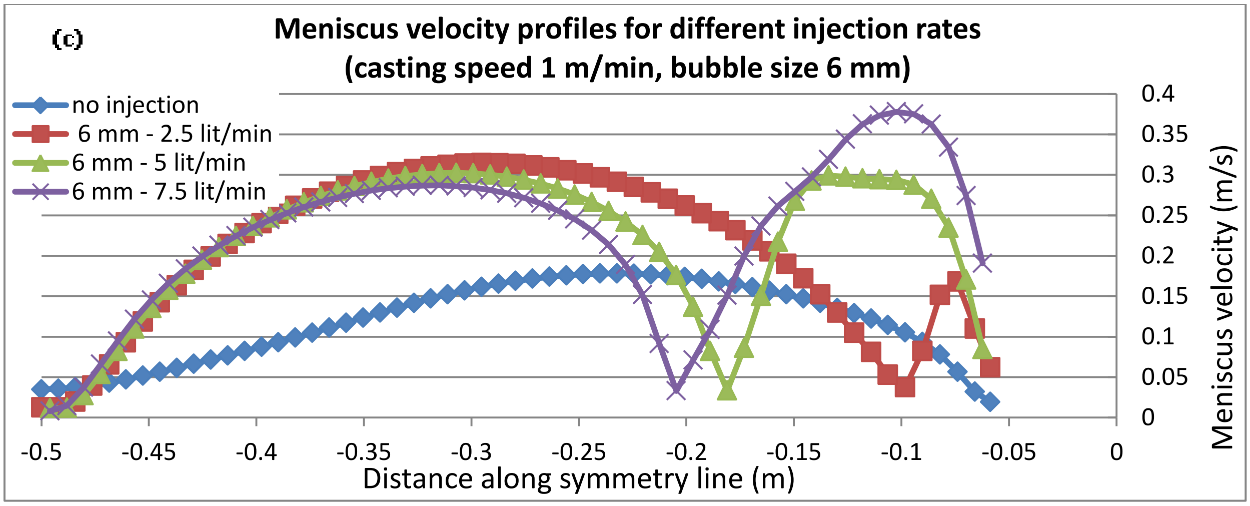

Figure 4.4: Effects of injection rates on velocity profiles along symmetryline for a constant casting speed of 1.1 m/min and different bubble diameters: (a) 4 mm, (b) 5 mm, (c) 6 mm.

Table 4.3: Centerline velocities for different injection conditions and a constant casting speed of 1.1 m/min.

Injection Rate (liter/min)	Bubble Diameter (mm)	Maximum velocity (m/s)				Minimum velocity at top surface (e.g. two waves meet)	
		1st Peak	Location of 1st peak along symmetry line	2nd Peak	Location of 2nd peak along symmetry line	Velocity (m/s)	Interference point (m)
0	N/A	0.18	-0.23	-	-	-	-
2.5	4	0.3	-0.29	0.13	-0.07	0.03	-0.085
	5	0.305	-0.3	0.13	-0.07	0.05	-0.11
	6	0.31	-0.3	0.17	-0.075	0.04	-0.1
5	4	0.29	-0.31	0.32	-0.12	0.03	-0.18
	5	0.295	-0.31	0.35	-0.09	0.04	-0.18
	6	0.3	-0.3	0.3	- 0.14	0.04	-0.18
7.5	4	0.27	-0.33	0.43	-0.09	0.04	-0.21
	5	0.275	-0.325	0.26	-0.125	0.04	-0.19
	6	0.28	-0.325	0.38	-0.1	0.04	-0.2

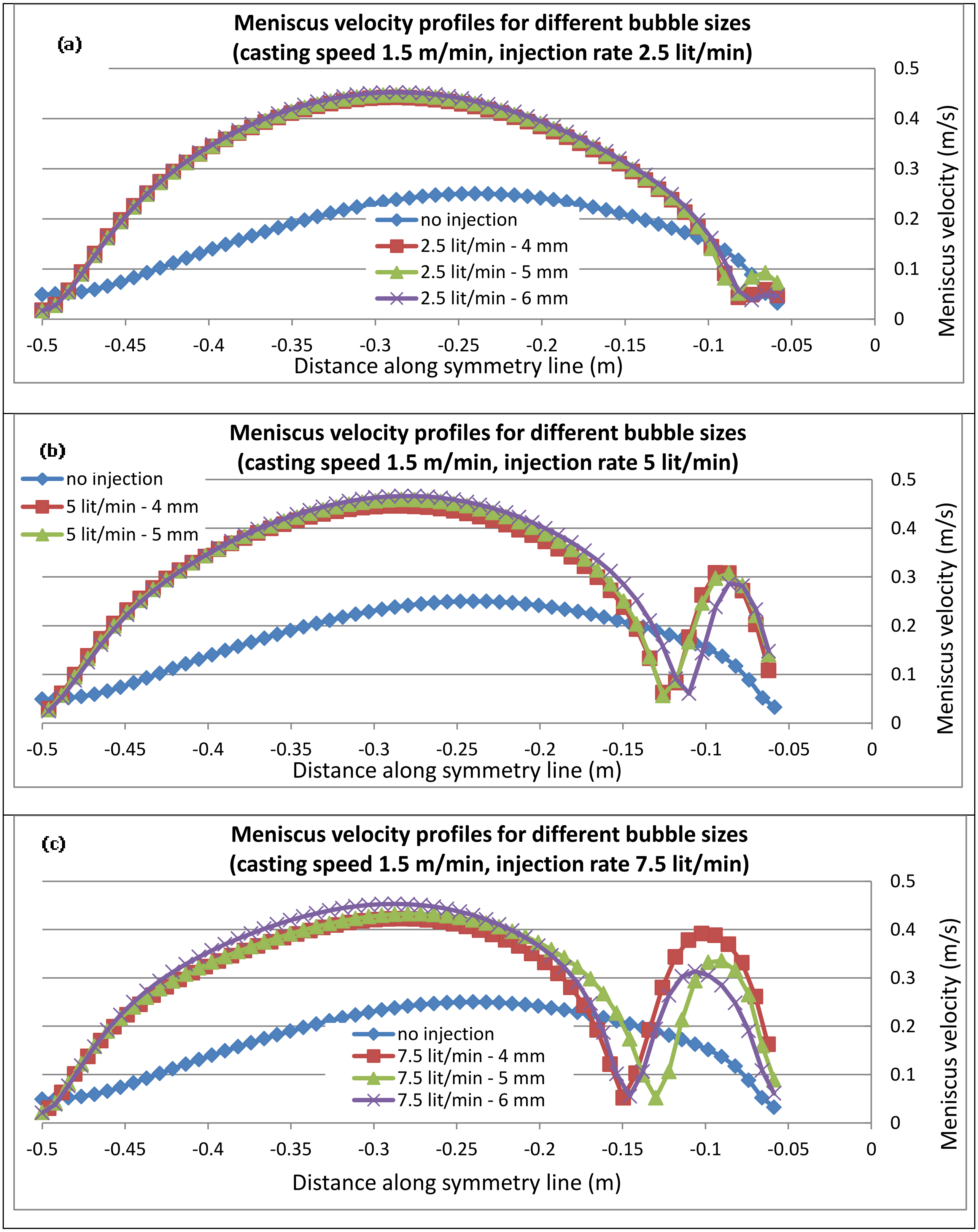

Figure 4.5: Effects of different bubble sizes on the velocity profiles, along top symmetryline, for a constant casting speed of 1.5 m/min and different injection rates: (a) 2.5 LPM, (b) 5 LPM, (c) 7.5 LPM.

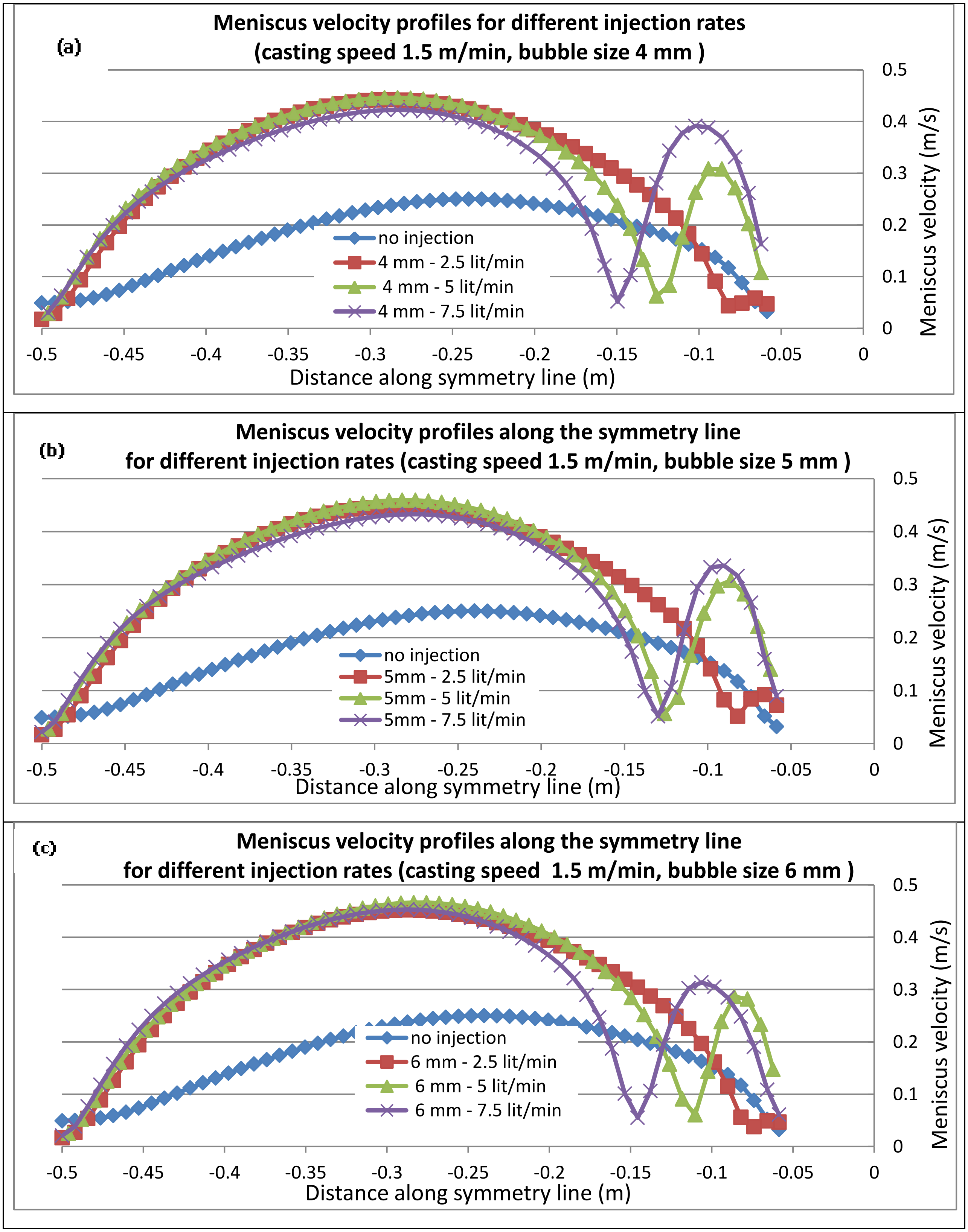

Figure 4.6: Effects of injection rates on velocity profiles for a constant casting speed of 1.5 m/min for different bubble diameters: (a) 4 mm, (b) 5 mm, (c) 6 mm.

Table 4.4: Meniscus velocities along centerline plane for different injection conditions for a constant casting speed of 1.5 m/min.

Injection Rate (liter/min)	Bubble Diameter (mm)	Maximum velocity (m/s)				Minimum velocity at top surface (interference)	
		1st Peak	Location 1st Peak along symmetry line	2nd Peak	Location of 2nd Peak along symmetry line	Velocity (m/s)	Interference point (m)
0	N/A	0.25	-0.24	-	-	-	-
2.5	4	0.44	-0.28	0.06	-0.06	0.04	-0.08
	5	0.445	-0.28	0.09	-0.06	0.04	-0.08
	6	0.45	-0.28	0.05	-0.06	0.04	-0.07
5	4	0.45	-0.28	0.32	-0.09	0.05	-0.125
	5	0.455	-0.28	0.31	-0.09	0.05	-0.125
	6	0.46	-0.275	0.28	-0.08	0.06	-0.11
7.5	4	0.42	-0.28	0.39	-0.1	0.05	-0.15
	5	0.43	-0.28	0.335	-0.09	0.05	-0.13
	6	0.45	-0.28	0.31	-0.105	0.05	-0.145

4.2.2 Comparison Between Experimental and Simulations Results

Based on the experimental results in Section (**Error! Reference source not found.**2.2.4), Thomas et al. stated that "at the medium casting speed of 1.4 m/min, meniscus velocity is always positive (0.3 to 0.5 m/s), which indicates a consistent double-roll flow pattern in the mold. At the low casting speed of 1.0 m/min, meniscus velocities appear both positive and negative, indicating a complex flow pattern, with variable reversing flows"[88]. Their observations can be roughly correlated to the formation of the two velocity peaks and the interference point as seen in velocity profiles of previous Section (4.2.1). The interference point, i.e. predicted intersection point of two waves on meniscus surface, depends on the injection rate and the casting speed. Also, the error percentages between the two peaks, shown in Table 4.5, highlight the influence of argon injection parameters on meniscus layer. This is seen from the positive and the negative percentages for different casting conditions.

Table 4.5: Error % between velocity peaks at mold surface for different casting conditions.

Injection Rate (lit/min)	Bubble Diameter (mm)	Casting Speed 0.8 m/min			Casting Speed 1.1 m/min			Casting Speed 1.5 m/min		
		Maximum velocity (m/s)		$\frac{\text{2nd Peak} - \text{1st Peak}}{\text{1st Peak}}$ %	Maximum velocity (m/s)		$\frac{\text{2nd Peak} - \text{1st Peak}}{\text{1st Peak}}$ %	Maximum velocity (m/s)		$\frac{\text{2nd Peak} - \text{1st Peak}}{\text{1st Peak}}$ %
		1st Peak	2nd Peak		1st Peak	2nd Peak		1st Peak	2nd Peak	
2.5	4	0.19	0.19	-2.08	0.3	0.13	-56.67	0.44	0.06	-86.36
	5	0.19	0.13	-31.91	0.305	0.13	-57.38	0.445	0.09	-79.78
	6	0.19	0.02	-89.58	0.31	0.17	-45.16	0.45	0.05	-88.89
5	4	0.17	0.42	147.06	0.29	0.32	10.34	0.45	0.32	-28.89
	5	0.17	0.38	123.53	0.295	0.35	18.64	0.455	0.31	-31.87
	6	0.18	0.36	100.00	0.3	0.3	0.00	0.46	0.28	-39.13
7.5	4	0.16	0.50	212.50	0.27	0.43	59.26	0.42	0.39	-7.14
	5	0.17	0.37	117.65	0.275	0.27	-1.82	0.43	0.335	-22.09
	6	0.17	0.46	170.59	0.28	0.38	35.71	0.45	0.31	-31.11

The magnitude of the secondary velocity peak increases to exceed the respective primary peak in the case of high injection rates combined with low casting speeds. Also, the interference point of the two peaks moves toward the narrow-face with high argon flow rates and/or low casting speeds. For instance, this interference point is approximately at quarter distance of wide-face between -0.18 to -0.21 m, for a casting speed of 1.1 m/min and injection rate of 5-7.5 lit/min. This might explain the complex flow behavior and possible reversal of velocity values as reported in the experimental study. However, at a higher casting speed, the primary peak magnitude, at the same location, always exceed the respective secondary peak values. This promotes a stable meniscus flow and prevents flow reversal behavior. In addition, the experimental results seen in Figure 2.9 (c), indicate that for high casting speeds and a constant injection rate, two main effects prevail which are the increase of meniscus velocity and the reduction of gas volume fractions. Such behavior of surface velocity matches simulations' results observed in velocity profiles. For example, for an injection rate of 7.5 lit/min and bubble diameter of 5 mm, the primary peak increases from 0.17 m/s to 0.43 m/s for the increase of casting speeds from 0.8 m/min to 1.5 m/min, respectively.

Furthermore, the experimentally measured surface velocities for a casting speed of 1.5 m/min and argon injection of 6 LPM range between 0.25-0.45 m/s. Whereas, simulations surface velocities range between 0.42-0.46 m/s for a casting speed of 1.5 m/min and injection rates range of 5-7.5 LPM. The simulations higher range might be due the shallower submergence depth of 150 mm compared to 185 mm in the experimental study. So, a qualitative agreement can be said to have been established for the surface velocities between simulation results and experimental measurements.

4.3 Bubble Dispersion

DPM trajectory calculations can support the visualization of bubbles' dispersion inside the simulation domain. For a constant bubble size, any increase of injection flow rate increases the bubbles density and spread inside the domain. For instance, small bubbles of 4 mm diameter are dispersed widely inside the mold and toward the narrow face compared to larger bubbles as seen in Figure 4.8 (a-i). Generally, bubble dispersion toward narrow face and wide face increases along with high casting speeds, high injection rates and small bubble sizes as shown in Figure 4.10. Also, there is a high possibility of bubble entrapment between dendritic arms during solidification, i.e. blister defects, due to the dispersion of bubbles toward mold sides.

Based on Danissov et al. [59] study, small bubbles ($D_{bubble} \leq 1$ mm) are expected to be dragged down in lower recirculation zone and spiral towards the inner radius with possible entrapment in the solidified shell. Similar entrapment is also expected for relatively larger bubbles which may breakup near the solidification front and get entrapped by internal hooks[19], shown in Figure 4.7. Thus, high bubble spread increases the probability of bubble entrapment at the meniscus region and subsequent quality defects such as pencil pipe [89].

[19] Sub-surface microstructural defect often accompanies deep oscillation marks in steels and caused by the vertical oscillation of the copper mold.

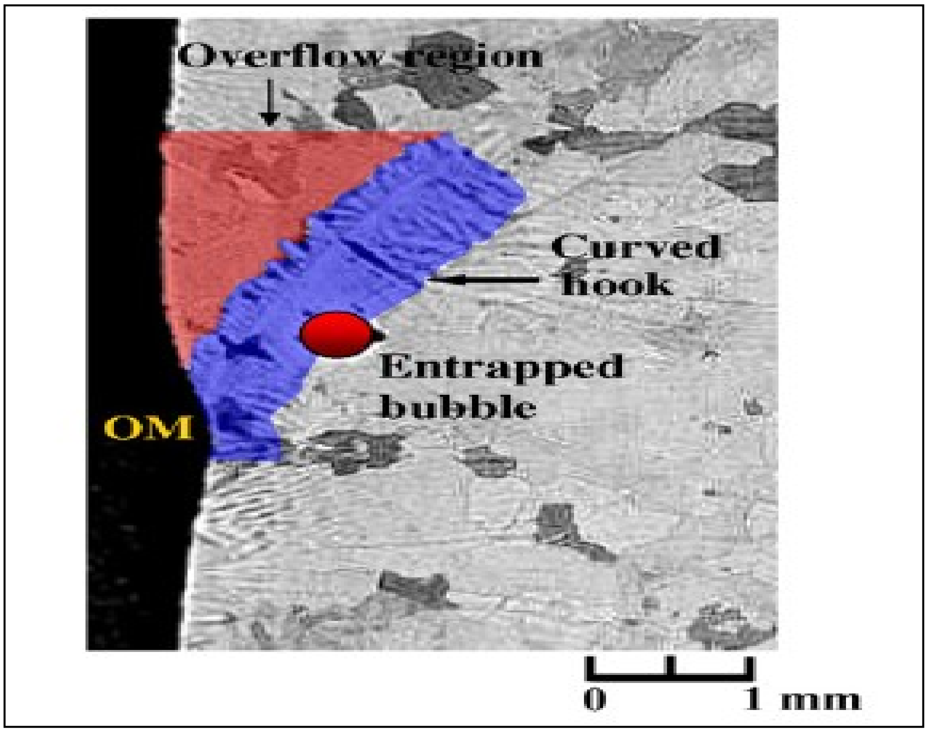

Figure 4.7: Optical micrograph of low-carbon steel sample showing entrapment of argon bubble by a curved hook-type oscillation mark [89].

Moreover, bubbles spread widely with higher argon flow rates toward the wide-face and form a semi-circumferential rim around SEN, as seen in Figure 4.9. Also, this rim might induce a transient behavior to the viscous slag layer due to the escaping bubbles. Therefore, the wear area around SEN walls is expected to increase with excessive argon flow rates.

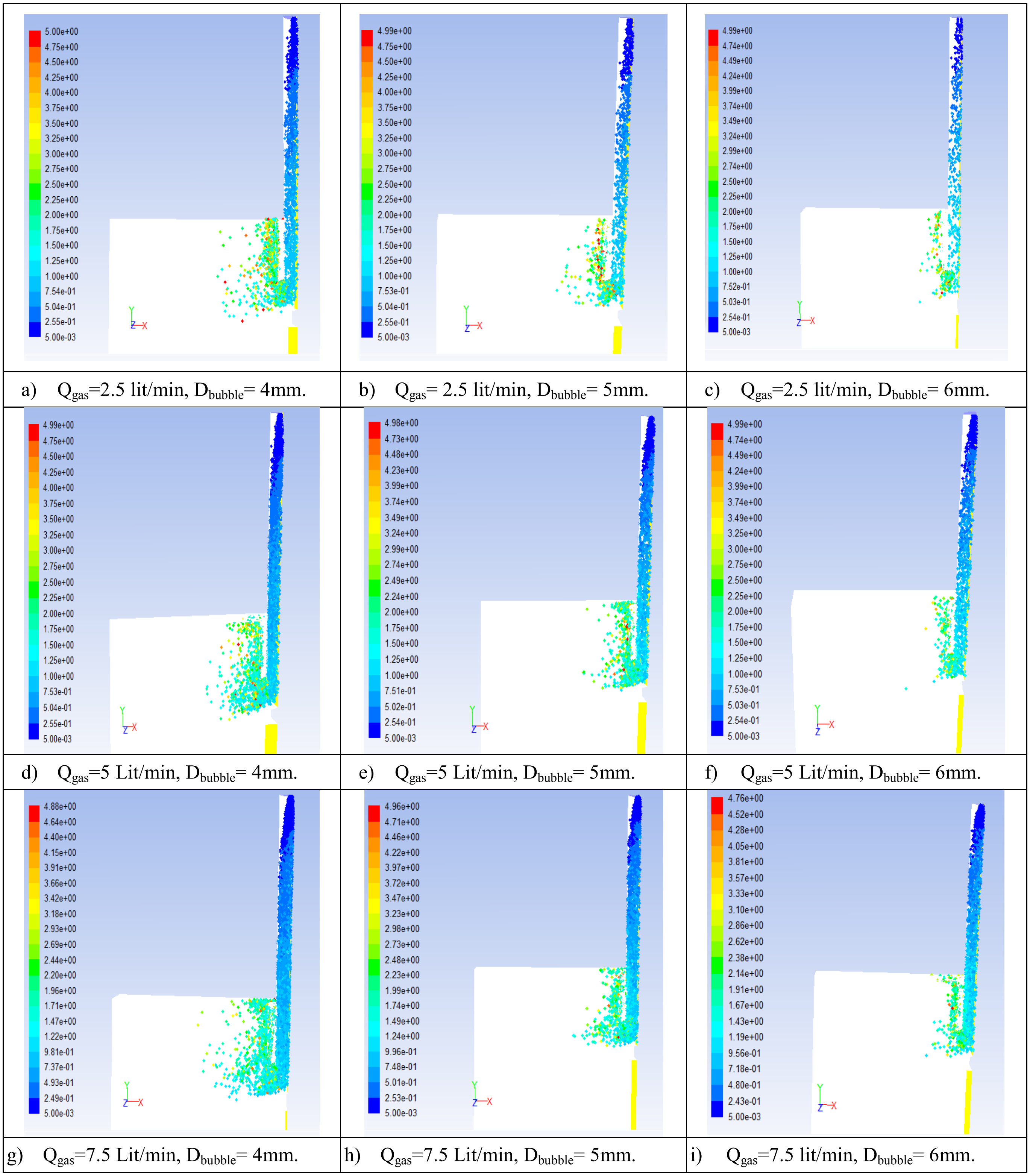

a) Q_{gas}=2.5 lit/min, D_{bubble}= 4mm.
b) Q_{gas}= 2.5 lit/min, D_{bubble}= 5mm.
c) Q_{gas}=2.5 lit/min, D_{bubble}= 6mm.
d) Q_{gas}=5 Lit/min, D_{bubble}= 4mm.
e) Q_{gas}=5 Lit/min, D_{bubble}= 5mm.
f) Q_{gas}=5 Lit/min, D_{bubble}= 6mm.
g) Q_{gas}=7.5 Lit/min, D_{bubble}= 4mm.
h) Q_{gas}=7.5 Lit/min, D_{bubble}= 5mm.
i) Q_{gas}=7.5 lit/min, D_{bubble}= 6mm.

Figure 4.8: Bubble dispersion for injection cases and a constant casting speed of 1 m/min. (Color code: residence time in seconds)

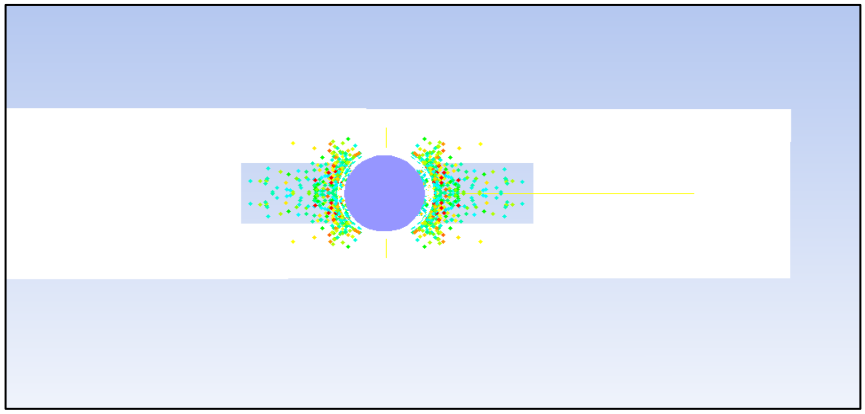

a) Q_{gas}= 2.5 lit/min

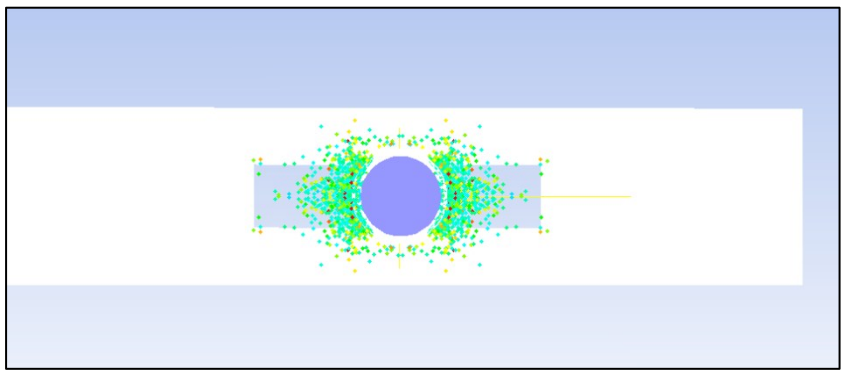

b) Q_{gas}= 5 lit/min

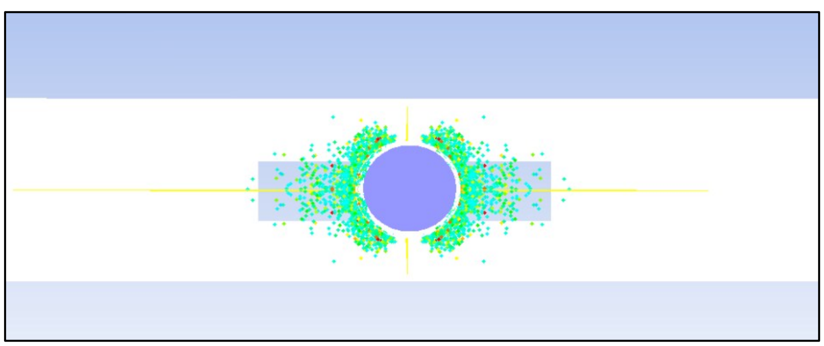

c) Q_{gas}= 7.5 lit/min

Figure 4.9: The top view of bubbles spread around SEN for a constant casting speed of 1.1 m/min and bubble diameter of 5 mm; for different injection rates: (a) 2.5 LPM, (b) 5 LPM, (c) 7.5 LPM.

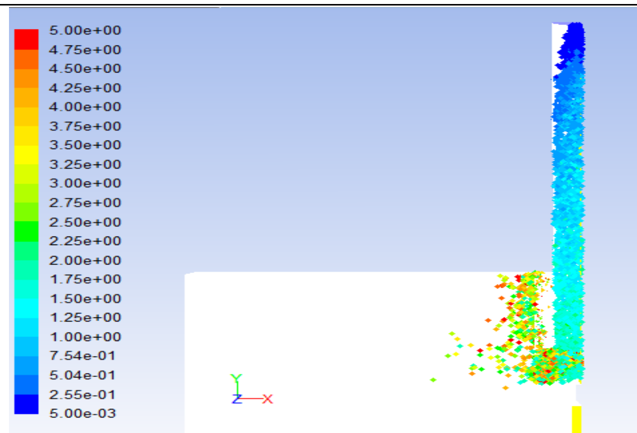

a) Casting speed= 0.8 m/min

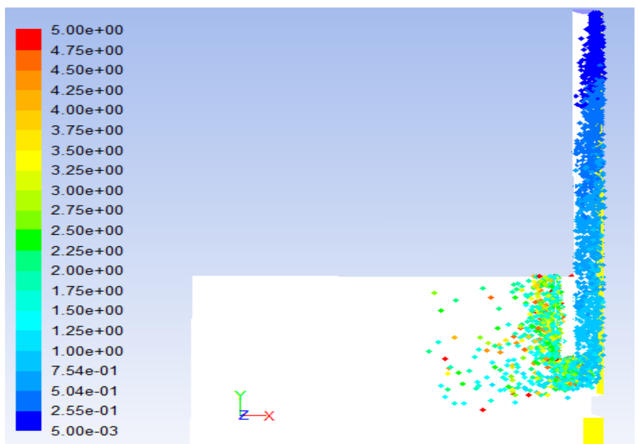

b) Casting speed = 1.1 m/min

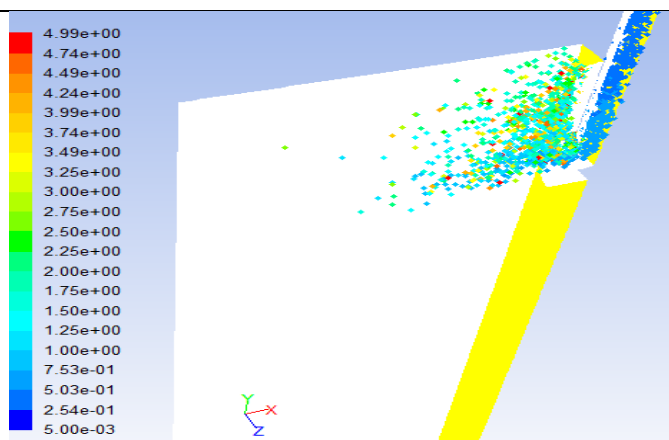

c) Casting speed= 1.5 m/min

Figure 4.10: Bubble dispersion of a constant injection rate of 2.5 LPM and bubble diameter = 4 mm; for different casting speeds: (a) 0.8 m/min, (b) 1.1 m/min, (c) 1.5 m/min. (Color code: residence time in seconds)

4.4 Velocity Contours and Vector plots

No-injection simulations indicate a generally uniform velocity inside SEN with two small eddies at the bottom centerline and at port's upper area. Also, the maximum velocity inside SEN occur near these eddies as shown in velocity contours (Figure 4.11 (a) - 4.16 (a)).

Inside the mold, the molten steel jet velocity decreases and gradually becomes zero at the narrow face, where it impinges and forms the double recirculation zones. Based on Alnajjar et al. [66] single-phase parametric study, the steel jet angle is steeper downward compared to the nozzle angle which matches the predictions of the present no-injection simulations.

When argon injection is integrated into simulations, velocity contours and vector plots show noticeable changes in both SEN and mold regions. For instance, argon bubbles reduce the molten steel velocity near injection points, but this effect is less-dominant near SEN outlet port. Inside the mold, bubbles have two main effects on fluid flow, namely, lift the outlet jet upward which increases the meniscus velocity as well as oppose the downward flow around SEN walls.

For high injection flow rates, the upward moving bubbles reverse the molten steel flow direction around SEN wall, and thereby reduce the diameter of the upper recirculation zone by forming a small recirculation zone. However, for low injection rates and high casting speeds, the bubbles' influence on the recirculation zone is less-dominant because argon volume fraction is reduced noticeably inside the domain. These trends are observed in the velocity vector plots (Figure 4.14 to Figure 4.16).

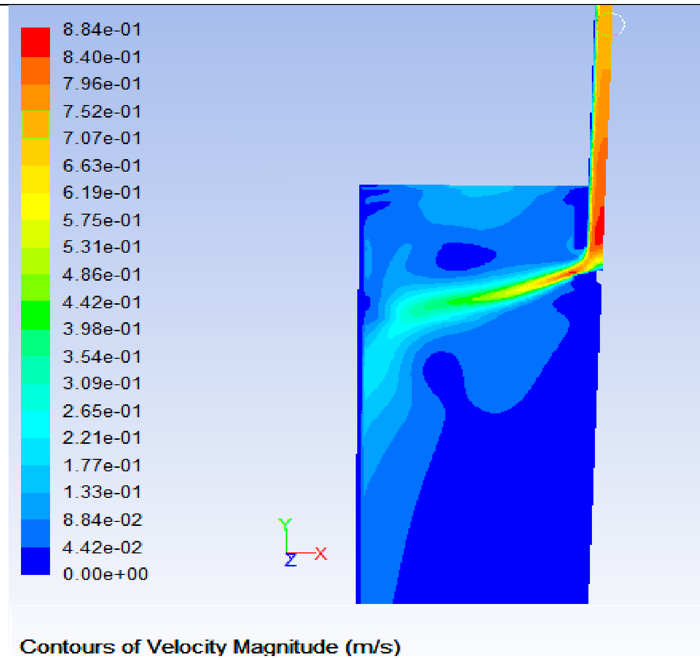

a) Without injection

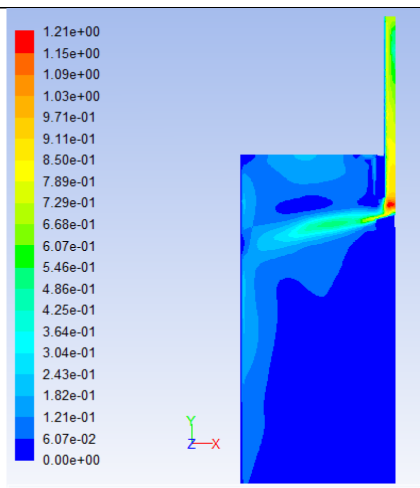

b) Q_{gas} = 2.5 lit/min, D_{bubble} =4 mm

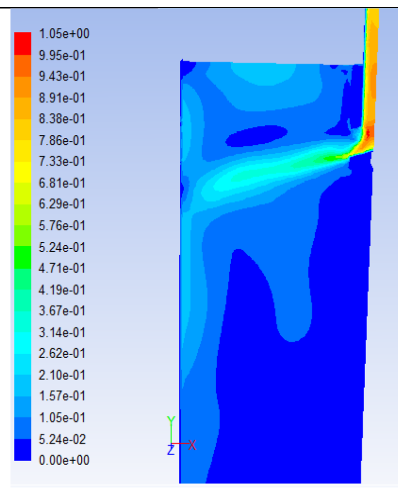

c) Q_{gas} = 2.5 lit/min, D_{bubble} =5 mm

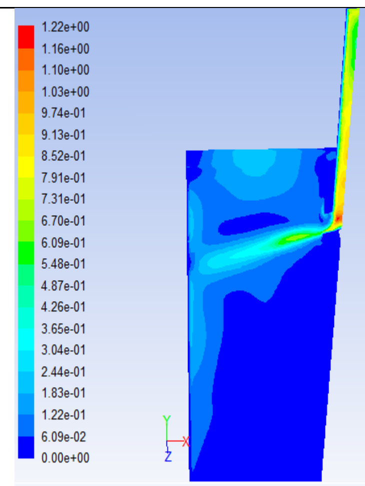

d) Q_{gas} = 2.5 LPM,D_{bubble}=6 mm

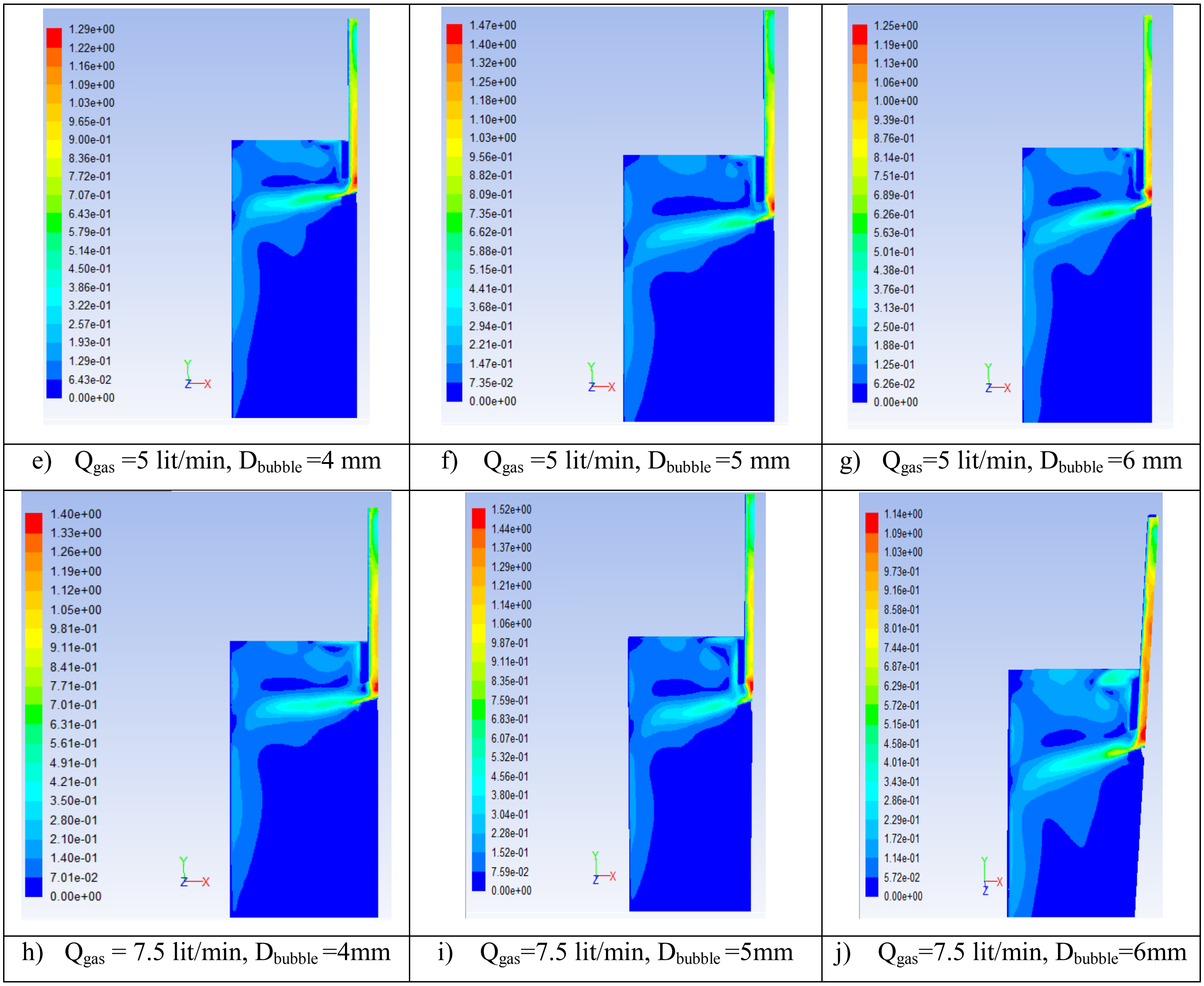

e) Q_{gas} =5 lit/min, D_{bubble} =4 mm

f) Q_{gas} =5 lit/min, D_{bubble} =5 mm

g) Q_{gas}=5 lit/min, D_{bubble} =6 mm

h) Q_{gas} = 7.5 lit/min, D_{bubble} =4mm

i) Q_{gas}=7.5 lit/min, D_{bubble} =5mm

j) Q_{gas}=7.5 lit/min, D_{bubble}=6mm

Figure 4.11: Velocity contours for a constant casting speed of 0.8 m/min and different injection conditions (color code: velocity in m/s)

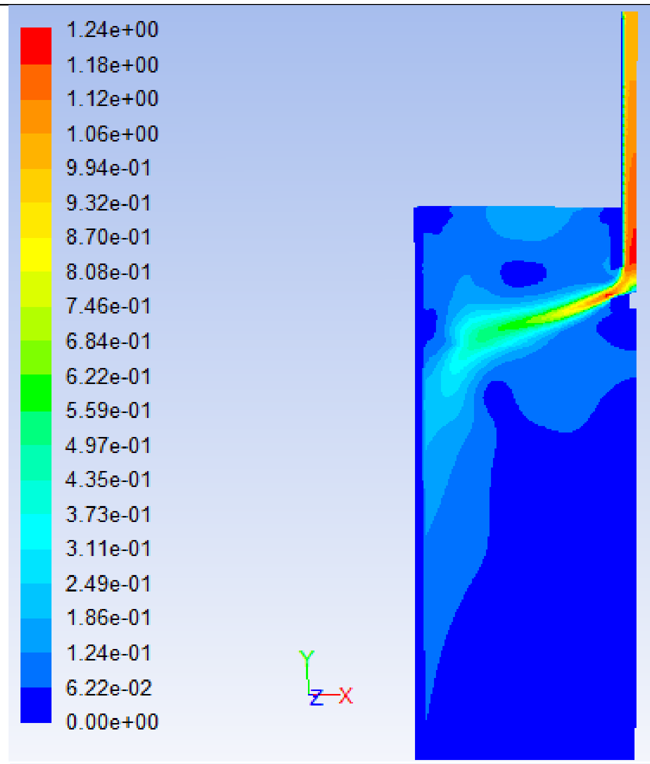

a) Without injection

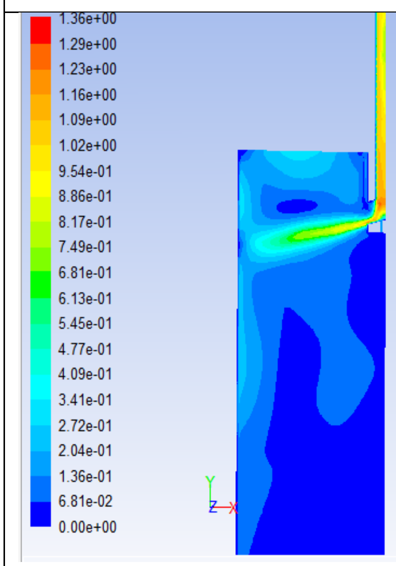

b) Q_{gas}=2.5 lit/min,D_{bubble} =4mm

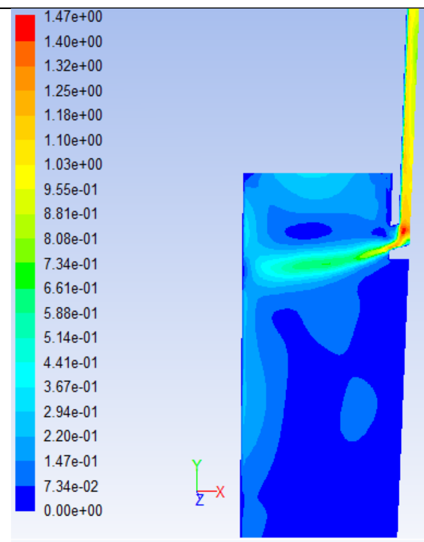

c) Q_{gas} = 2.5 lit/min, D_{bubble} =5 mm

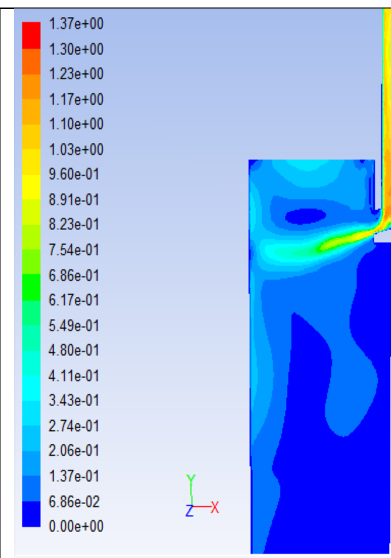

d) Q_{gas} = 2.5 lit/min, D_{bubble} =6 mm

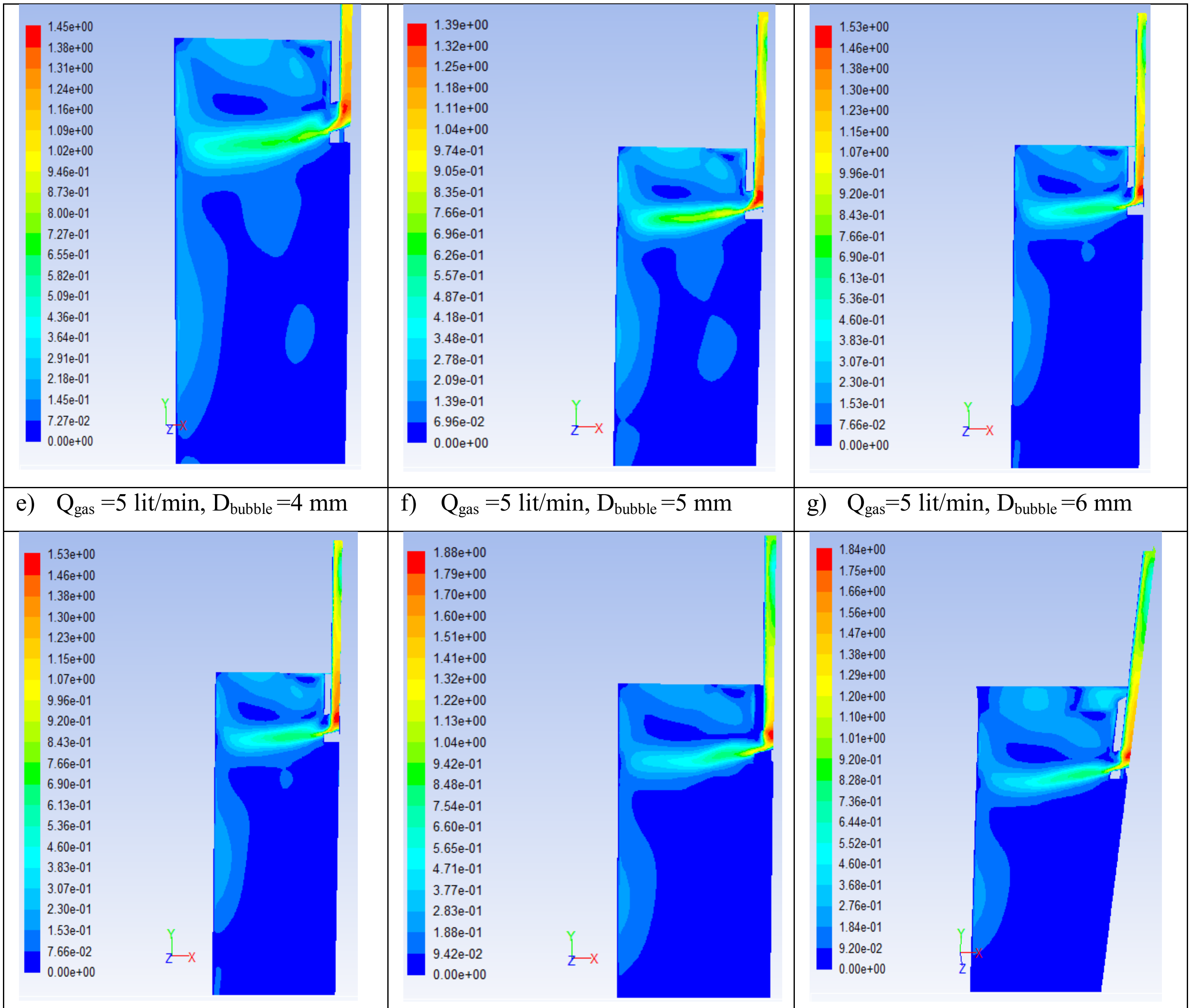

e) Q_{gas} =5 lit/min, D_{bubble} =4 mm

f) Q_{gas} =5 lit/min, D_{bubble} =5 mm

g) Q_{gas}=5 lit/min, D_{bubble} =6 mm

h) Q_{gas}=7.5 lit/min, D_{bubble} =4mm

i) Q_{gas}=7.5 lit/min, D_{bubble} =5mm

j) Q_{gas}=7.5 lit/min, D_{bubble}=6mm

Figure 4.12: Velocity contours for a contant casting speed of 1 m/min and different injection conditions (color code: velocity in m/s).

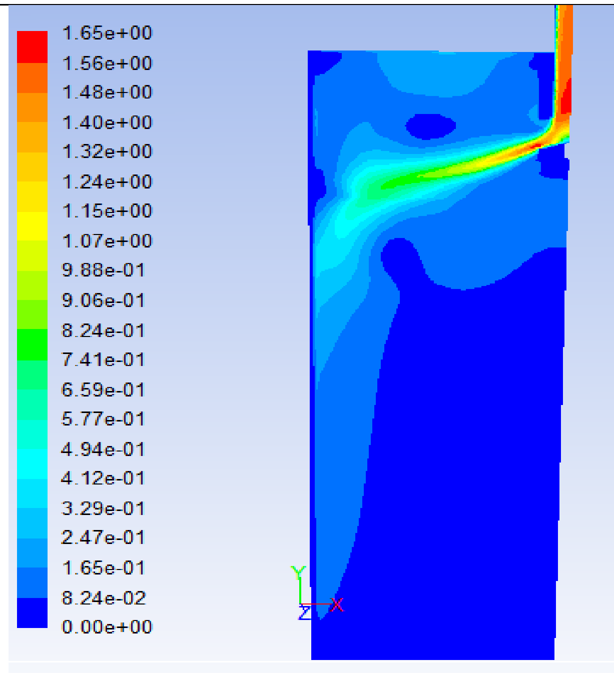

a) Without injection

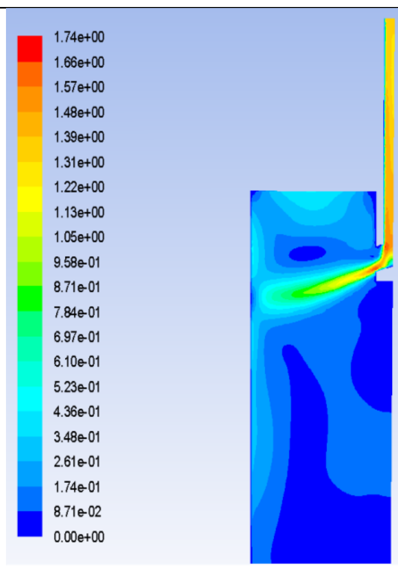

b) Q_{gas} = 2.5 lit/min, D_{bubble} =4 mm

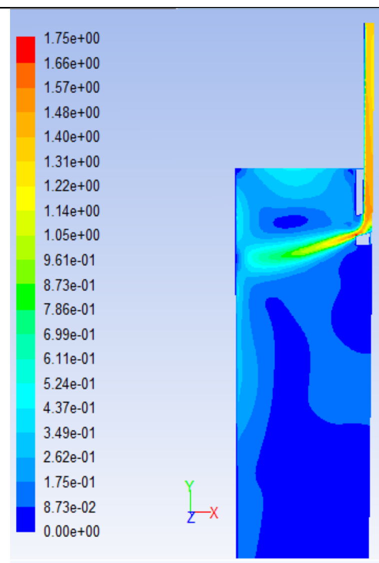

c) Q_{gas} = 2.5 lit/min, D_{bubble} =5 mm

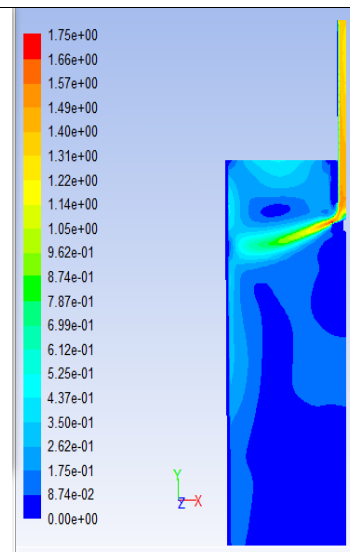

d) Q_{gas} = 2.5 lit/min, D_{bubble} =6 mm

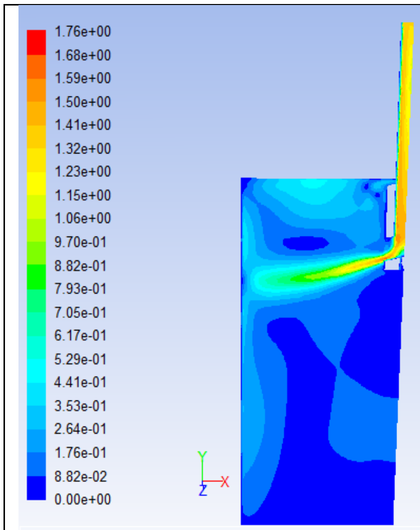	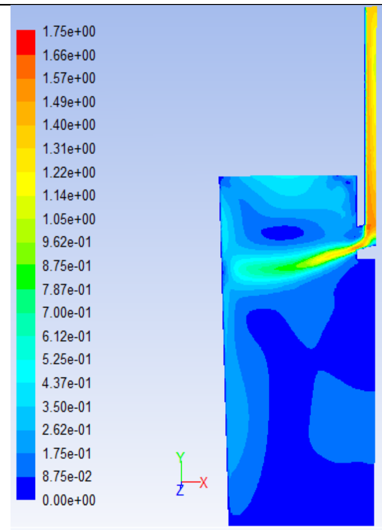	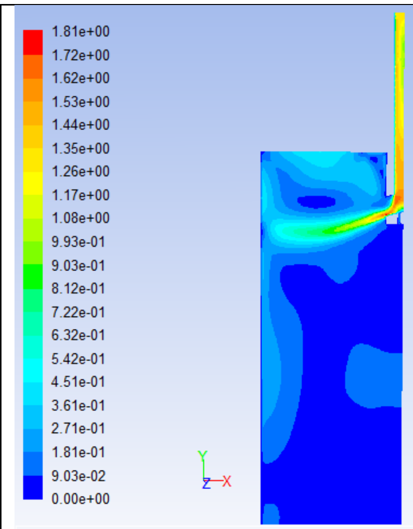
e) Q_{gas} =5 lit/min, D_{bubble} =4 mm	f) Q_{gas} =5 lit/min, D_{bubble} =5 mm	g) Q_{gas}=5 lit/min, D_{bubble} =6 mm
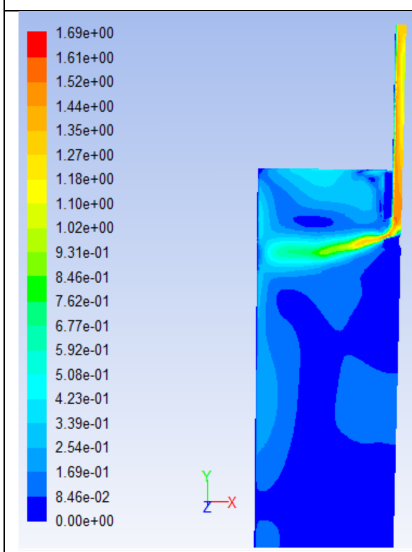	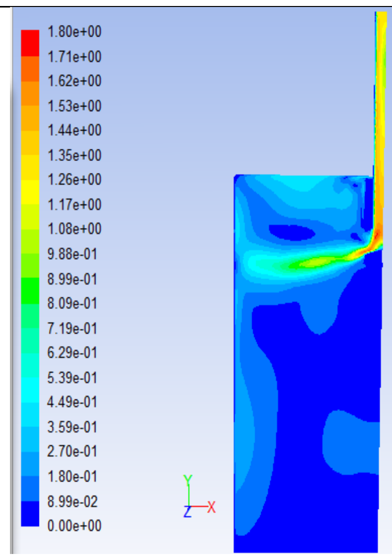	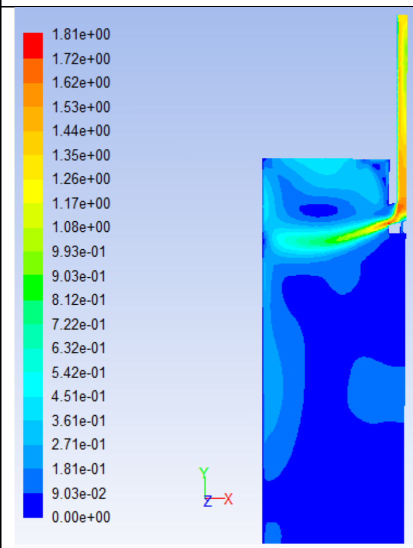
h) Q_{gas} = 7.5 lit/min, D_{bubble} =4mm	i) Q_{gas}=7.5 lit/min, D_{bubble} =5mm	j) Q_{gas}=7.5 lit/min, D_{bubble}=6mm

Figure 4.13: Velocity contours for casting speed 1.5 m/min and different injection conditions (color code: velocity in m/s).

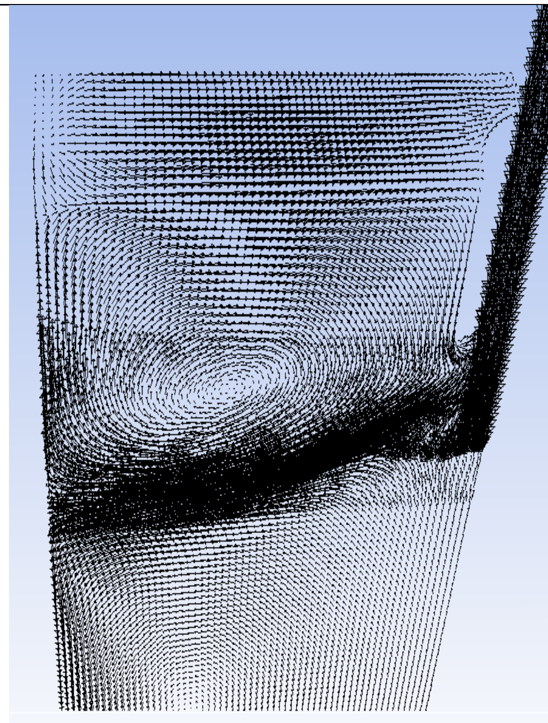

a) Without injection

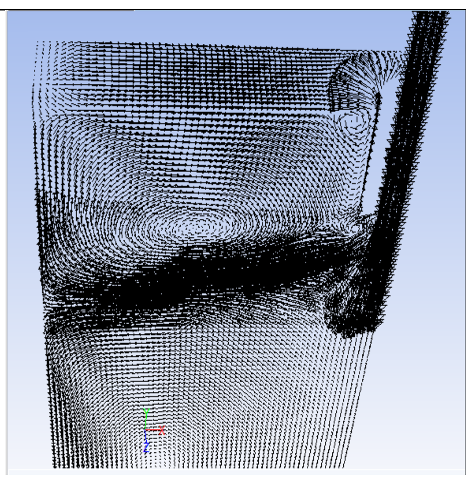

b) Q_{gas} = 2.5 lit/min, D_{bubble} =4 mm

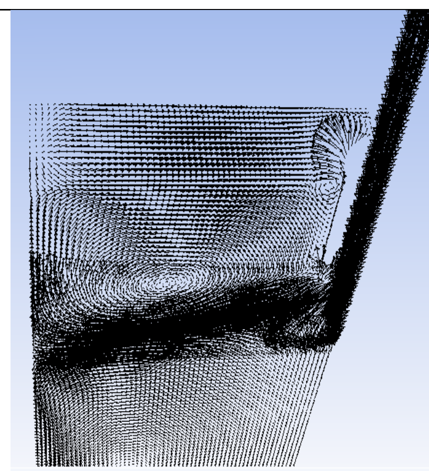

c) Q_{gas} = 2.5 lit/min, D_{bubble} =5 mm

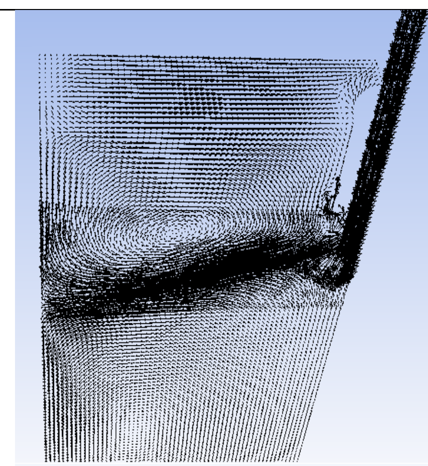

d) Q_{gas} = 2.5 lit/min, D_{bubble} =6 mm

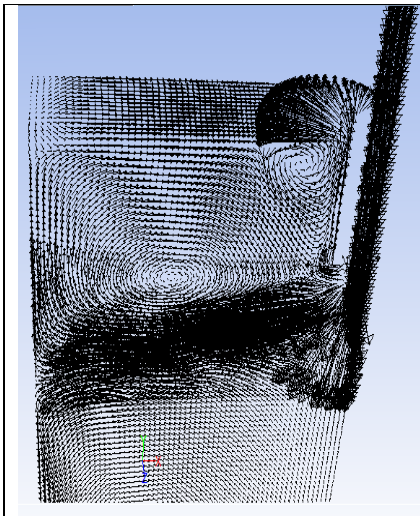	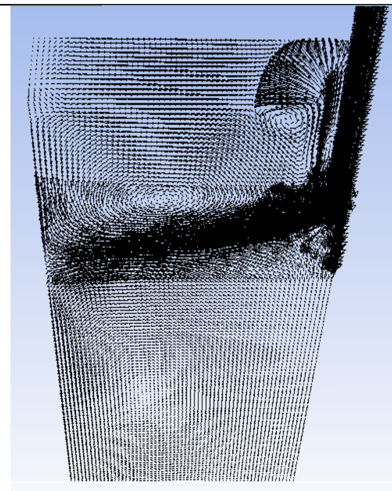	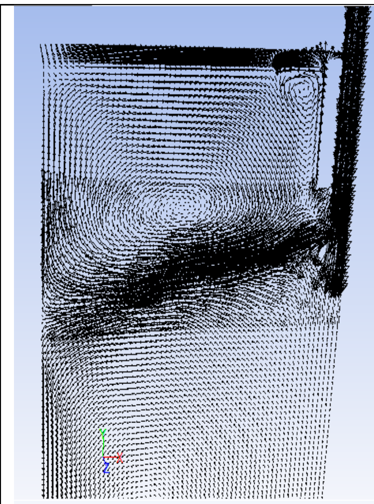
e) Q_{gas} =5 lit/min, D_{bubble} =4 mm	f) Q_{gas} =5 lit/min, D_{bubble} =5 mm	g) Q_{gas}=5 lit/min, D_{bubble} =6 mm
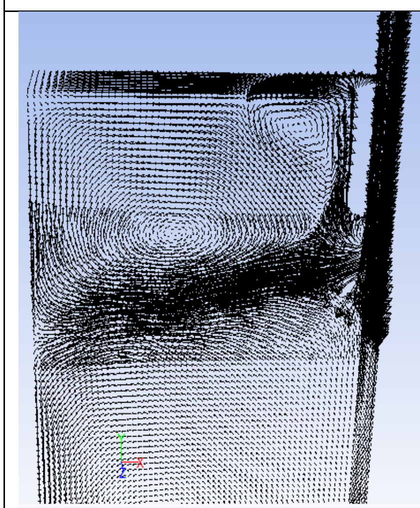	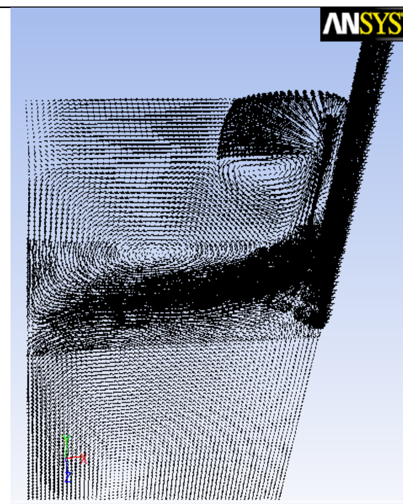	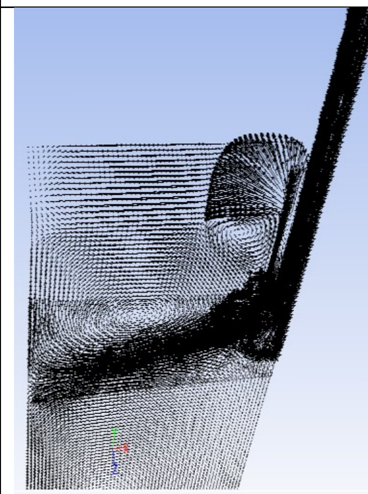
h) Q_{gas} = 7.5 lit/min, D_{bubble} =4mm	i) Q_{gas}=7.5 lit/min, D_{bubble} =5mm	j) Q_{gas}=7.5 lit/min, D_{bubble}=6mm

Figure 4.14: Velocity vector plots for casting speed 0.8 m/min and different injection conditions.

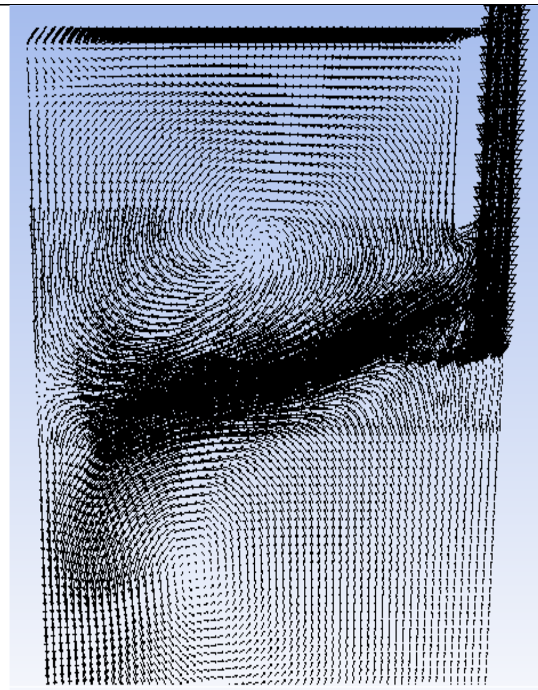

a) Without injection

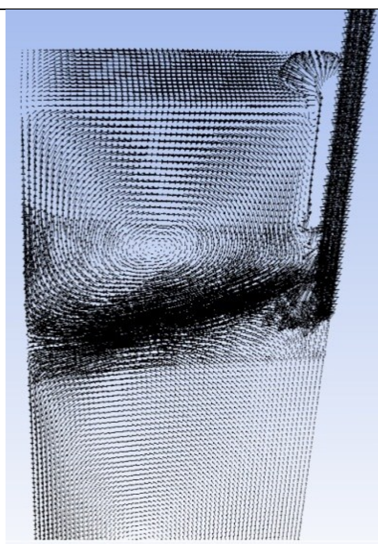

b) Q_{gas} = 2.5 lit/min, D_{bubble} =4 mm

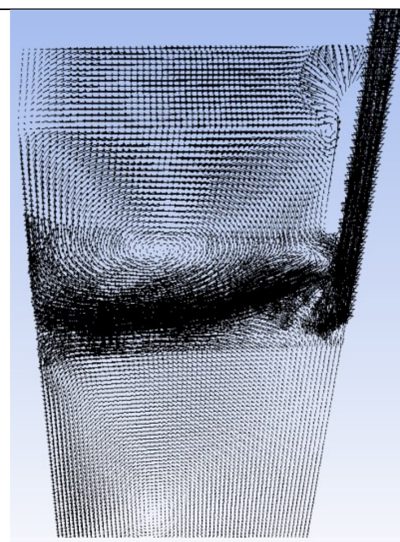

c) Q_{gas} = 2.5 lit/min, D_{bubble} =5 mm

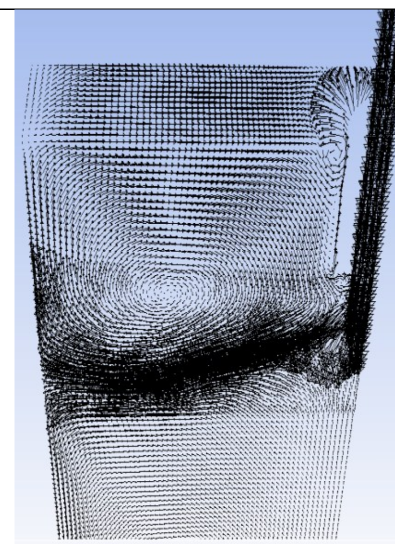

d) Q_{gas} =2.5 lit/min,D_{bubble}=6 mm

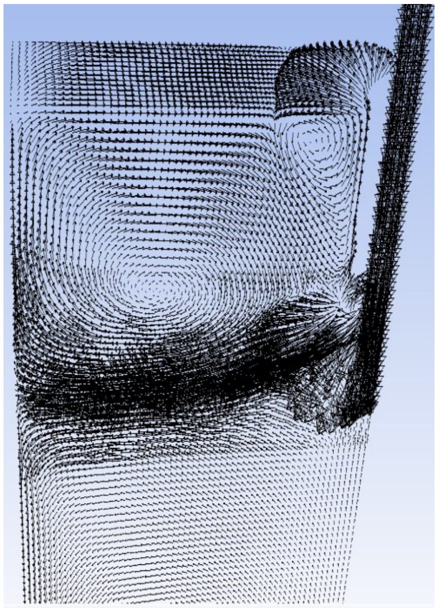	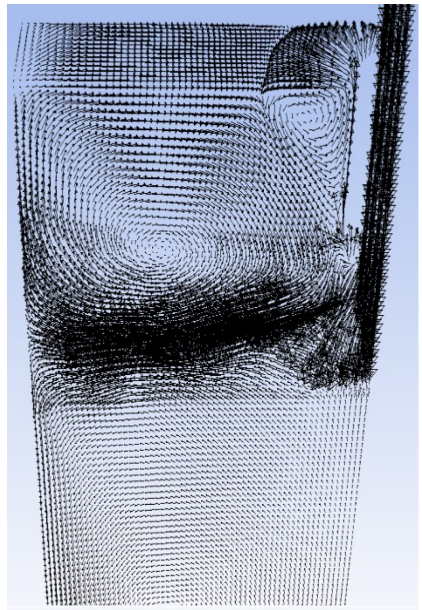	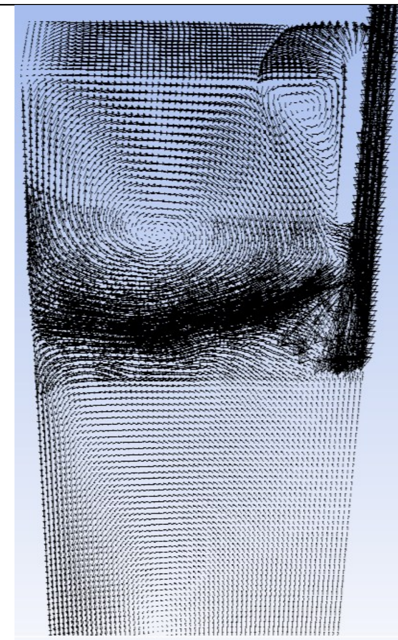
e) Q_{gas} =5 lit/min, D_{bubble} =4 mm	f) Q_{gas} =5 lit/min, D_{bubble} =5 mm	g) Q_{gas}=5 lit/min, D_{bubble} =6 mm
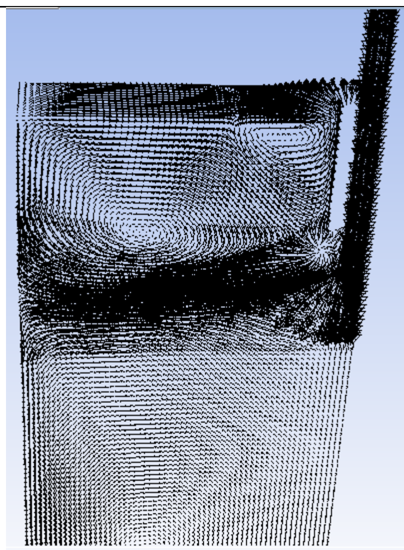	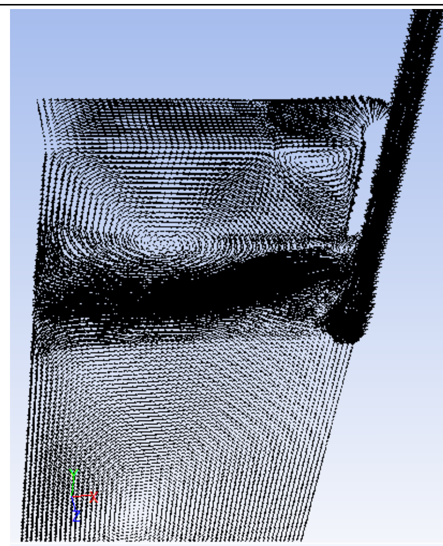	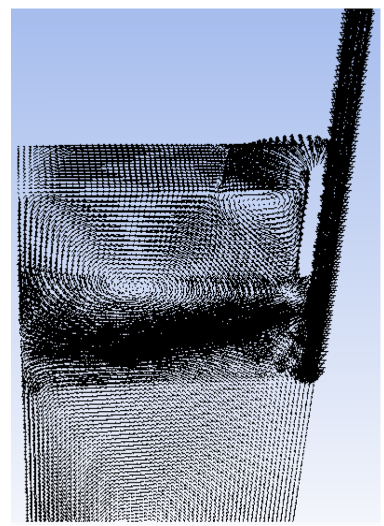
h) Q_{gas} = 7.5 lit/min, D_{bubble} =4mm	i) Q_{gas}=7.5 lit/min, D_{bubble} =5mm	j) Q_{gas}=7.5lit/min,D_{bubble}=6mm

Figure 4.15: Velocity vector plots for casting speed 1 m/min and different injection conditions.

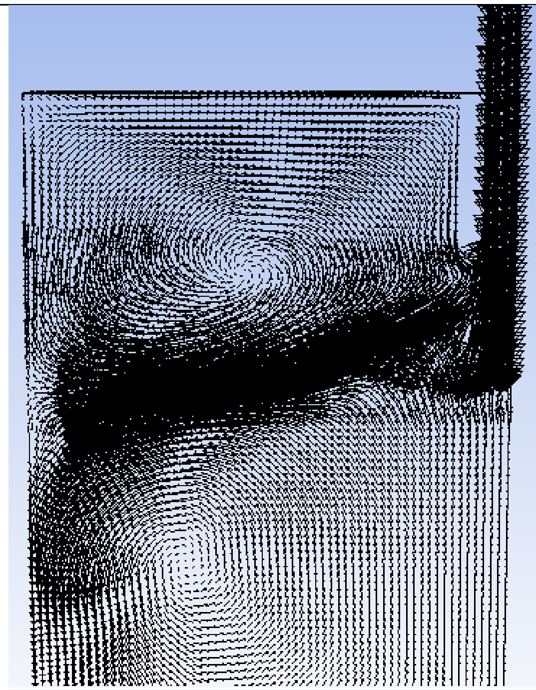

a) Without injection

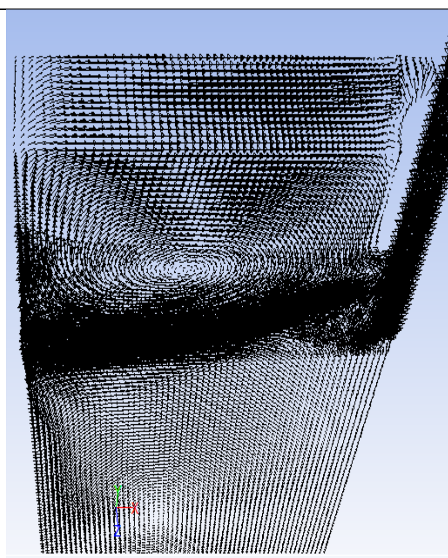

b) Q_{gas} = 2.5 lit/min, D_{bubble} =4 mm

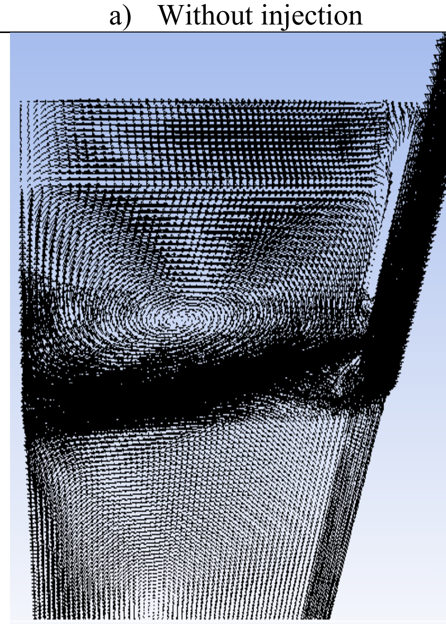

c) Q_{gas} = 2.5 lit/min, D_{bubble} =5 mm

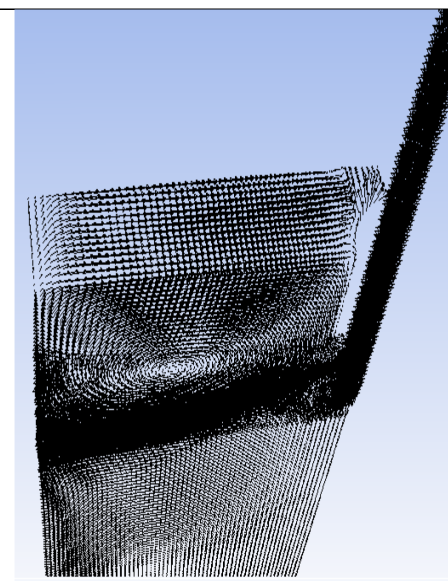

d) Q_{gas} = 2.5 lit/min, D_{bubble} =6 mm

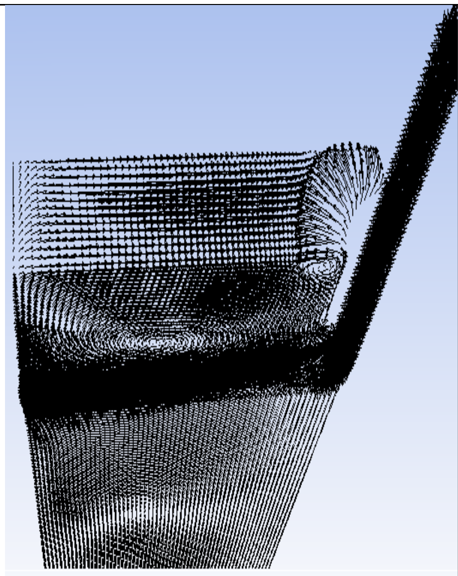	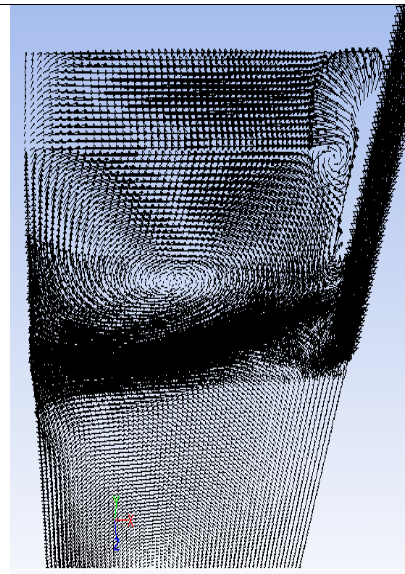	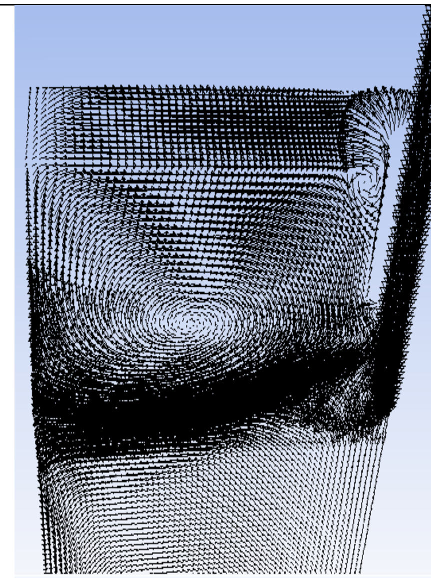
e) Q_{gas} =5 lit/min, D_{bubble} =4 mm	f) Q_{gas} =5 lit/min, D_{bubble} =5 mm	g) Q_{gas}=5 lit/min, D_{bubble} =6 mm
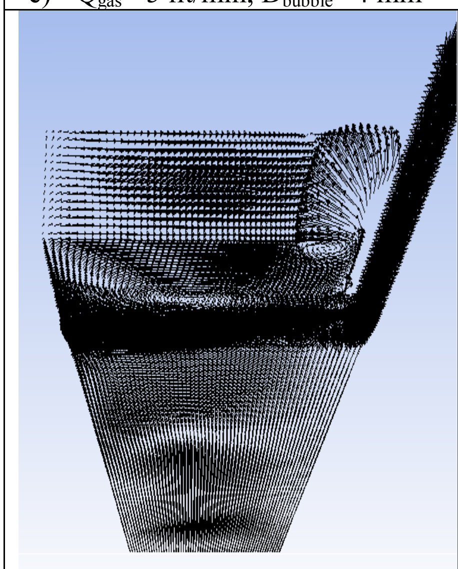	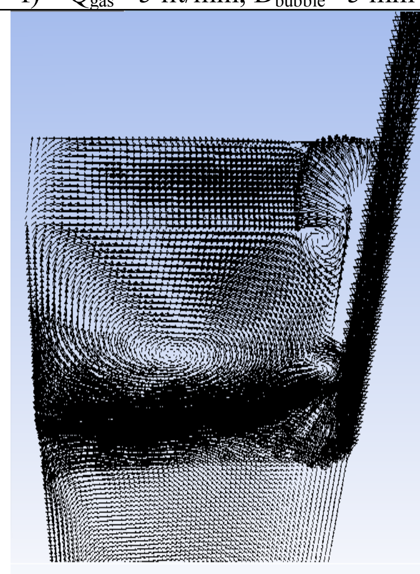	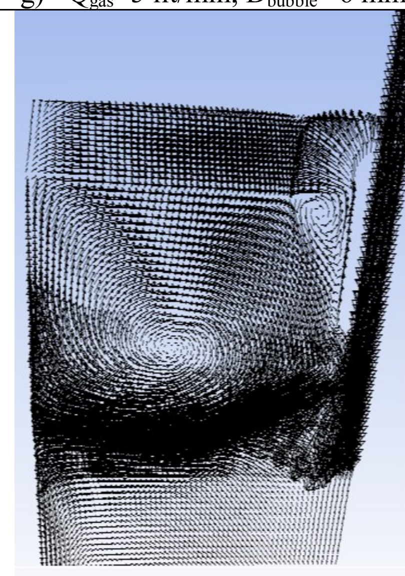
h) Q_{gas} = 7.5 lit/min, D_{bubble} =4mm	i) Q_{gas}=7.5 lit/min, D_{bubble} =5mm	j) Q_{gas}=7.5 lit/min, D_{bubble}=6mm

Figure 4.16: Velocity vector plots for casting speed 1.5 m/min and different injection conditions.

4.5 Superheat Dissipation Simulations

Thirty parametric cases, with and without argon injection, were simulated to determine the effects of different parameters on the temperature distribution inside the upper region of the mold. Single-phase temperature contours, highlight several cold spots at mold's corners and at the top area of narrow-face as seen in Figures 4.17 (a)-4.19 (a). Also, these figures indicate that the temperature increases in the top mold region with the casting speed.

This trend is altered by argon injection where relatively higher temperatures are predicted near SEN walls especially for the low casting speed of 0.8 m/min coupled with high injection rates, see Figure 4.17(b – j). This temperature rise is due to the strong influence of bubbles on the molten steel flow around SEN. By increasing the casting speed from 0.8 m/min to 1.1 m/min, this influence is reduced especially for the low argon flow rates of 2.5 LPM. However, the influence of bubbles is more-dominant around SEN for the high argon flow rate of 7.5 LPM, as seen in Figures 4.18 (h-j). Moreover, for a relatively higher casting speed of 1.5 m/min, the influence of injection flow rate is reduced around SEN; see Figure 4.19 (b-j), due to the deeper penetration of bubbles inside the mold. Also, argon injection reduces the size of the cold spots located in the mold's corners. Moreover, small bubbles generally have more influence on a relatively larger area due to its wider spread within domain.

The temperature contours, Figure 4.19 (e-j), show relatively higher temperatures within the top recirculation zone in the case of high casting speed of 1.5 m/min and injection rate of 7.5 LPM. This desirable behavior, for the fast removal of superheat, is possibly due to the lift experienced by the molten steel jet.

The temperature profiles, Figures 4.20-4.22, indicate a gradual increase from a minimum value at the narrow face to a relatively higher temperature near SEN. In addition, the temperature profiles for the low casting speed of 0.8 m/min, see Figure 4.20, indicate sharp temperature rise near SEN which match the locations of secondary peaks shown in previous Section (4.2.1).

In addition, the temperature difference, between mono-phase and two-phase profiles of the casting speed of 0.8 m/min, around SEN increases from 1° C to 2.5° C for the injection rate range of 2.5 to 7.5 lit/min, respectively. Also, the corresponding distance, away from SEN, covered by this temperature difference increases from 0.15 m to 0.25 m with injection rate increment from 2.5 lit/min to 7.5 lit/min, respectively.

Moreover, the temperature difference decreases in the case of high casting speed of 1.5 m/min due to the lower influence of injection on the heat-transfer around SEN. In fact, the temperature profiles of mono-phase and two-phase overlap for a casting speed of 1.5 m/min as seen in Figure 4.22.

DPM simulations indicate that argon injection can possibly speed up superheat dissipation if controlled properly. This desired influence is obtained by the precise correlation of the argon flow rate to the casting speed to obtain the optimum performance.

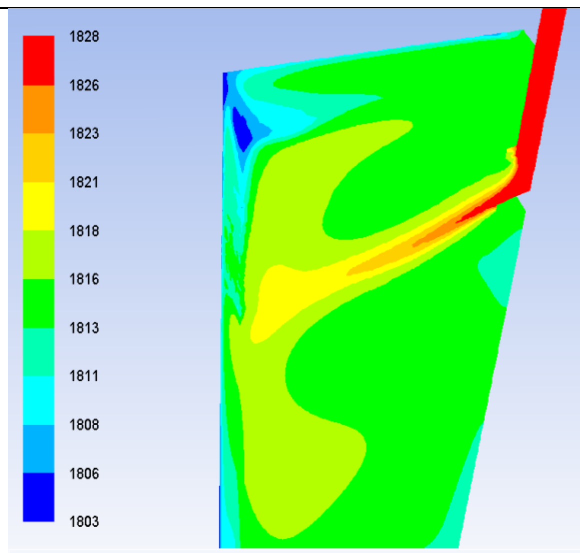

a) Without injection

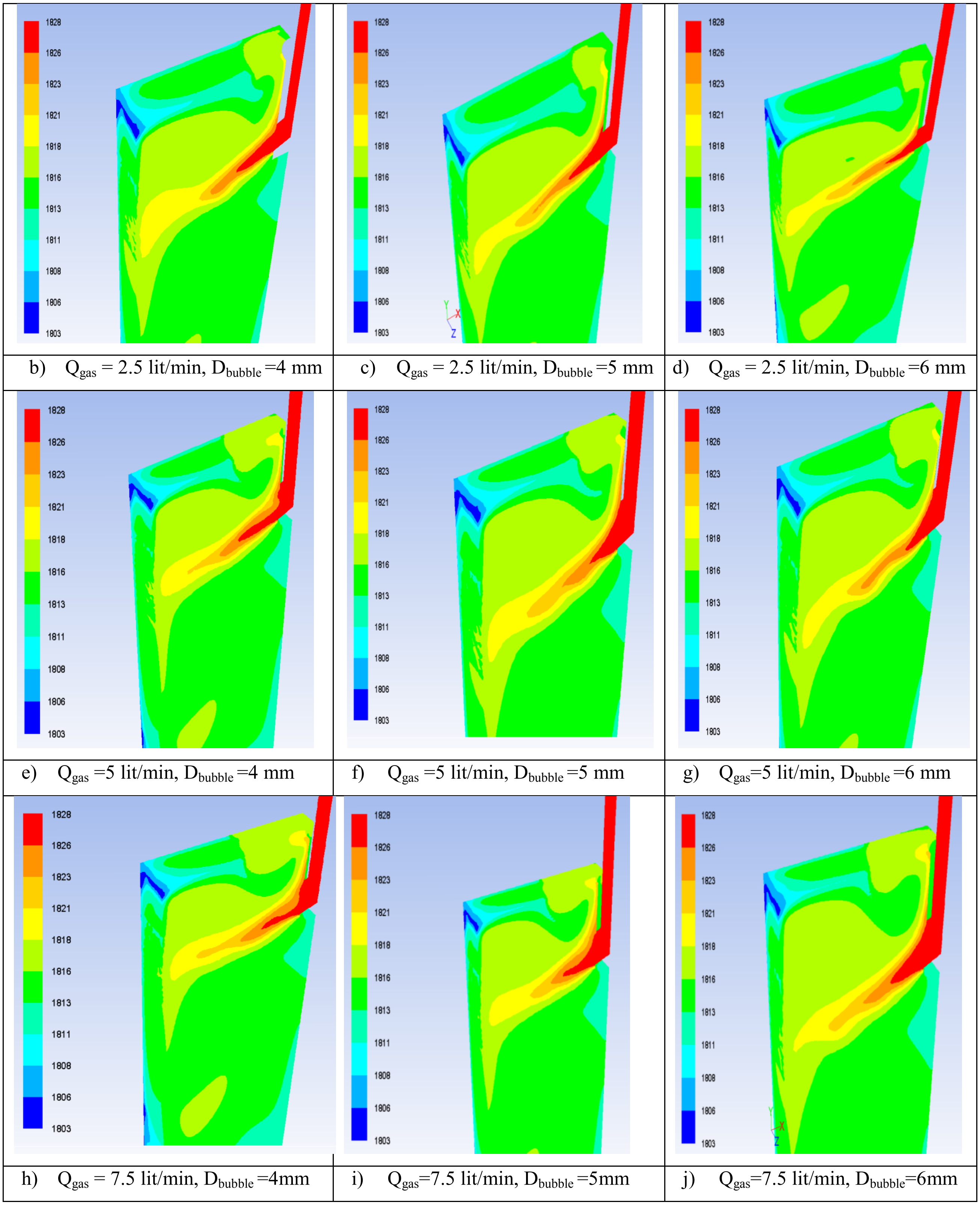

b) Q_{gas} = 2.5 lit/min, D_{bubble} =4 mm | c) Q_{gas} = 2.5 lit/min, D_{bubble} =5 mm | d) Q_{gas} = 2.5 lit/min, D_{bubble} =6 mm

e) Q_{gas} =5 lit/min, D_{bubble} =4 mm | f) Q_{gas} =5 lit/min, D_{bubble} =5 mm | g) Q_{gas}=5 lit/min, D_{bubble} =6 mm

h) Q_{gas} = 7.5 lit/min, D_{bubble} =4mm | i) Q_{gas}=7.5 lit/min, D_{bubble} =5mm | j) Q_{gas}=7.5 lit/min, D_{bubble}=6mm

Figure 4.17: Temperature contours for a constant casting speed of 0.8 m/min and different injection conditions (color code: temperature in Kelvin).

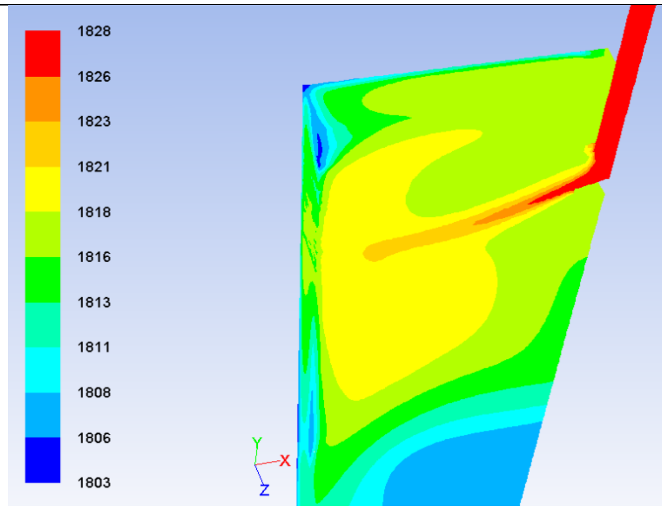

a) Without injection

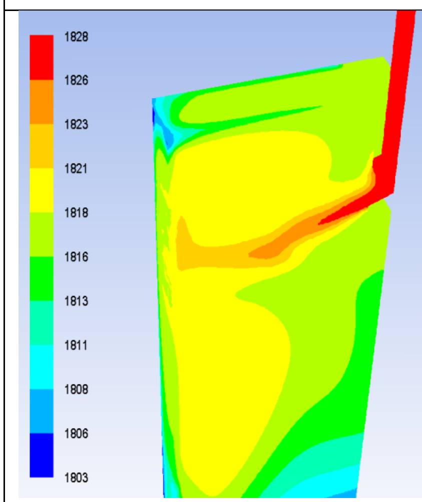

b) Q_{gas} = 2.5 lit/min, D_{bubble} =4 mm

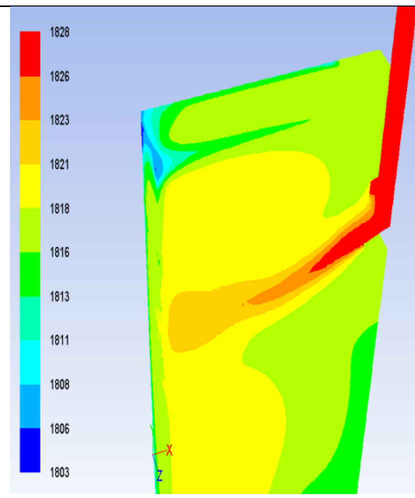

c) Q_{gas} = 2.5 lit/min, D_{bubble} =5 mm

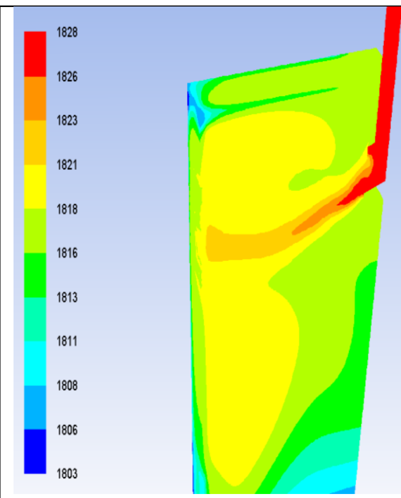

d) Q_{gas} = 2.5 lit/min, D_{bubble} =6 mm

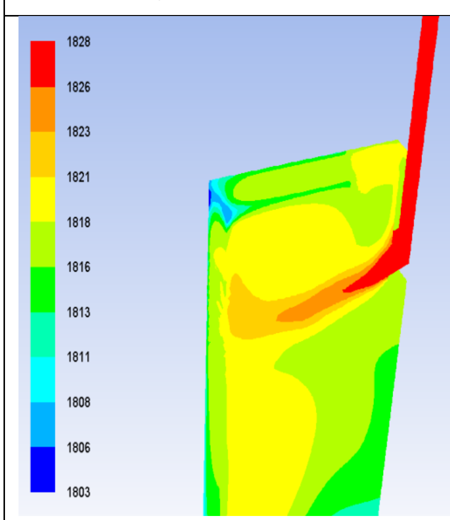

e) Q_{gas} =5 lit/min, D_{bubble} =4 mm

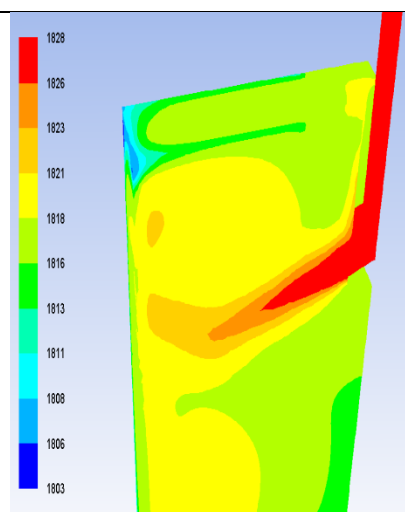

f) Q_{gas} =5 lit/min, D_{bubble} =5 mm

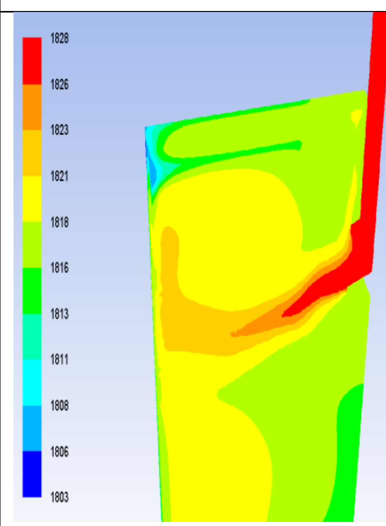

g) Q_{gas}=5 lit/min, D_{bubble} =6 mm

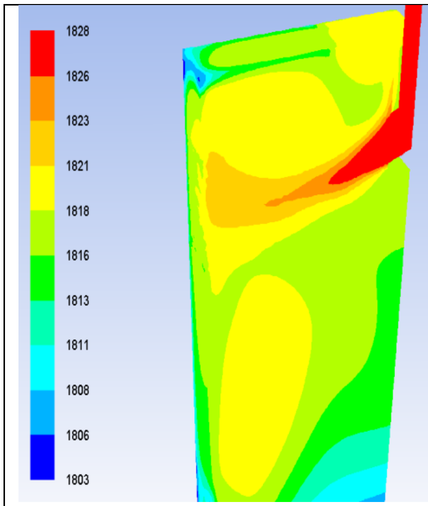

h) Q_{gas} = 7.5 lit/min, D_{bubble} =4mm

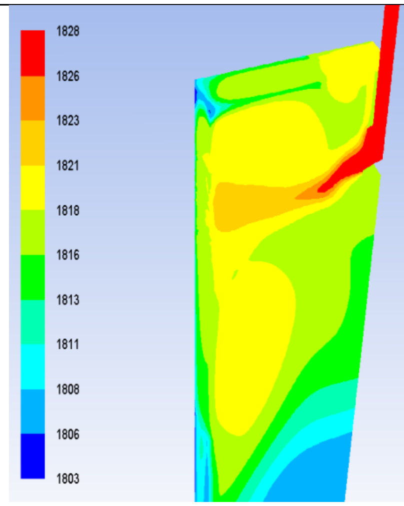

i) Q_{gas}=7.5 lit/min, D_{bubble} =5mm

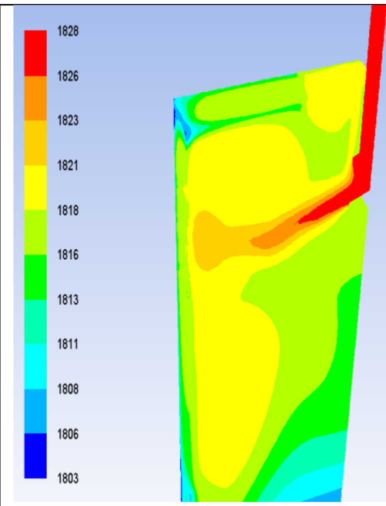

j) Q_{gas}=7.5 lit/min, D_{bubble}=6mm

Figure 4.18: Temperature contours for a constant casting speed of 1.1 m/min and different argon injection conditions (color code: temperature in Kelvin).

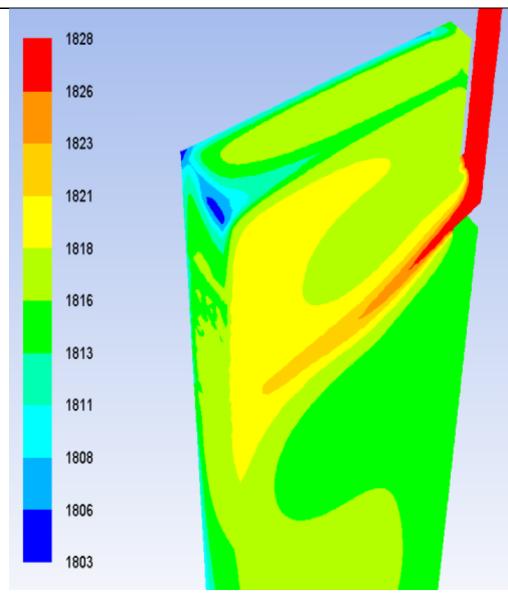

a) Without injection

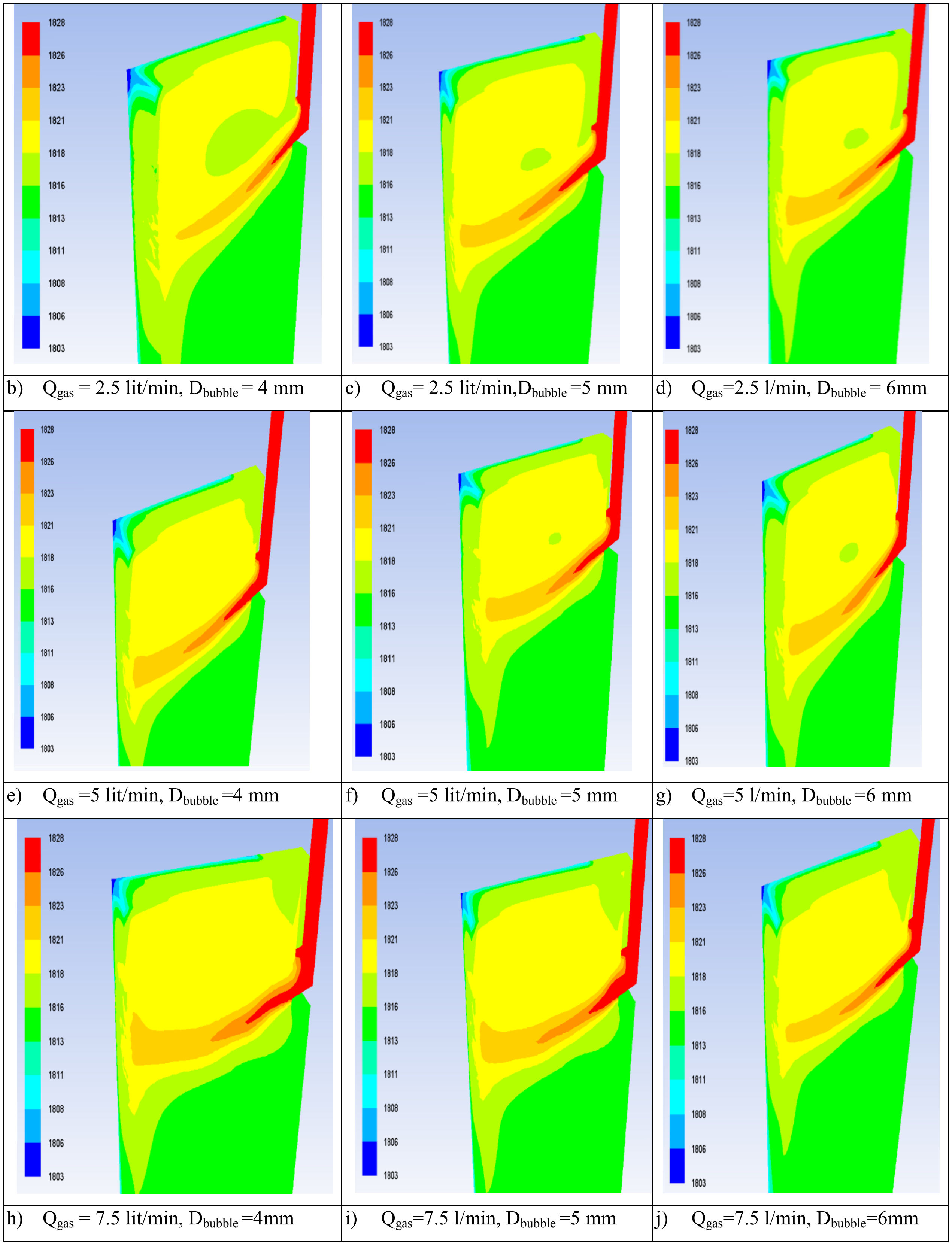

Figure 4.19: Temperature contours for a constant casting speed of 1.5 m/min and different injection conditions (color code: temperature in Kelvin).

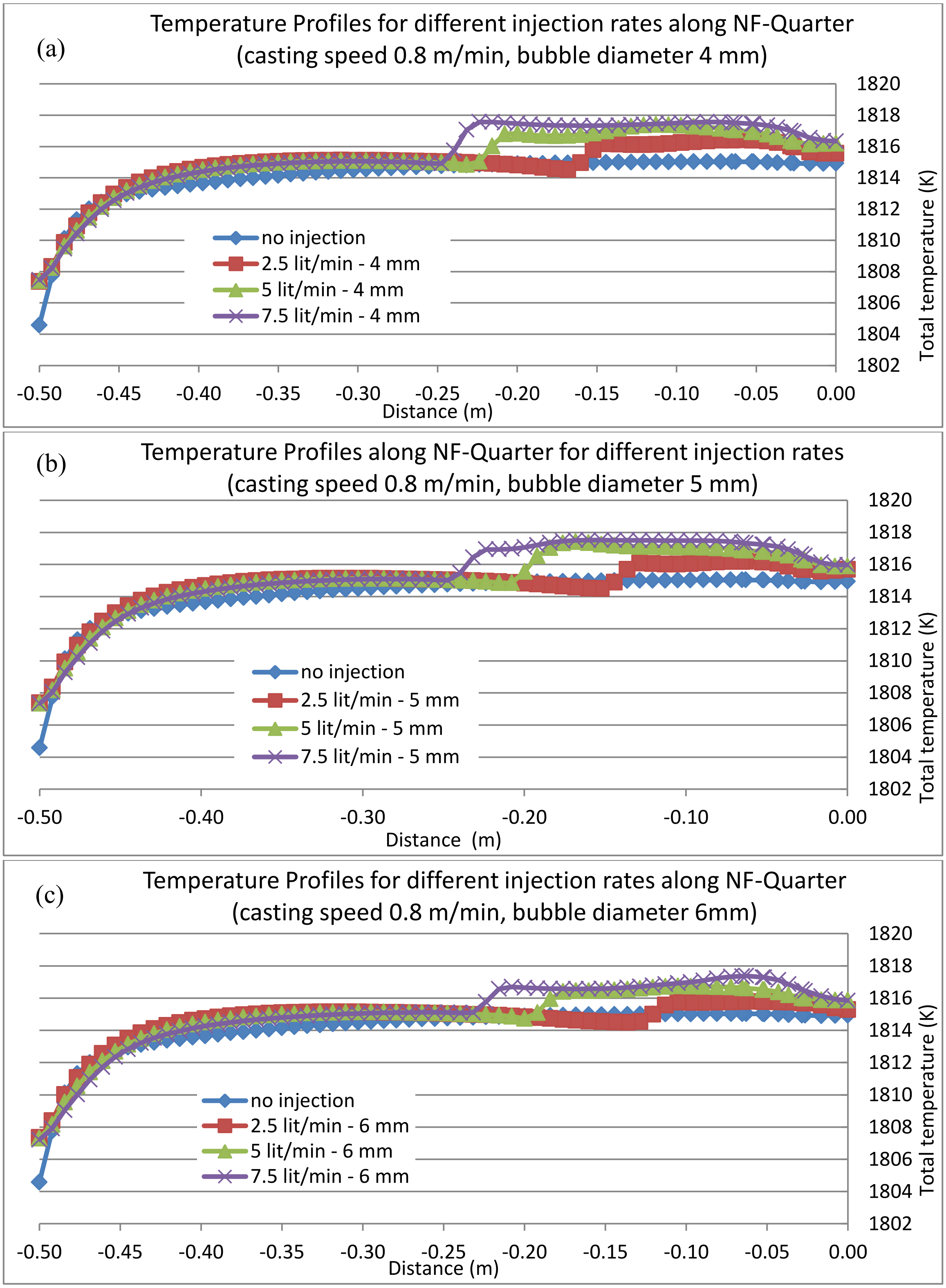

Figure 4.20: Effects of injection rates on temperature profiles, along the symmetry plane, for a constant casting speed of 0.8 m/min and different bubble diameters: (a) 4 mm, (b) 5 mm, (c) 6 mm.

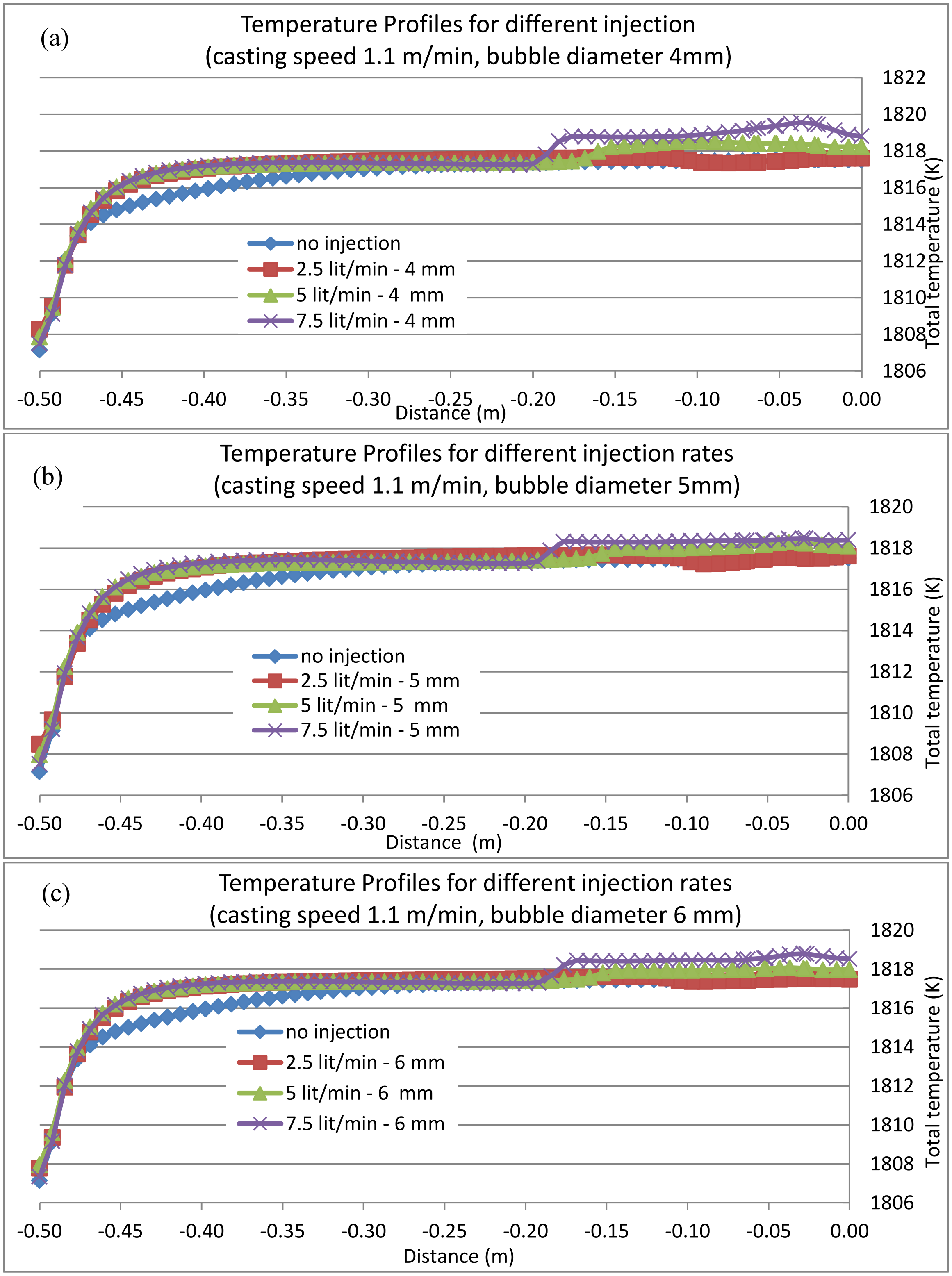

Figure 4.21: Effects of injection rates on temperature profiles, along the symmetry plane, for a constant casting speed of 1.1 m/min and different bubble diameters: (a) 4 mm, (b) 5 mm, (c) 6 mm.

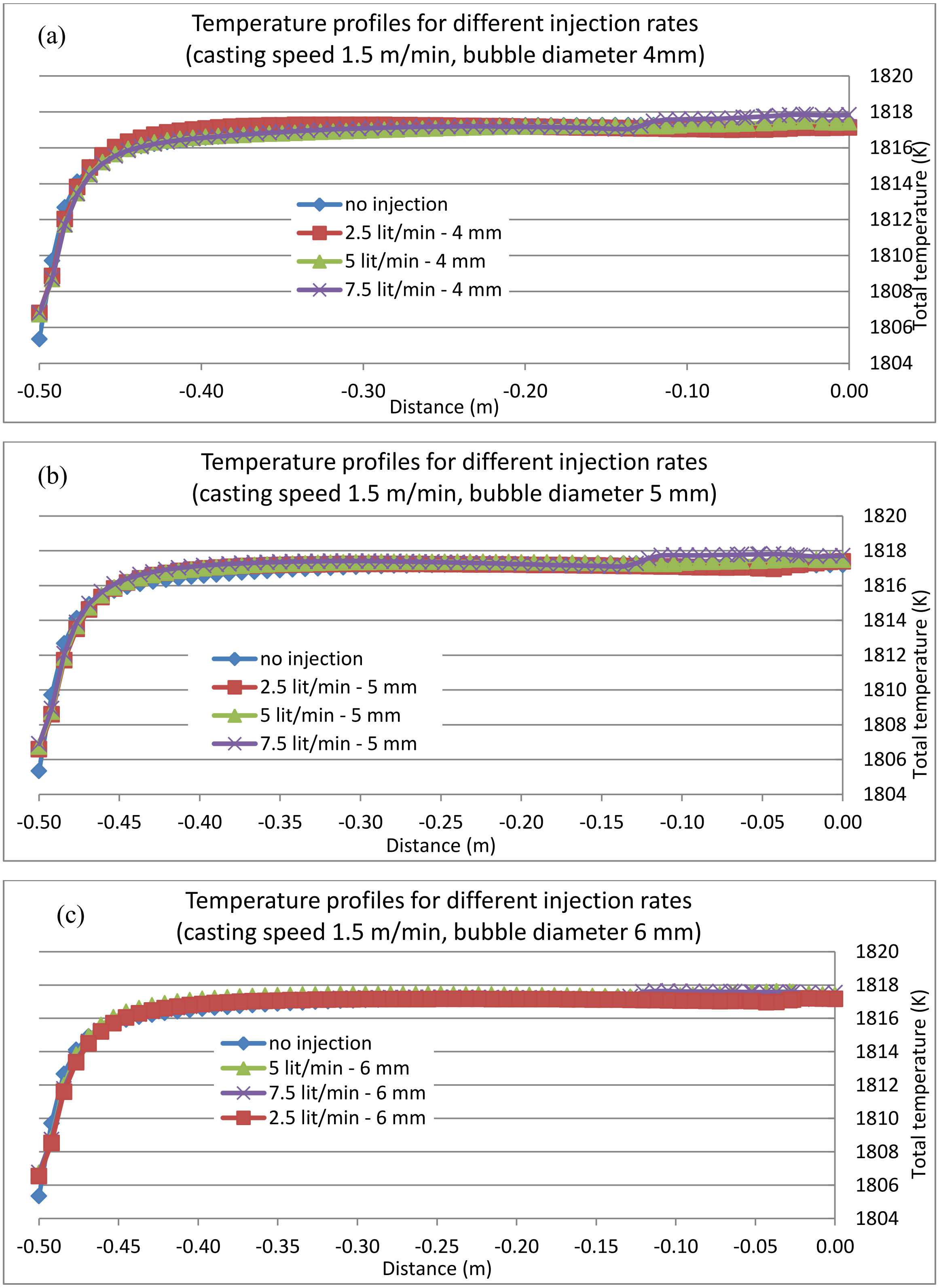

Figure 4.22: Effects of injection rates on temperature profiles, along the symmetry plane, for a constant casting speed of 1.5 m/min and different bubble diameters: (a) 4 mm, (b) 5 mm, (c) 6 mm.

Chapter 5: Conclusions

A 3D CFD-DPM model can provide some guidelines on the velocity and temperature fields in such harsh and opaque systems. The present 3D CFD-DPM study is an attempt to model the multi-phase flow patterns and heat transfer dissipation rates in the mold region of a specific continuous caster for various argon injection rates in the mold under different casting conditions.

The present CFD-DPM simulations have shown the potential of approximating molten steel-argon gas two-phase flow pattern. Simulations with DPM predict that gas injection effects on steel flow vary and are dependent on casting speeds and injection flow rates. Also, the formation of the two velocity peaks, which depend on the casting speed and the injection rate, under the slag layer was not studied thoroughly by previous researchers in this area. Although the presence of the slag layer will surely dampens these peaks physically, but the velocity peaks magnitudes can be used to develop slag entrainment mechanistic studies.

Also, the temperature distribution at the upper region of the mold varies with the casting speeds and the injection parameters. Simulations indicate that argon injection optimization, to correspond to a specific casting speed, is critical to obtain the desired criteria of fast removal of superheat and mitigation of cold spots.

In this research, a total of sixty 3D turbulent two-phase flow simulation runs were carried out by varying the casting speed, the gas injection and the bubble size to arrive at the conclusions stated above.

References

1	M. Wolf. "History of Continuous Casting", *75th Steelmaking Conference Proceedings*, Iron & Steel Society, 1992, pp. 83-137.
2	H.F. Schrewe. *Continuous Casting of Steel, Fundamental Principles and Practice*. Dusseldorf, Germany: Stahl und Eisen, 1991.
3	A. Cramb, ed. *The Making, Shaping, and Treating of Steel: Casting*, Pittsburgh, PA: AISI Engineers, 2001.
4	W.R. Irving. *Continuous Casting of Steel*, London, UK: Carlton House Terrace, 1993, pp.1-206.
5	B.G. Thomas. “Continuous Casting,” The Encyclopedia of Materials: Science and Technology: Elsevier Science Ltd., UK, Vol. 2, 2001, pp. 1595-1599.
6	R. Guthrie and M. Isaac. “Chapter 4: Continuous Casting”, *in Advanced Steel Making Handout*, to be published, pp. 1-50.
7	Y. Sahai and T. Emi, *Tundish technology for clean steel production.* NJ: World Scientific, 2008.
8	K. Tanizawa, F. Yamaguchi, K. Inaoka, and K. Tanaka. “Influence of the Steelmaking Conditions on Nonmetallic Inclusions and Product Defects”, *Metallurgia Italiana* , Vol. 84, 1992, pp. 17-22.
9	J. Farrell, P. Bilek, and D. Hilty. "Inclusions Originating from Reoxidation of Steel", *28th AIME Electric Furnace Conference Proceedings*, 1970, pp. 64-88.
10	J. Svoboda, R. W. Monroe, C. Bates and J. Griffin. "Appearance and Composition of Macro-inclusions in Steel Castings", *AFS Transactions*, 1987, pp. 187- 202.
11	A.S. Venkatadri. "Mechanism of Formation of Non-metallic Inclusions in Aluminum-killed Steel", *Transaction ISIJ*, Vol. 18, 1978, pp. 591-600.
12	M. Schmidt, T. Russo, and D. Bederka. “Steel Shrouding and Tundish Flow Control to Improve Cleanliness and Reduce Plugging”, *73rd ISS Steelmaking Conference*, 1991, pp. 3-12.

13	S. N. Singh. “Mechanism of Alumina Buildup in Tundish Nozzles During Continuous Casting of Aluminum-Killed Steels”, *Metallurgical Transactions*, Vol. 5, 1974, pp. 2165-2178.
14	S. Ogibayashi et. al., “Mechanism and Countermeasure of Alumina Buildup on Submerged Nozzle in Continuous Casting”, *Taikabutsu Overseas*, Vol. 15 [1], 1994, pp. 3-14.
15	F. Kemeny, "Tundish Nozzle Clogging - Measurement and Prevention", *McLean Symposium Proceedings*, ISS, Warrendale, PA, 1998, pp. 103-110.
16	S. Li, W. Jin, L. Zhang, X. Zuo and Y. Wang. "Inclusions and Nozzle Clogging during Steel Continuous Casting Process", *AISTech Proceedings*, Vol.2, 2008, pp.899-913.
17	K. Rackers and B.G. Thomas. "Clogging in Continuous Casting Nozzles", *78th Steelmaking Conference Proceedings*, Vol. 78, 1995, pp. 723-734.
18	M. Byrne, T. W. Fenicle, and A. W. Cramb. “The Sources of Exogenous Inclusions in Continuous Cast, Aluminum-Killed Steels”, *ISS Transactions*, Vol. 10, 1989, pp. 51-60.
19	Y. Fukuda, Y. Ueshima, and S. Mizoguchi. "Mechanism of alumina deposition on alumina graphite immersion nozzle in continuous caster", *ISIJ International*, Vol. 32 [1], 1992, pp.164-168.
20	J. Szekely and S. Dinovo. “Thermal Criteria for Tundish Nozzle or Taphole Blockage”, *Metallurgical Transactions*, Vol. 5, 1974, pp. 747-754.
21	K. Sasai and Y. Mizukami. "Reaction mechanism between alumina graphite immersion nozzle and low carbon steel", *ISIJ International*, Vol. 34 [10], 1994, pp.802- 809.
22	Y. Vermeulen, B. Coletti, and P. Wollants. “Clogging in submerged entry nozzles”, *Steel Research*, Vol. 71[10], 2000, pp.391-395.
23	B.G. Thomas and H. Bai. “Tundish nozzle clogging-application of computational models”, *18th Process Technology Division Conference Proceedings*, 2001, pp. 895-912.
24	J. Bourguignon, J. Dixmier, and J. Henry. “Different Types of Calcium Treatment as Contribution to Development of Continuous Casting Process”, *85th Continuous Casting*, 1985, pp. 22-24.
25	B. Bergmann, N. Bannenberg, and R. Piepenbrock. “Castability Assurance of Al-Killed Si-Free Steel by Calcium Cored Wire Treatment”, *1st European Conference on*

	Continuous Casting, 1991, pp. 1501-1508.
26	R. Dekkers. "Chapter 9: Submerged Entry Nozzle Clogging", Ph.D. dissertation, Katholieke Universiteit, Leuven, Belgium, 2002.
27	L. Trueba, K.D. Peaslee and J. Smith. "Simulation of Nozzle Clogging During the Continuous Casting of Aluminum-Killed Steel", *84th Steelmaking Conference Proceedings, Iron and Steel Society/AIME*, 2001, pp. 913-924.
28	R. Tuttle, K. Peaslee, and J. Smith. "Casting Simulation of Calcium Titanate and Calcium Zirconate Nozzles for Continuous Casting of Aluminum-Killed Steels", *Metallurgical and Materials Transactions B*, Vol. 38 [1], 2007, pp.101-108.
29	E. Marino. "Use of Calcium Oxide as Refractory Material in Steel Making Processes" in Refractories for the Steel Industry, R. Amavis, Ed. New York: Elsevier Applied Science Publishers, 1990, pp. 59-68.
30	T. Aoki, T. Nakamura, H. Ozeki and A. Elksnitis. "Alumina Clogging Resistant Materials for Tundish Shrouds", *78th Steelmaking Conference Proceedings*, 1991, pp. 357-360.
31	P. Benson, Q. Robinson, and H. Park. "Evaluation of Lime-Containing Sub-Entry Shroud Liners to Prevent Alumina Clogging", *76th ISS Ironmaking and Steelmaking Conference*, 1993, pp. 533–539.
32	Y. Aiba, K. Oki, M. Sugie, K. Kurihara, and T. Maeda. "Study of Corrosion and Penetration of Zirconia Refractories by Molten Steel and Slag", *Taikabutsu Overseas*, Vol. 5[1], 1985, pp. 3-11.
33	Y. Chung and S. Kim. "Mechanism of Slagline Wear of Graphite-Containing Zirconia Submerged Nozzles during Continuous Casting", *Journal Korean Institute of Metals and Materials*, Vol. 28[1], 1990, pp. 49-58.

34	A. Dick, X. Yu, R. Pomfret and K. Coley. “Attack of Submerged Entry Nozzles by Mould Flux and Dissolution of Refractory Oxides in the Flux”, *ISIJ International*, Vol. 37 [2], 1997, pp. 102-108.
35	E. Heikkinen, R. Mattila, T. Kokkonen, J. Harkki, and E. Mannisto. “The Chemical Wear of the SEN Slagline in the Continuous Casting of Stainless Steels”, *85th Steelmaking Conference*, 2002, pp. 419-428.
36	L. Heaslip, I. Sommerville, A. McLean, L. Swartz, and W. Wilson. “Model Study of Fluid Flow and Pressure Distribution During SEN Injection - Potential for Reactive Metal Additions During Continuous Casting”, *Iron and Steelmaker*, Vol. 14[8] 1987, pp. 49-64.
37	I. Sasaka, T. Harada, H.Shikano and I. Tanaka. “Improvement of Porous Plug and Bubbling Upper Nozzle For Continuous Casting”, *74th ISS Steelmaking Conference*, 1991, pp. 349-356.
38	N. Sidmar, F. Haers, R. Bauwens, R. Croock and M. Moor. “First Experience in Using the Caster Tube Change Device (TCD90)”, *4th International Conference on Continuous Casting*, 1988, pp. 503-514.
39	N. Tsukamoto, K. Ichikawa, E. Iida, A. Morita and J. Inoue “Improvement of Submerged Nozzle Design Based on Water Model Examination of Tundish Slide Gate”, *74th ISS Steelmaking Conference*, 1991, pp. 803-808.
40	L. Zhang, B.G. Thomas and B. Rietow. "Investigation of Ingot Inclusions Using Microscope and SEM", University of Illinois at Urbana-Champaign: Illinoi, Report No. CCC200406, 2004.
41	H. Yin and H. Tsai. "Application of Cathodoluminescence Microscopy (CLM) in Steel Research", in *Iron & Steel Society International Technology Conference and Exposition*, 2003, pp. 217-226.
42	R. Gass, H. Knoepke, J. Moscoe, R. Shah, J. Beck, J. Dzierzawski and P. Ponikvar. "Conversion of Ispat Inland's No.1 Slab Caster to Vertical Bending", *ISSTech2003 Conference Proceedings*, pp. 3-18.
43	P. Rocabois, J.-N. Pontoire, V. Delville and I. Marolleau. "Different Slivers Type Observed in Solla Steel Plants and Improved Practice to Reduce Surface Defects on Cold Roll Sheet", *ISSTech2003 Conference Proceedings*, pp. 995-1006.

44	*Submerged Pouring Tubes*, Vesuvius corp., 2011. [online], Available: http://www.vesuvius.com/en/end-markets/iron-steel/casting/continuous-casting/tundish-flow-control-refractories /submerged-pouring-tubes/ [Accessed: 20 Jan. 2012]
45	W. Lai, M. Milone and I. Samarasekera. "Meniscus Thermal Analysis as a Tool for Evaluating Slab Surface Quality", *83rd Steelmaking Conference Proceedings*, 2000, pp. 461-476.
46	D. Gupta, S. Subramaniam and A. Lahiri. "Study of Fluid Flow and Residence-Time Distribution in a Continuous Slab Casting Mould", *Steel Research,* Vol. 62 [11], 1991, pp. 496- 500.
47	D. Gupta, S. Chakraborty and A. Lahiri." Asymmetry and Oscillation of the Fluid Flow Pattern in a Continuous Casting Mould: a Water Model Study", *ISIJ International,* Vol. 37 [7], 1997, pp. 654-58.
48	D. Gupta and A.K. Lahiri. "A Water Model Study of the Flow Asymmetry Inside a Continuous Slab Casting Mold", *Metallurgical and Materials Transactions B,* Vol. 27B [5], 1996, pp. 757-764.
49	L.J. Heaslip and J. Schade. "Physical Modeling and Visualization of Liquid Steel Flow Behavior during Continuous Casting", *Iron Steelmaker,* 1999, Vol. 26 [1], pp. 33-41.
50	N. Tsukamoto, K. Ichikawa, E. Iida, A. Morita and J. Inoue. "Improvement of Submerged Nozzle Design Based on Water Model Examination of Tundish Slide Gate", *74th ISS Steelmaking Conference*, 1991, pp. 803-808.
51	T. Chung. *Computational Fluid Dynamics*. Cambridge: Cambridge University Press, 2002.
52	F. Menter. "Two-equation eddy-viscosity turbulence models for engineering applications", *AIAA-Journal*, Vol. 32[8], 1994, pp. 269-289.
53	D. Wilcox. *Turbulence Modeling for CFD*., CA: DCW Industries Inc., 1993.
54	B.G. Thomas and L. Zhang. "Mathematical Modeling of Fluid Flow in Continuous Casting", *ISIJ International*, Vol. 41[10], 2001, pp.1181-1193.
55	B. Thomas, Q. Yuan, S. Sivaramakrishnan, T. Shi, S. Vanka, and M. Assar. "Comparison of Four Methods to Evaluate Fluid Velocities in a Continuous Slab Casting Mold", *Iron Steel Institute Japan (ISIJ) International*, Vol. 41[10], 2001, pp. 1262-1271.

56	H. Bai and B.G. Thomas. "Turbulent Flow of Liquid Steel and Argon Bubbles in Slide-Gate Tundish Nozzles, Part I, Model Development and Validation," *Metallurgical Materials Transaction B,* Vol. 32B [2], 2001, pp. 253-267.
57	H. Bai, and B. Thomas. "Two Phase Flow in Tundish Nozzles During Continuous Casting of Steel", *Materials Processing in the Computer Age III, TMS Annual Meeting*, Nashville, TN, 2000, pp. 85-99.
58	B.G. Thomas, X. Huang, and R.C. Sussman. "Simulation of Argon Gas Flow Effects in a Continuous Slab Caster", *Metallurgical & Materials Transaction B,* Vol. 25B [4], 1994, pp. 527-547.
59	B.G. Thomas, A. Denissov, and H. Bai. "Behavior of Argon Bubbles during Continuous Casting of Steel", *80th ISS Steelmaking Conference Proceedings*, 1997, pp. 375-384.
60	C. Pfeiler, M. Wu and A. Ludwig. "Influence of Argon Gas Bubbles and Non-Metallic Inclusions on the Flow Behavior in Steel Continuous Casting", *Materials Science & Engineering,* Vol.413, 2005, pp. 115-120.
61	H. Yu, M. Zhu and J. Wang. "Interfacial Fluctuation Behavior of Steel/Slag in Medium-Thin Slab Continuous Casting Mold With Argon Gas Injection", *International Journal of Iron and Steel Research*, Vol. 17[4], 2010, pp. 5-11.
62	M. Iguchi, J. Yoshida, T. Shimzu and Y. Mizuno. "Model study on the entrapment of mold powder into molten steel", *ISIJ International*, Vol. 40, 2000, pp. 685-691.
63	L.J. Heaslip and J. Schade. "Physical Modeling and Visualization of Liquid Steel Flow Behavior During Continuous Casting", *Iron & Steelmaker,* Vol. 26, 1999, pp. 33-41.
64	R. Miranda, M. Barron, J. Barreto, L. Hoyos and J. Gonzalez. "Experimental and numerical analysis of the free surface in a water model of a slab continuous casting mold", *The Iron and Steel Institute of Japan International*, Vol. 45 [11], 2005, pp. 1626-1635.
65	J. Szekely and R. Yadoya. "The physical and mathematical modelling of the flow field in the mold region in continuous casting systems", *Metallurgical & Materials Transactions*, Vol. 4[5], 1973, pp.1379-1388.
66	F.M. Najjar, B. Thomas and D. Hershey. "Numerical Study of Steady Turbulent Flow through Bifurcated Nozzles in Continuous Casting", *Metallurgical Transactions B*, Vol. 26B [4], 1995, pp. 749-765.

67	F.M. Najjar, D. Hershey, and B. Thomas. "Turbulent Flow through Bifurcated Nozzles", *International Journal for Numerical Methods in Fluids*, Vol. 17 [1], 1993, pp. 23-47.
68	B. Thomas and S. Vanka. "Study of Transient Flow Structures in the Continuous Casting of Steel", in *Proc. NSF Design & Manufacturing Grantees Conference*, 2000.
69	S. Patankar. *Numerical Heat Transfer and Fluid Flow*. Washington: Hemisphere Publishing Corp, 1980.
70	B.E. Launder and D. Spalding. "Numerical computation of turbulent flows", *Computer Methods in Applied Mechanics and Engineering*, Vol. 13, 1974, pp. 269-289.
71	GAMBIT Version 2.0, Fluent Inc., Lebanon, NH, USA, www.fluent.com, 2002-4.
72	ANSYS-FLUENT Version 12.0, ANSYS Inc., www.ansys.com, April 2009.
73	R. Kumar and N. Kuloor. "The formation of bubbles and drops", *Advances in Chemical Engineering*, Vol. 8, 1970, pp. 255–368.
74	A. Kulkarni and J. Joshi. "Bubble formation and bubble rise velocity in gas–liquid systems: a review.", *Industrial and Engineering Chemistry Research*, Vol. 44, 2005, pp. 5873–5931
75	L.J. Heaslip and J. Schade. "Physical Modeling and Visualization of Liquid Steel Flow Behavior During Continuous Casting," *Iron & Steelmaker,* Vol. 26 [1], 1999, pp. 33-41.
76	S. Morsi, and A. Alexander. "An investigation of particle trajectories in two-phase flow systems", *Journal of Fluid Mechanics*, Vol. 55,1972, pp. 193–208
77	M. Sevik and S.H. Park."The splitting of drops and bubbles by turbulent fluid flow," *Journal of Fluids Engineering Transactions AIME*, 1973, pp. 53-60.
78	L. Zhang and S. Taniguchi. "Fundamentals of Inclusions Removal from Liquid Steel by Bubbles Flotation", *International Materials Reviews*, Vol. 45 [2], 2000, pp.59-82.
79	Vesuvius Crucible Company. "Gas permeable stopper rod", US Patent 4791978, Nov 1987.
80	R. Tan, W. Chen, and K. Tan. "A non-spherical model for bubble formation with liquid cross-flow", *Chemical Engineering Science*, Vol. 55 [24], 2000, pp. 6259- 6267.
81	G. Irons and R. Guthrie. "Bubble Formation at Nozzles in Pig Iron", *Metallurgical & Materials Transactions B*, Vol. 9[2], 1978, pp. 101-110.
82	M. Iguchi, T. Chihara,N. Takanashi, Y. Ogawa, N. Tokumitsu, and Z.Morita. "X-ray fluoroscopic observation of bubble characteristics in a molten iron bath", *ISIJ*

	International, Vol. 35 [11], 1995, pp.1354–1361.
83	H. Bai and B.G. Thomas. "Bubble Formation During Horizontal Gas Injection into Downward Flowing Liquid", *Metallurgical and Materials Transactions B*, Vol. 32B [6], 2001, pp. 1143-1159.
84	R. Clift, J. Grace, and M. Weber. *Bubbles, Drops, and Particles*. New York: Academic Press, 1978.
85	A. Ramos-Banderas, R. Morales, R. Sánchez-Pérez, L. García-Demedices, G. Solorio-Díaz. “Dynamics of two phases downwards flows in submerged entry nozzles and its influence on the two-phase flow in the mold”, *International Journal of Multhiphase Flow,* Vol. 31[5], 2005, pp.643-665.
86	S.A. Argyropoulos. "Measurement of Velocity in High Temperature Metals and Slags", 39th *Fundamentals of Metallurgical Processing: The James M. Toguri Symposium,* Canada, 2000, pp. 31-42.
87	B. Rietow and B.G. Thomas. “Using Nail Board Experiments to Quantify Surface Velocity in the CC Mold“, *AISTech 2008 Steelmaking Conference Proceedings*, 2008, pp. 75-86.
88	B. Thomas, J. Yurko and L. Zhang. "Measurement of Molten Steel Surface Velocity with SVC and Nail Dipping during Continuous Casting Process", *Sensors, Sampling, and Simulation for Process Control*. Hoboken, NJ: Wiley-TMS, 2011, pp. 67–75.
89	J. Sengupta, B. Thomas, H. Shin, G. Lee and S. Kim. "Mechanism of hook formation during continuous casting of ultra-low carbon steel slabs", *Metallurgical & Materials Transactions A*, Vol. 37A [5], 2006, pp.1597–1611.
90	S. Seyedein and Hasan. “A three-dimensional simulation of coupled turbulent flow and macroscopic solidification heat transfer for continuous slab casters”, *International Journal of Heat and Mass Transfer*, Vol. 40 [18], 1997, pp. 4405-4423.
91	B. Thomas, R. O’Malley, T. Shi, Y. Meng, D. Creech, and D. Stone. “Validation of Fluid Flow and Solidification Simulation of a Continuous Thin-Slab Caster”, *Modeling of Casting, Welding, and Advanced Solidification Processes IX*, 2000, pp. 769-776.

Appendix A

Derivation of Discrete Phase Model governing equation:

$$m_p \frac{du_p}{dt} = F_D + F_B + F_a$$

where, The drag force term (F_D) = $\frac{1}{2}\rho v^2 C_D A$ (from Newton's second law of motion.)

$$m_p \frac{du_p}{dt} = \frac{1}{2}\rho\left(\left|u - u_p\right|\right)^2 C_D A + V_p g(\rho_p - \rho) + m_p f_a$$

$$m_p \frac{du_p}{dt} = \frac{1}{2}\rho|u_{rel}||u_{rel}|C_D \frac{\pi d_p^2}{4} + m_p \frac{g(\rho_p - \rho)}{\rho_p} + m_p f_a$$

$$m_p \frac{du_p}{dt} = \frac{1}{8}\rho|u_{rel}||u_{rel}|C_D \pi d_p d_p + m_p \frac{g(\rho_p - \rho)}{\rho_p} + m_p f_a$$

$$m_p \frac{du_p}{dt} = \frac{1}{8}\left(\frac{\boldsymbol{\rho|u_{rel}|d_p}}{\mu}\right).|u_{rel}|\ C_D \pi d_p \mu + m_p \frac{g(\rho_p - \rho)}{\rho_p} + m_p f_a$$

$$m_p \frac{du_p}{dt} = \frac{1}{8} Re|u_{rel}|\ C_D \pi d_p \mu \frac{\frac{d_p^2}{6}}{\frac{d_p^2}{6}} + m_p \frac{g(\rho_p - \rho)}{\rho_p} + m_p f_a \qquad \text{[Replacing } \frac{\rho|u_{rel}|d_p}{\mu} \text{ by } Re\text{]}$$

$$m_p \frac{du_p}{dt} = \frac{6}{8 d_p^2} Re|u_{rel}|\ C_D \mu \frac{\pi d_p^3}{6}\frac{\rho_p}{\rho_p} + m_p \frac{g(\rho_p - \rho)}{\rho_p} + m_p f_a$$

$$m_p \frac{du_p}{dt} = \frac{6}{8 d_p^2\, \rho_p} Re|u_{rel}|\ C_D \mu \frac{\pi d_p^3 \rho_p}{6}\frac{3}{3} + m_p \frac{g(\rho_p - \rho)}{\rho_p} + m_p f_a$$

$$m_p \frac{du_p}{dt} = \frac{18\mu C_D}{24 d_p^2\, \rho_p} Re|u_{rel}|\ m_p + m_p \frac{g(\rho_p - \rho)}{\rho_p} + m_p f_a \qquad \left[Replacing, \frac{\pi d_p^3 \rho_p}{6} = m_p\right]$$

$$\frac{du_p}{dt} = \frac{18\ \mu C_D Re}{24\ \rho_p d_p^2} u_{rel} + \frac{g(\rho_p - \rho)}{\rho_p} + f_a \qquad [Dividing\ both\ sides\ by\ m_p]$$

Integrating of above equation gives the particle velocities at every cell in the domain.